

**Politecnico di Torino**

Department of Mechanical and Aerospace Engineering

Master Degree in Aerospace Engineering



Master Degree Thesis

**Implementation of a comprehensive  
real-time simulation model  
of a tilt-rotor aircraft**

**Supervisors**

Giorgio Guglieri

Pierluigi Capone

Federico Barra

**Candidate**

Anna Abà

2020



# Summary

The purpose of this work is the description of the implementation of a real-time flight simulation model of the Bell Aircraft Corporation XV-15 Tilt-Rotor Research Aircraft. The model is developed in the Matlab/Simulink environment and integrated with the ReDSim of the ZAV Centre for Aviation at ZHAW, Zurich University of Applied Sciences, in Winterthur, Switzerland, a research and development flight simulator employed for both educational and industrial applications. All the activities described were carried out by the author as part of her Exchange Project at ZHAW, from October 2019 to February 2020. The first part of the author's work has been focused mainly on reviewing and debugging the XV-15 rotor model, in terms of both its mathematical formulation and its implementation in the Simulink environment. Several additions have then been made to the rotor model, with the aim of improving its accuracy while at the same time complying with the requirements for a real-time simulation. Most notably, the formulation of the flapping dynamics has been modified specifically to describe the behaviour of a gimballed rotor. As a result of the debugging and optimization activities carried out by the author, it has been possible to trim the flight simulation model using an algorithm based on the Newton-Raphson method. An extensive phase of model validation has followed. The simulation results have been compared to the data presented in the NASA Report CR-166537, *Development and validation of a simulation for a generic tilt-rotor aircraft*, by Samuel W. Ferguson, 1989. Moreover, a series of pilot-in-the-loop tests has been conducted to assess the performance and handling qualities of the simulated aircraft.



# Contents

<b>Summary</b>	<b>i</b>
<b>List of Figures</b>	<b>v</b>
<b>List of Tables</b>	<b>vii</b>
<b>1 Introduction</b>	<b>1</b>
1.1 The search for new effective V/STOL aircraft . . . . .	1
1.2 The first technology demonstrators . . . . .	5
1.3 Current industrial developments . . . . .	9
1.3.1 V-22 Osprey . . . . .	9
1.3.2 AW-609 . . . . .	10
1.3.3 V-280 Valor . . . . .	11
1.3.4 Electric convertiplanes . . . . .	12
1.3.5 UAVs . . . . .	12
<b>2 The XV-15 Tilt-Rotor Research Aircraft</b>	<b>15</b>
2.1 General characteristics . . . . .	15
2.2 The rotor assembly . . . . .	17
2.3 The role of flight simulation . . . . .	18
2.4 The ReDSim flight simulator at ZAV . . . . .	20
2.4.1 The XV-15 simulation model . . . . .	21
<b>3 Review and development of the rotor mathematical model</b>	<b>23</b>
3.1 General description . . . . .	23
3.1.1 Reference frames . . . . .	23
3.1.2 Rotor aerodynamics . . . . .	25
3.1.3 Flapping dynamics . . . . .	28
3.1.4 Multi-blade coordinates . . . . .	30
3.1.5 Hub loads . . . . .	30
3.1.6 Inflow dynamics . . . . .	32
3.2 Gimbal model . . . . .	33
3.3 Trim algorithm . . . . .	35
<b>4 Implementation of the Simulink model</b>	<b>39</b>
4.1 Overview . . . . .	39
4.2 Rotor model architecture . . . . .	41
4.3 Blade aerodynamics . . . . .	42
4.3.1 Airfoil aerodynamic coefficients . . . . .	43
4.4 Integration of differential equations . . . . .	47

4.4.1	Flapping dynamics . . . . .	47
4.4.2	Inflow dynamics . . . . .	48
4.5	Trimming the model . . . . .	49
<b>5</b>	<b>Validation and results</b>	<b>51</b>
5.1	Comparison of trim results . . . . .	51
5.2	Pilot-in-the-loop tests . . . . .	59
5.2.1	Helicopter mode . . . . .	59
5.2.2	Airplane mode . . . . .	81
<b>6</b>	<b>Conclusions</b>	<b>85</b>
<b>A</b>	<b>Rotor mathematical model equations</b>	<b>87</b>
A.1	Blade position, speed and acceleration . . . . .	87
A.1.1	Position . . . . .	87
A.1.2	Speed . . . . .	88
A.1.3	Acceleration . . . . .	89
A.2	Blade aerodynamics . . . . .	91
A.2.1	Angle of attack . . . . .	91
A.2.2	Aerodynamic forces and moments . . . . .	92
A.3	Gimballed rotor flapping dynamics . . . . .	94
A.4	Hub loads . . . . .	94
<b>B</b>	<b>Trim results</b>	<b>97</b>
B.1	Helicopter mode . . . . .	97
B.2	Conversion . . . . .	101
B.3	Airplane mode . . . . .	113
<b>C</b>	<b>Examples of Flight Test Cards</b>	<b>129</b>
C.1	The Cooper-Harper Handling Qualities Rating Scale . . . . .	129
C.2	Helicopter mode . . . . .	130
C.2.1	Hover . . . . .	130
C.2.2	Pirouette . . . . .	132
C.2.3	Sidestep . . . . .	134
C.3	Airplane mode . . . . .	136
	<b>Bibliography</b>	<b>137</b>

# List of Figures

1.1	Examples of V/STOL aircraft . . . . .	2
1.2	Collage showing the V-22 Osprey ( <i>left to right</i> ) in helicopter mode, during in-flight conversion and in airplane mode (Reference [12]) . . . . .	3
1.3	The Transcendental Model 1-G (Reference [12]) . . . . .	5
1.4	Photograph of the Bell XV-3 in helicopter mode . . . . .	6
1.5	The Vertol Model 76 tilt-wing aircraft (Reference [12]) . . . . .	7
1.6	The XC-142 during a test flight on a U.S. Navy ship (Reference [12]) . . . . .	8
1.7	The XV-15 in helicopter mode during a test flight at the NASA Dryden Flight Research Center in 1980 (Courtesy of NASA) . . . . .	9
1.8	Two V-22 Ospreys taking off from a U.S. Navy carrier ship . . . . .	10
1.9	The AW-609 in forward flight (Courtesy of Agusta Westland) . . . . .	11
1.10	The V-280 Valor during its first autonomous flight . . . . .	11
1.11	The Airbus A <sup>3</sup> Vahana during its first flight at one of the A <sup>3</sup> Facilities in the Silicon Valley (Courtesy of Airbus) . . . . .	12
1.12	Rendering of the electric tilt-wing aircraft being currently developed by Dufour Aerospace (Courtesy of Dufour Aerospace) . . . . .	13
1.13	The Bell Eagle Eye tilt-rotor UAV . . . . .	13
2.1	The XV-15 Tilt Rotor Research Aircraft flying in airplane mode (Reference [12]) . . . . .	16
2.2	General layout and major components of the XV-15 (Reference [15]) . . . . .	16
2.3	A single XV-15 proprotor in the 40- by 80-foot wind tunnel at NASA Ames Research Center (Reference [12]) . . . . .	18
2.4	The XV-15 hub and blade-retention assembly (Reference [12]) . . . . .	19
2.5	Scheme of the working principle of the hub universal joint (Reference [12]) . . . . .	19
2.6	View of the ReDSim flight simulator (Courtesy of ZAV) . . . . .	20
2.7	Scheme of the major ReDSim equipment (Courtesy of ZAV) . . . . .	21
2.8	Schematic representation of the ReDSim hardware architecture (Reference [2]) . . . . .	22
3.1	Reference frames for the right rotor . . . . .	24
3.2	Sketch of a generic blade section . . . . .	26
3.3	Sketch of the forces involved in the blade flapping dynamics . . . . .	29
3.4	Forces and moments acting on each blade . . . . .	31
4.1	Block diagram representing the architecture of the complete XV-15 aircraft model . . . . .	40
4.2	Architecture of the rotor Simulink model . . . . .	41
4.3	Complete $C_l - \alpha$ and $C_{l\alpha} - \alpha$ curves for the NACA 64-208 airfoil . . . . .	44
4.4	Complete $C_d - \alpha$ and $C_{d\alpha} - \alpha$ curves for the NACA 64-208 airfoil . . . . .	45

4.5	Rotor hover performance – Variation of the thrust coefficient with the collective pitch . . . . .	45
4.6	Rotor hover performance – Torque coefficient versus thrust coefficient . . . .	46
4.7	Rotor hover performance – Thrust-to-solidity ratio versus Figure of Merit ( $FM = \sqrt{C_T^3/2/C_P}$ ) . . . . .	46
4.8	Implementation of the Forward Euler Method in the Simulink model . . . . .	48
4.9	Flow chart of the process adopted to trim the model . . . . .	49
5.1	Example of the trim results contained in Reference [8] . . . . .	52
5.2	Comparison of trim results – Angle of attack . . . . .	54
5.3	Comparison of trim results – Root collective pitch . . . . .	54
5.4	Comparison of trim results – Longitudinal cyclic . . . . .	55
5.5	Comparison of trim results – Rotor coning angle (Helicopter mode) . . . . .	55
5.6	Comparison of trim results – Tip-path-plane orientation . . . . .	56
5.7	Comparison of trim results – Overall rotor forces and moments, Helicopter mode . . . . .	57
5.8	Comparison of trim results – Overall rotor forces and moments, Airplane mode, 517 rpm, 12 000 ft . . . . .	58
5.9	Test course for the Hover task . . . . .	61
5.10	Simulation data records for Hover task, SCAS off – Aircraft angular rates . .	62
5.11	Simulation data records for Hover task, SCAS off – Pilot controls . . . . .	63
5.12	Simulation data records for Hover task, SCAS off – Comparison between lateral cyclic input and aircraft roll rate . . . . .	64
5.13	Simulation data records for Hover task, SCAS on – Aircraft angular rates . .	65
5.14	Simulation data records for Hover task, SCAS on – Pilot controls . . . . .	66
5.15	Simulation data records for Hover task, SCAS on – Trajectory . . . . .	67
5.16	Test course for the Pirouette task, as implemented in the ReDSim simulator .	69
5.17	Simulation data records for Pirouette task, SCAS off – Trajectory (the yellow boundaries indicate the requirements for adequate performance) . . . . .	70
5.18	Simulation data records for Pirouette task, SCAS off – Lateral speed, roll angle and pitch angle . . . . .	71
5.19	Simulation data records for Pirouette task, SCAS off – Pilot controls . . . .	72
5.20	Test course for the Sidestep task . . . . .	73
5.21	Simulation data records for Sidestep task, SCAS on, Pilot 1 – Lateral speed and trajectory . . . . .	75
5.22	Simulation data records for Sidestep task, SCAS on, Pilot 1 – Euler angles .	76
5.23	Simulation data records for Sidestep task, SCAS on, Pilot 1 – Pilot controls	77
5.24	Simulation data records for Sidestep task, SCAS on, Pilot 2 – Euler angles .	78
5.25	Simulation data records for Sidestep task, SCAS on, Pilot 2 – Lateral speed and trajectory . . . . .	79
5.26	Simulation data records for Sidestep task, SCAS on, Pilot 2 – Trajectory (the yellow boundaries indicate the requirements for adequate performance)	79
5.27	Simulation data records for Sidestep task, SCAS on, Pilot 2 – Pilot controls	80
5.28	Simulation data records for airplane mode, SCAS off – Pilot controls . . . .	82
5.29	Simulation data records for airplane mode, SCAS off – Ground speed, altitude and angular rates . . . . .	83
A.1	Integration using the method of the trapezoids . . . . .	93

C.1 The Cooper-Harper Handling Qualities Rating Scale (Reference [1]) . . . . . 129

## List of Tables

5.1 Flight conditions considered for the comparison of trim results . . . . . 53  
5.2 Performance standards for the Hover task (Reference [1]) . . . . . 61  
5.3 Performance standards for the Pirouette task (Reference [1]) . . . . . 69  
5.4 Performance standards for the Sidestep task (Reference [1]) . . . . . 74



# Chapter 1

## Introduction

### 1.1 The search for new effective V/STOL aircraft

Following the first successful demonstrations of the airplane at the beginning of the XX century and the helicopter in the 1930s, the world's aviation panorama has evolved along two fundamental directions:

- The progress in airplane design, manufacturing and operations has allowed these machines to reach increasingly high cruise speed, range, cruise altitude and payload capacity. However, the fixed-wing concept comes with serious issues of stability, control and performance at low speed, and the aforementioned improvements have not been achieved without paying a price: in fact, they have been accompanied by a progressive rise in aircraft minimum speed, which translates into longer take-off and landing distances, hence the necessity of longer runways and bigger airfields. Today, especially in very densely populated areas, airports are usually located quite distant from city centres, thus reducing the time gain afforded by air transport compared to other means such as rail and road; moreover, with the ever-growing demand for the transfer of people and goods all around the planet, delays and air traffic congestion have become increasingly serious and urgent problems.
- Thanks to their unique low speed performance, and the ability to take off and land vertically, helicopters have established themselves as a particularly suitable solution for a vast variety of both civil and military missions, such as: search and rescue, survey of wide areas, support to troops and police forces, point-to-point transport in isolated sites or harsh environments, aerial work, and many more. All these applications require high versatility and enhanced, low speed capabilities which are peculiar to rotorcraft and very hard to be found in any conventional airplane. On the other hand, helicopters suffer from strong limitations on the maximum speed, range, altitude and payload capacity achievable – disadvantages which, combined with the high operative costs, fuel consumption, noise and vibration levels typical of these machines, impact negatively on their productivity and put a severe constraint on their deployment in other civil and military mission scenarios.

Given the situation, it is hardly surprising that, over the past eight decades, the aviation industry has repeatedly tried to come up with a new aircraft concept able to get over the shortcomings of both airplanes and rotorcraft, combining the high speed, range, payload, altitude performances of fixed-wing aircraft with the low speed and V/STOL<sup>1</sup> capabilities of helicopters.

---

<sup>1</sup>Vertical / Short Take-Off and Landing



(a) The McDonnell XV-1



(b) The McDonnell/British Aerospace Harrier



(c) The Bell Aerospace X-22A

(d) The Eurocopter X<sup>3</sup>**Figure 1.1:** Examples of V/STOL aircraft

Starting from the 1940s, several new technologies and configurations have been explored, with the aim of either extending the flight envelope of fixed-wing aircraft in the low-speed regime, or pushing the speed, altitude and range limits of rotorcraft towards more airplane-like values; some examples can be seen in Figure 1.1. Although a discreet number of prototypes was built and numerous ground and flight test campaigns were performed, only very few<sup>2</sup> of these new aircraft have actually reached production and are currently deployed as military aircraft; to date, no civil aviation V/STOL has yet entered into service.

Among the assortment of V/STOL concepts proposed, convertiplanes represent one of the most interesting and promising solutions. These innovative machines reunite in a single aircraft the characteristics of both an airplane and a helicopter, combining a lifting wing with two (or more) proprotors which can produce lift or thrust:

- In helicopter mode, the proprotors operate like conventional edgewise-flying helicopter rotors, generating lift and endowing the aircraft with helicopter-like hovering, VTOL and low speed capabilities.
- In airplane mode (i.e. at higher speeds) the proprotors, tilted 90 degrees forward, act like large-diameter propellers and produce thrust – all required lift being now

<sup>2</sup>Franklin D. Harris, in Reference [12], cites only three successful V/STOL concepts:

- The Bell / Boeing V-22 Osprey tilt-rotor (Figure 1.2 and 1.8).
- The McDonnell / British Aerospace Harrier (Figure 1.1b), a VTOL fighter powered with a single jet engine; hovering is obtained by means of swivelling nozzles which direct engine thrust towards the ground.
- The Boeing C-17A, a STOL military transport airplane in which exhaust from the four jet engines is exploited to increase lift from the wing flaps, thus reducing dramatically take-off and landing distances.



**Figure 1.2:** Collage showing the V-22 Osprey (*left to right*) in helicopter mode, during in-flight conversion and in airplane mode (Reference [12])

provided by the wing. The aircraft can therefore operate like, and achieve cruise speed, range and efficiency similar to, a conventional propeller-driven airplane.

Conversion between the two modes is accomplished in flight, either by rotating the whole wing-engine-propotor assembly as a unit (as happens in tilt-wing aircraft), or by tilting only the wing-tip-mounted engines and propotors (the wing being hard-mounted to the fuselage, as is the case with tilt-rotors). Since the same power plant system is used both for take-off and landing and for forward flight, airplane-like cruise performance can be obtained without an excessive increase in the required installed power, thus affording better fuel-effectiveness and payload capacity, at equal design gross weight, than other V/STOLs such as, for instance, compound helicopters.

The search for an operationally successful convertiplane began in the early 1950s and continued through the following decades, with a series of technology demonstrators being developed and tested in order to prove the feasibility of both tilt-wing and tilt-rotor concepts. The results of this massive effort, together with major advancements in aviation in general, led to the birth of the first – and, so far, only – fully operational tilt-rotor, the V-22 Osprey, which entered service in 1999 with the U.S. Marine Corps. Today, the aviation industry interest in convertiplanes is far from being dead and many companies, from major manufacturers to small start-ups, are investing in the development of new tilt-rotor and tilt-wing solutions for civil as well as military applications.

There are several ways in which civil aviation could benefit from the introduction of commercial convertiplanes:<sup>3</sup>

- In densely populated regions, convertiplanes could substitute traditional commuter airplanes in meeting part of the demand for short-haul passenger transport. Thanks to their VTOL capability, these aircraft could bring multiple advantages: passengers

<sup>3</sup>Reference [20]

mobility would be improved, by making them able to begin and end their flight closer to their starting point and destination, and thus minimizing the time and expense related to the ground segments of the trip; moreover, significant congestion relief would be provided both to airports and the whole system of infrastructures connected to them, reducing delays, freeing runway slots for larger aircraft, increasing the time- and cost-effectiveness of air transport in general.

- Tilt-rotor and tilt-wing potential for high mission flexibility, speed and productivity, as well as the ability to operate close to metropolitan business destinations, constitute undoubtedly attractive features for corporations and other organisations aiming at making the most effective and profitable use of their business aircraft. Therefore, convertiplanes could capture a large portion of the corporate/executive transport market, successfully replacing both airplanes and helicopters.
- Convertiplanes could also be employed to provide air service to low density or developing regions, as well as remote and isolated areas, affording increased and better-quality mobility to small communities.
- One of the biggest and most successful markets for large helicopters is represented by support to natural resource development activities, and in particular supply of offshore oil and gas platforms. The introduction of convertiplanes into this context could bring substantial economic benefits, due to higher cruise speed, range and payload capability.
- Finally, convertiplanes would be ideal substitutes for helicopters in a wide variety of public service missions: their higher range, speed and endurance would provide significant improvements in search and rescue operations and police applications such as air patrol, drug enforcement, high-priority personnel transport; moreover, their greater payload capacity would be a critical advantage in emergency medical transport and disaster relief missions, where the ability to move rapidly large numbers of people is required.

Unfortunately, the tilt-wing and tilt-rotor concepts are still very far from maturity, and the various technology demonstrators, as well as the V-22 itself, have explored but a small fraction of their unique potential. For one thing, there is still room for improvement in terms of both hovering and high speed capability, and better performances will be crucial in making convertiplanes actually competitive with helicopters and airplanes. In addition, the coexistence of both airplane and helicopter features is a source of extreme complexity: numerous technical problems have emerged and some, especially the ones related to aircraft aeromechanic stability, are still waiting for a definitive solution. Costs are also very high, the estimated price of a convertiplane being currently 3-400% higher than that of a helicopter – to which several further operating and maintenance costs should be added. Finally, several other issues concerning safety, operations, fuel efficiency, noise levels, environmental impact, passenger comfort, integration with air traffic and existing infrastructures, need to be addressed.

Convertpiplanes have proved a viable and promising answer to the demand for new effective V/STOL aircraft, but lots of work still have to be done before these groundbreaking machines can finally make their entrance into the civil aviation scene.



**Figure 1.3:** The Transcendental Model 1-G (Reference [12])

## 1.2 The first technology demonstrators

Although studies on convertiplanes had already been conducted since before World War II<sup>4</sup>, it was in the 1950s that exploration of tilt-rotor and tilt-wing concepts began in earnest. Experience gathered over the previous decades had allowed airplane and helicopter to reach a good degree of maturity but had also highlighted their limitations, while military scenarios kept setting increasingly challenging requirements in terms of hovering performance, agility and low speed maneuverability, united with high speed and range capabilities – characteristics impossible to be found together in any of the then-current fixed-wing and rotary-wing aircraft. Several approaches were proposed to meet the new requirements, and the U.S. armed forces launched between the 1950s and the 1970s a series of programs aimed at demonstrating and evaluating the different concepts. It is in this context that the first successful convertiplanes made their appearance.

The first step towards the demonstration of the tilt-rotor concept was taken when Mario Guerreri and Robert Lichten, engineers at Transcendental Aircraft Corporation, started development of the Transcendental Model 1-G (Figure 1.3). This small tilt-rotor attracted the attention of the U.S. Air Force, leading to a contract between USAF and Transcendental for a series of ground and flight tests. The first hovering flight was completed in 1954 and subsequent tests culminated with a partial in-flight conversion from a shaft angle of 0 degrees (helicopter mode) to about 70 degrees forward. However, severe problems due mainly to mechanical instability during conversion caused the USAF to eventually withdraw its financial support, marking the end of the project and of Transcendental itself.

In the meantime, the interest of both the U.S. Army and the U.S. Air Force in developing new VTOL aircraft led to the creation of a joint program and the issue, in 1951, of a Request for Proposal for convertible aircraft. In response, Bell Aircraft Corporation presented its Model 200 tilt-rotor, later designated as XV-3, after a considerable research and development activity led by Larry Bell and Robert Lichten (who had by then relocated at Bell). Following extensive ground tests, the initial hover trial of the XV-3 was flown in August 1955; both that and subsequent test flights showed that the machine had satisfactory characteristics during the beginning of the flight, but suffered from high vibrations in hover due to dynamic instability of the proprotor-pylon assembly. Such instability caused a nearly fatal crash in October 1956, prompting Bell engineers to ground the XV-3 and start a series of research activities and tiedown tests in order to solve and better understand this problem. Analysis capabilities were at that time very limited, and dynamicists had to rely mainly

---

<sup>4</sup>See Reference [12], [15]



**Figure 1.4:** Photograph of the Bell XV-3 in helicopter mode

on traditional analyses, combined with experimental data and trial-and-error empirical methods. A partial solution was finally reached by replacing the original three-bladed articulated proprotors with two-bladed, stiff-inplane teetering rotors, and test flights were resumed in 1958.

The final XV-3 prototype (Figure 1.4) had the two-bladed proprotors mounted on a shaft assembly at each wing tip, with the possibility to tilt each rotor over a range of 90 degrees to achieve conversion from between helicopter and airplane mode. Both rotors were powered by a single Pratt and Whitney R-985-AN-1 supercharged piston engine mounted inside the fuselage. The aircraft had conventional empennages with the addition of a central fin below the rudder, and a skid-type landing gear; to increase wing stiffness, fuselage-to-wing tip struts are incorporated into the structure. The cockpit contained helicopter-like controls (cyclic control stick, collective pitch stick with twist grip throttle, and rudder pedals); during conversion a mechanical system automatically reduced longitudinal cyclic controls and increased the collective pitch in order to meet the required operative range. Neither lateral cyclic proprotor controls nor a stability augmentation system were installed.

The first full tilt rotor conversion was achieved in December 1958, and in subsequent flight tests a speed of 155 knots was attained before experiencing aeroelastic instability. By the end of the XV-3 program in 1968, a total of 110 full conversions were accomplished over 125 flight hours. Test evaluation performed both at Bell and military facilities showed that the machine was clearly underpowered, leading to rather poor performances both in hover and at higher speed; in addition, important deficiencies in handling qualities and structural stability were highlighted, resulting in low control response at low speed and instability during in-ground-effect hovering, as well as crashes and fatigue failures. All the same, the XV-3 represented a superb achievement, given the technology and engineering knowledge then available: it proved the fundamental feasibility of the tilt-rotor concept, and in particular its ability to safely perform in-flight conversion between airplane and helicopter mode, thus leading the way to further development of tilt-rotor aircraft.



**Figure 1.5:** The Vertol Model 76 tilt-wing aircraft (Reference [12])

Almost concurrently with the development of the first til-rotors, exploration of another convertiplane concept, the tilt-wing, began. The first successful prototype displaying this configuration was the Vertol Aircraft Corporation Model 76 (Figure 1.5), which completed its first flight in August 1957 and achieved the first full conversion from hover to forward flight and back in July 1958. Albeit presenting serious issues of high vibration, poor stability and control, and wing stalling during conversion and descent, the new aircraft garnered attention from the U.S. armed forces, and extensive military-funded testing was performed until the early 1960s. At the same time, other tilt-wing prototypes, such as the Hiller X-18 and the Canadair CL-84, were built and tested with varying degrees of success.

In 1961 the U.S. Department of Defense started a "Tri-Service" program, involving the U.S. Army, Navy and Air Force and aimed at the development of new V/STOL aircraft concepts. The competition was won by Vought-Hiller Aircraft Corporation and Ryan Aeronautical Company with the design for a tilt-wing convertiplane which was subsequently designated as the XC-142A. The aircraft (Figure 1.6) was a cargo/assault transport meant to carry 32 troops over 200 nautical miles, and was equipped with four 15-foot-diameter four-bladed propellers powered by four T64-GE-1 turboshaft engines. A first flight as a conventional airplane was made in September 1964, followed two months later by the first hovering flight; the first in-flight conversion and reconversion was performed in January 1965. Thanks to its massive installed power, the XC-142A came with exceptional V/STOL and hovering performances; on the contrary, it failed to meet forward flight requirements due to serious stability and vibration problems. Expected payload capacity was not attained either, and the machine presented also several major issues in terms of noise level, structural fatigue, handling qualities, reliability, maintenance and safety of operations<sup>5</sup>. All these shortcomings discouraged tilt-wing advocates; following a series of severe crashes in 1967, the XC-142 program was interrupted and then officially terminated in 1970, essentially putting an end to all further exploration of the tilt-wing concept by the U.S. military.

While interest in tilt-wing aircraft was apparently lost, the achievements of the XV-3 program had succeeded in convincing the aeronautical world of tilt-rotors unique potential. As a result, several research, testing and development activities were carried out between

<sup>5</sup>One important safety issue was that, given the high disk loading of the XC-142 propellers, slipstream generated by the hovering aircraft was strong enough to blow people down



**Figure 1.6:** The XC-142 during a test flight on a U.S. Navy ship (Reference [12])

the late 1960s and early 1970s both by Government and industry researchers, addressing the issues brought up by the XV-3 and expanding the knowledge base about these aircraft. The output from these activities, together with advancements in aircraft design and simulation, increased confidence in the tilt-rotor concept, prompting NASA and the U.S Army to start in 1971 a program for the development of a new proof-of-concept tilt-rotor research vehicle; the joint nature of the Army/NASA agreement indicated that the project was meant to meet both civil and military needs. Competing solutions by Boeing Vertol and Bell Helicopter were considered; the Bell Model 301 (soon to be designated the XV-15) won over the Boeing Model 222, and a \$ 40 million contract was awarded to Bell in 1973 for the design, fabrication and testing of two technology demonstrators.

Relying on far more advanced technology than its predecessors, the XV-15 (Figure 1.7) finally demonstrated that helicopter-like low speed features and airplane-like high speed characteristics could, in fact, be incorporated in one single machine. Following the first flight on May 3, 1977, subsequent tests expanded the aircraft flight envelope to altitudes of 25000 feet and cruise speeds of over 300 knots. The aircraft displayed excellent versatility and handling qualities; moreover, a conversion corridor having a wide range of airspeeds, conversion angles and fuselage attitudes, with the flight controls being automatically phased from helicopter to airplane mode, made transition between the two flight modes remarkably easy and safe and significantly reduced pilot workload. As testing proceeded, interest of the U.S. Navy in potential ship board applications led to a series of sea trial evaluations, bringing also important positive outcomes in terms of funding to the project. In September 1981 the U.S. Government declared the primary proof-of-concepts objectives of the XV-15 project to be successfully completed. The aircraft had by then met or exceeded all the goals specified in the original Program Plan, and demonstrated the suitability of tilt-rotor aircraft for civil as well as military applications. Furthermore, the use of state-of-the-art technology for test data acquisition and processing had made it possible to collect massive amounts of information, building up a huge heritage and an invaluable resource for future tilt-rotor research projects.

The legacy of the XV-15 project was picked up by two aircraft: the Bell-Boeing V-



**Figure 1.7:** The XV-15 in helicopter mode during a test flight at the NASA Dryden Flight Research Center in 1980 (Courtesy of NASA)

22 Osprey, which in 1999 became the first fully operational military tilt-rotor, and the Bell-Boeing, now Agusta-Westland AW-609, soon to enter service as the world's first civil tilt-rotor. The XV-15 itself continued its activity as a test aircraft until 2003, and was extensively deployed both by Bell and NASA for research and demonstration of new tilt-rotor technology as well as support to other tilt-rotor design projects.

### 1.3 Current industrial developments

#### 1.3.1 V-22 Osprey

The Bell-Boeing V-22 Osprey has been the first tilt-rotor aircraft to achieve fully operational military status, and currently stands as the only convertiplane actually in service.

Following the success of the XV-15 program, the U.S. Department of Defence launched in 1981 the Joint-service Vertical take-off and landing Experimental aircraft program. This project originated from the need to replace the ageing CH-46 helicopters, used by both the U.S. Army and Marine Corps, with a machine capable of combining VTOL capabilities with increased forward flight performances; another important requirement for the new aircraft was shipboard compatibility, in order to allow operations on U.S. Navy ships.

As an answer to this demand, the V-22 was proposed by a joint-venture between Boeing Vertol and Bell Helicopter Textron. This multi-purpose aircraft has a gross weight of 55000 pounds, is powered by two 6150 horse power gas turbine engines, and is capable of transporting up to 24 troops at a top speed of 363 miles per hour and with a maximum range of more than 800 nautical miles.

The first V-22 built to production entered service in 1999 and eleven units were produced by the end of 2000. Despite registering a few incidents as well as a major crash on December



**Figure 1.8:** Two V-22 Ospreys taking off from a U.S. Navy carrier ship

11, 2000, in 2013 the Bell-Boeing V-22 project was awarded a five-year U.S. Naval Air System Command (NAVAIR) contract for the supply of 99 more units. Today, more than 200 Ospreys have been produced and are currently in service with the U.S. Air Force, Marine Corps and Navy, with a total of more than 185000 flight hours; in 2015 Japan ordered five units for its Self Defence Forces (the first one was delivered in 2017), becoming the first V-22 export customer.

### 1.3.2 AW-609

In addition to the military V-22, Bell and Boeing derived also another concept from the XV-15 experience, i.e. the Model 609, aimed specifically at the commercial transport market. The project has had a rather complicated story, with Bell partnering up with the Italian Agusta after Boeing quit in 1998, and Agusta (which had by then merged with the British Westland) eventually taking over the whole program in 2011.

The two-crew, nine passenger AW-609 has a 16800 pound VTOL design weight and is powered by two Pratt & Whitney PT6C-67A turboprop engines; it made its first flight in 2003 and, so far, has demonstrated 333-knots maximum speed and 275-knots maximum cruise speed, with a range of 700 to 1000 nautical miles and a cruise altitude of 25000 feet. It is meant to be a versatile platform combining the best features of both helicopters and turboprop aircraft, therefore providing VTOL capabilities together with twice the speed and range as a conventional helicopter, as well as a pressurized cabin and advanced avionics technology. Thanks to its high potential, the AW-609 is advertised as a multi-role platform allowing a wide range of missions such as offshore passenger transport, search and rescue, homeland security, emergency medical transfer and VIP transport.

This multi-purpose tilt-rotor is a highly innovative machine, exploiting several state-of-the-art technologies such as a mostly composite airframe and a triple-redundant, fully fly-by-wire flight control system. It is also the first pressurized rotorcraft seeking for certification – a characteristic which comes with several complex implications, as no new helicopter category has been certified since 1946. For this reason among several others, the



**Figure 1.9:** The AW-609 in forward flight (Courtesy of Agusta Westland)



**Figure 1.10:** The V-280 Valor during its first autonomous flight

AW-609 is not yet fully operational (although first delivery is expected for 2020), and in spite of so much effort being put into the project in terms of engineering development and financial commitment, several improvements seem to be still required before certification can be obtained. A tragic setback in the development of the AW-609 occurred in 2015 when, during a test flight, severe aeromechanical instability caused a prototype to break up in mid-air resulting in the death of the two test pilots.

### 1.3.3 V-280 Valor

V-280 is a new tilt-rotor concept, currently under development by a partnership of Bell Helicopter Textron with Lockheed Martin, in the context of the U.S. Army Future Vertical Lift (FVL) program. The latter is aimed at replacing the Sikorsky UH-60 Black Hawk and the Boeing AH-64 Apache helicopters, now in service with the U.S. armed forces.

The V-280 Valor was selected for the Joint Multi-Role Technology Demonstrator phase of the FLV program in 2013 and started flight tests in 2017. The aircraft will have a crew



**Figure 1.11:** The Airbus A<sup>3</sup> Vahana during its first flight at one of the A<sup>3</sup> Facilities in the Silicon Valley (Courtesy of Airbus)

of four and will be capable of transporting 14 troops at a cruise speed of 280 knots (top speed will be 300 knots), over a range of 2100 nautical miles.

### 1.3.4 Electric convertiplanes

Faster transfer of people, goods and information, reduction of traffic congestion and environment pollution, creation of on-demand, customised transport services, are some of the major challenges that modern society poses to today's transportation systems. Convertiplanes, with their unique operational flexibility, have the potential to be absolute protagonists in this scenario – even more so if clean, all-electric propulsion is adopted. For this reason, an increasing number of companies in the aerospace industry, spanning from big corporations to small start-ups, is devoting time and resources to the development of new, fully electric tilt-wing and tilt-rotor concepts – especially small vehicles for short-haul passenger transport.

Among the major players, Airbus is investing in several electric convertiplane projects. The most notable is the A<sup>3</sup> Vahana, an all-electric, self-piloted tilt-wing whose goal is incrementing the company knowledge base with respect to convertible, fully autonomous aircraft, as well as proving the capability of these vehicles to be a cost-comparable replacement for traditional short-range urban transport. Design of the Vahana started in 2016, while flight tests began in 2018 and the first successful conversion was achieved in May 2019.

Another interesting electric tilt-wing concept is being developed by the Swiss company Dufour Aerospace, and aims to revolutionise transport in mountain and rural regions by providing a faster and more efficient alternative to conventional means such as trains and cars. The new aircraft, with its ability to take off and land vertically from rooftop vertiports, and to perform transition to fast forward flight, would be also extremely competitive in urban scenarios.

### 1.3.5 UAVs

The market of small electric unmanned vehicles is in constant growth and represents another context in which convertible concepts could gain a prominent position. Today's UAV industry is still struggling due to limited battery duration and long recharging times, and only by increasing vehicle performances the full potential of these machines can be exploited. Tilt-wing and tilt-rotor designs offer flexibility, performances and operational



**Figure 1.12:** Rendering of the electric tilt-wing aircraft being currently developed by Dufour Aerospace (Courtesy of Dufour Aerospace)

capabilities that are very desirable for unmanned aircraft. Therefore, convertible technology is being investigated for several missions such as monitoring and surveillance, search and rescue, surveying and mapping, smart farming, media and entertainment, law enforcements, and many more.

Application of tilt-rotor technology to bigger, military UAVs has also been considered. An early example is the Eagle Eye Unmanned Aerial Vehicle, developed by Bell Helicopter in the late 1990s.



**Figure 1.13:** The Bell Eagle Eye tilt-rotor UAV



## Chapter 2

# The XV-15 Tilt-Rotor Research Aircraft

### 2.1 General characteristics

The XV-15 Tilt-Rotor Research Aircraft (originally referred to as Bell Model 301) was developed by Bell Helicopter Textron starting from the early 1970s, in the context of a joint U.S. Army/NASA program aimed at providing a new proof-of-concept tilt-rotor technology demonstrator. It represented a significant evolution from its predecessor the XV-3, with different empennage configuration, more powerful gas turbine powerplants, an innovative transmission based on gears with herringbone tooth configuration, and a state-of-the-art flight control system.

The aircraft was sized to meet two requirements: first, it had to be large enough to meet expected performance, structural-dynamic reliability and maneuverability; secondly, it had to be small enough to be accommodated in the test section of NASA Ames 40 by 80-foot wind tunnel<sup>1</sup>. The result was a 12.8-metre long, 17.4-metre wide machine with two 25-foot (7.62-metre) diameter, three-bladed proprotors and a design gross weight of 13000 pounds (6000 kilograms). The wing, having a span of 10 metres and constant, 1.6-metre chord, was given a 6.5-degree forward sweep to obtain sufficient proprotor-to-wing clearance in airplane mode flight.

The aircraft was powered by two Lycoming T-53 turboshaft engines, modified by the manufacturer to provide overspeed capability and a two-minute contingency rating, in addition to adapting to the XV-15 configuration. The modified engine was designated as the LTC1K-4K, had a take-off power of 1550 shp and an emergency rating of 1802 shp. The free-turbine architecture allowed proprotor speed to be reduced from 589 to 517 rpm during airplane-mode flight, in order to improve performance and reduce cruise noise. Proprotors were driven by the engines through the main transmissions also located in each nacelle. The two proprotors were also linked together by a cross shaft system that allowed both rotors to continue to be powered even after the shut-down of one engine; upon the loss of a single engine during flight, this one was made free from the drive system by an automatic clutch.

As the tilt-rotor concept combines the flight characteristics of a conventional helicopter with those of a fixed-wing airplane, its flight control system had to blend the basic elements of these two modes. The flight deck of the XV-15 was configured so that each pilot station had complete controls for pitch, roll, yaw, and thrust in all modes of flight. In helicopter mode, the controls resembled those of a conventional lateral-tandem rotor helicopter, applying collective or cyclic blade pitch changes to the rotors to produce control moments

---

<sup>1</sup>Reference [15]



**Figure 2.1:** The XV-15 Tilt Rotor Research Aircraft flying in airplane mode (Reference [12])

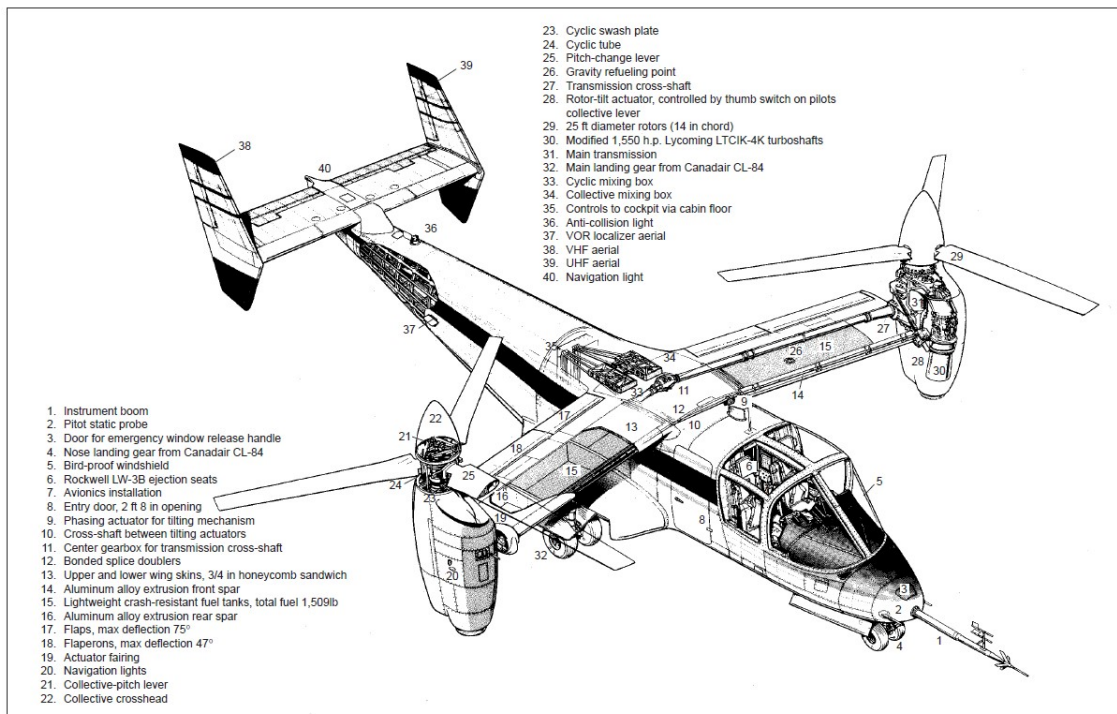


**Figure 2.2:** General layout and major components of the XV-15 (Reference [15])

and forces. Aircraft roll was produced through differential collective pitch, while differential cyclic pitch resulted in yaw motions. Moreover, to reduce the hover performance loss resulting from the proprotor wake impinging on the surface of the wing, the inboard flaps could be lowered to preset deflection positions. The outboard wing control surfaces, serving as ailerons in high speed flight, could also be deflected down when the flaps were deployed, though to a displacement less than two thirds of the flap position (such surfaces are referred to as "flaperons").

Conversion from vertical to forward flight and vice versa could be made within a wide range of airspeeds, conversion angles, and fuselage attitudes – resulting in a much wider conversion corridor than in previous technology demonstrators, and significantly reducing pilot workload during this delicate phase. While the fixed-wing control surfaces (ailerons, elevator, and rudder) remained active in all flight configurations, the rotor controls were automatically phased out as the nacelles were tilted toward the airplane configuration. This system was designed so that the need for control inputs during conversion were minimized. In addition, the XV-15 was provided with a Stability and Control Augmentation System (SCAS) incorporated within the aircraft design.

The nacelles were tilted by ball-screw-jack actuators with hydraulic motors and electric-powered servo valves. A triply redundant hydraulic power supply was provided for the conversion system because the XV-15 could not be landed in airplane mode without destroying the proprotor system. In the event of total electrical failure, the pilot still had mechanical access to hydraulic power to convert to helicopter mode. The conversion system shaft maintained both nacelles at the same angle and could also provide power to drive both nacelles to conversion in the event of total power failure on one side. In addition, conversion from helicopter to airplane mode could be stopped at any angle of tilting, with the possibility to perform steady flight at any point in the conversion range. The proprotor axes could rotate from a shaft angle of -5 degrees for rearward flight or autorotation, to 0 degrees position for hover and helicopter flight, and up to 90 degrees (horizontal) for typical airplane mode flight.

## 2.2 The rotor assembly

The XV-15 was equipped with two 25-foot diameter, three-bladed proprotors, with rectangular, 14-inch-chord blades made of stainless steel. Blade airfoils belonged to the NACA 64 series, with 8% thickness at the tip and 35% thickness at the theoretical root. The blades were twisted to provide high performance levels both in vertical and forward flight. Wire-wound tension-torsion straps retained each of the blades to a titanium yoke which in turn was gimbal-mounted to the mast. A nonrotating rubber hub-moment spring provided improved longitudinal control power. Finally, the rotor had cyclic and collective control through a pitch horn which was placed in a way to provide positive pitch-flap coupling, resulting in improved stability.

The three-bladed hub (Figure 2.4 installed in the XV-15 is generally called a "gimballed hub". In this configuration, the blades are rigidly connected with the hub, while the hub itself is linked to the shaft by a special joint which continually allows power transmission during tilting. The hub-to-shaft connection adopted in the XV-15 is commonly called a "universal joint" (a schematic representation is provided in Figure 2.5). This type of joint allows misalignment between the two shafts; however, such misalignment is generally designed to be rather small, as it introduces also two-per-revolution torsional vibrations<sup>2</sup>.

---

<sup>2</sup>Reference [12]

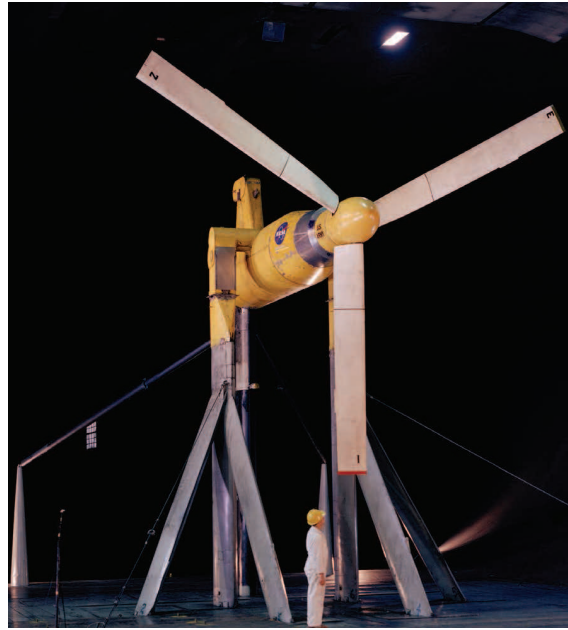


**Figure 2.3:** A single XV-15 proprotor in the 40- by 80-foot wind tunnel at NASA Ames Research Center (Reference [12])

The universal joint is not the only means to obtain a gimbaled hub: for example, in the V-22 a constant velocity joint was employed to attach the hub to the proprotor shaft.

## 2.3 The role of flight simulation

The one that led to the realization of the XV-15 Tilt-Rotor Research Aircraft was also one of the first programs in which flight simulation played a major role. Starting from the earliest phases of the program at the beginning of the 1970s, mathematical models were developed both at Boeing and Bell to provide preliminary concept evaluation and support to the design process.

By predicting the aircraft behaviour, these models allowed test pilots to evaluate the workload and handling qualities of the basic aircraft, both without automatic control-enhancing systems and with various control configurations, helping designers in the selection of the most suitable SCAS<sup>3</sup> control-enhancing algorithms. In addition, simulations enabled pilots to evaluate other factors, such as thrust/power management characteristics, the Force-Feel System (FFS), cockpit configuration, failure modes and effects, recovery procedures. Finally, piloted simulations were used as major evaluation and selection criteria by the U.S. Army and NASA, and it was also thanks to the results of these activities that the Bell Model 301 prevailed over the competing Boeing proposal<sup>4</sup>.

The XV-15 mathematical model was created by P. B. Harendra and M. J. Joglekar of Bell Helicopter Textron during the early 1970s, and implemented in Fortran environment on the GTRS/Sigma 8 flight simulator. It was conceived not only as an evaluation tool for a particular aircraft concept, but also as a device for developing improved generic tilt-rotor control laws and providing design guidance to subsequent projects. Initial piloted simulations were conducted in the NASA Ames Research Center Flight Simulator for Advanced Aircraft (FSAA) in November and December of 1973. The first test flight of a XV-15 prototype,

<sup>3</sup>Stability and Control Augmentation System

<sup>4</sup>Reference [15]

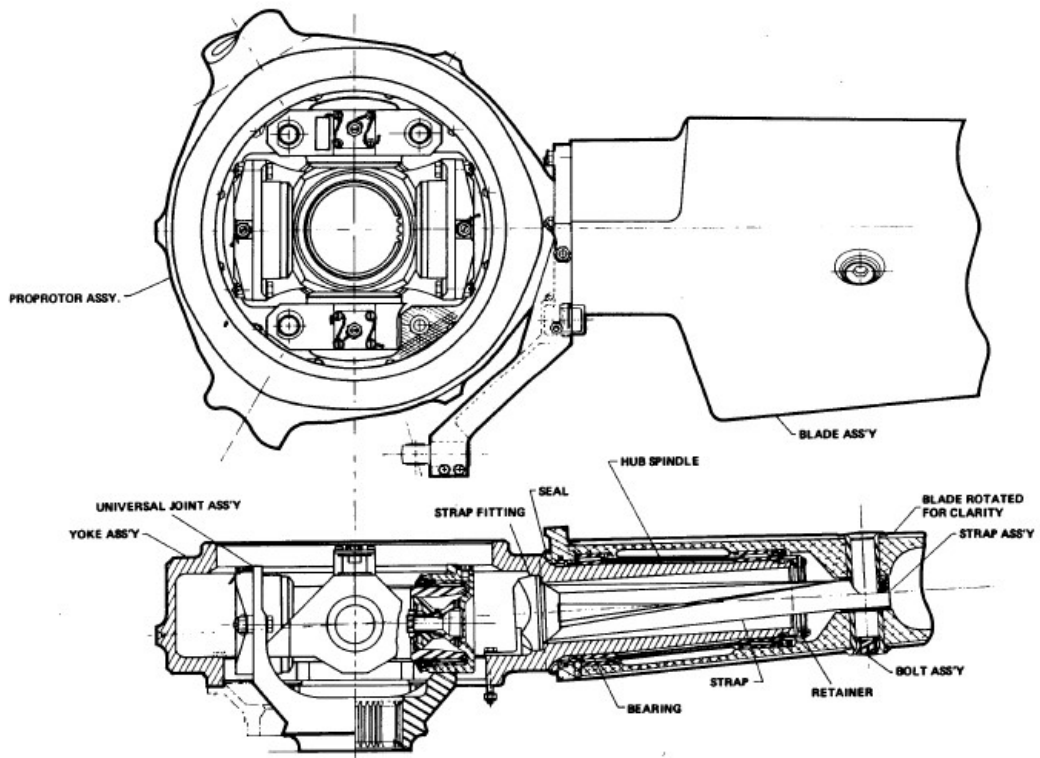


Figure 2.4: The XV-15 hub and blade-retention assembly (Reference [12])

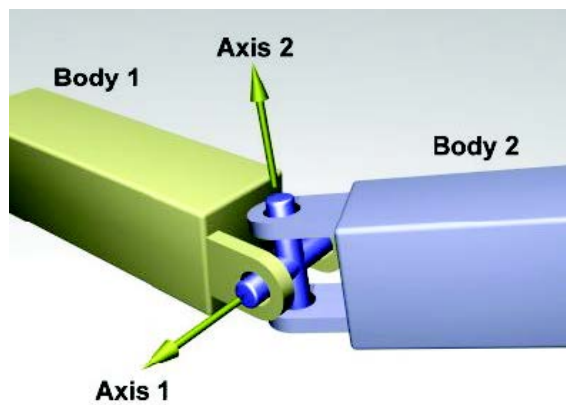
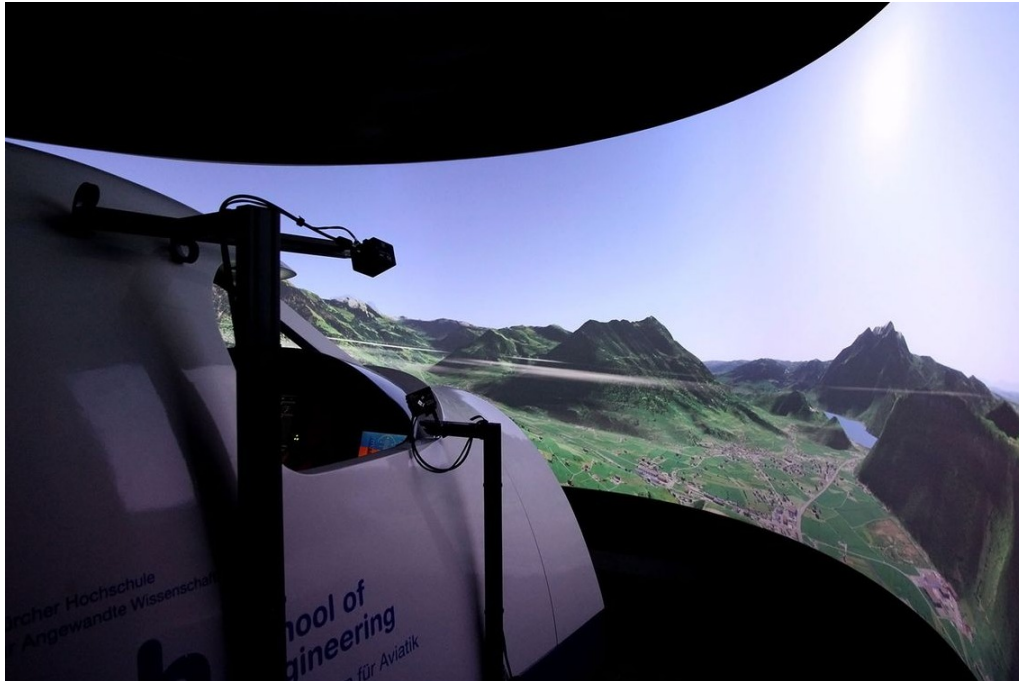


Figure 2.5: Scheme of the working principle of the hub universal joint (Reference [12])



**Figure 2.6:** View of the ReDSim flight simulator (Courtesy of ZAV)

in May 1977, demonstrated that, in general, the aircraft hovering behaviour reproduced almost exactly the predictions based on simulator evaluations, therefore clearly validating the simulation model. Data collected from the subsequent massive flight test activities carried out by the XV-15 were also used as a validation benchmark.

Through extensive development and refinement by Roger Marr and Samuel Ferguson in the 1980s, the XV-15 model eventually became the basis for a generic tilt-rotor mathematical model which has been employed in the Ames Vertical Motion Simulator to evaluate various tilt rotor aircraft designs (including the V-22) and related air traffic management issues. A description of this generic mathematical model is provided in NASA report CR-166536 (Reference [7]), while the model development and validation process is summarised in report CR-166537 (Reference [8]).

## 2.4 The ReDSim flight simulator at ZAV

The ZHAW Research and Didactics Simulator (ReDSim) is a flight simulator developed within the ZAV Centre for Aviation and operative since March 2011. The whole system was designed and integrated by ZAV personnel and by the students of ZHAW and has been constantly improved since 2011.

Thanks to the cockpit-like internal layout, a control loading system which allows to simulate a variety of feedback feel forces on pilot control, and a visual system with a 180-degree field of view, the flight simulator provides a highly realistic and immersive experience. ReDSim is used for educational activities and research as well as for industrial purposes together with partner companies such as Pilatus Aircraft Ltd. It is meant to be a universal platform, providing an interface with a wide range of aircraft models ranging from conventional fixed-wing airplanes and gliders to Unmanned Aerial Vehicle and Rotorcraft.

Notable features of the ReDSim (Figure 2.7) include:

- an airplane-like canopy under which the cockpit is installed;

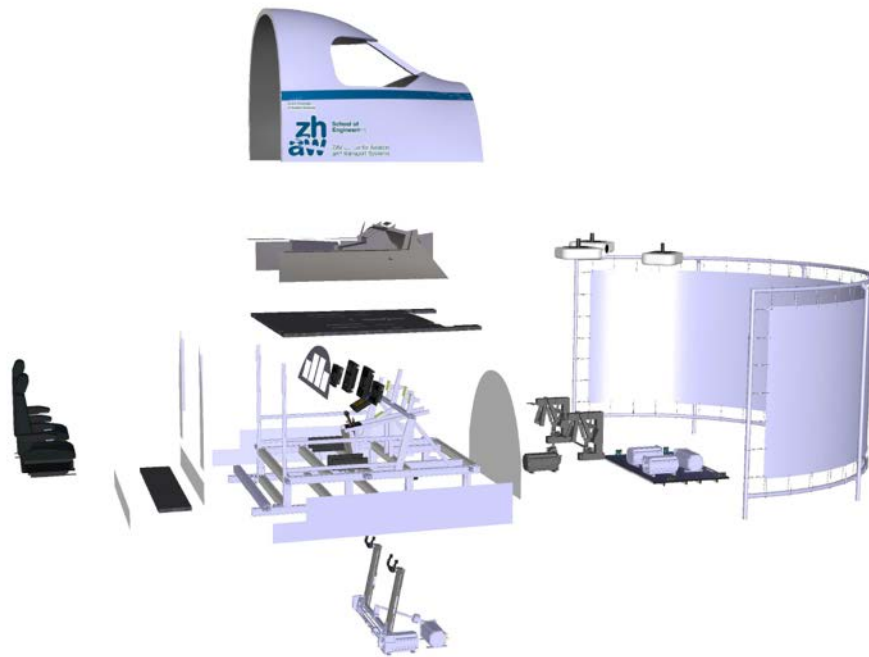


**Figure 2.7:** Scheme of the major ReDSim equipment (Courtesy of ZAV)

- a cockpit equipped with the traditional instrumentation of a conventional airplane (PFD, EFIS, ECAM, ...), plus a display showing selected simulation parameters;
- a Control Loadind Systems located under the deck and acting on the pilot controls;
- a visual system counting three projectors and a curved, 180-degree white screen.

The simulator is designed to run using either the Simulink environment or the simulation software DSix. A host computer runs the Simulink model and communicates with the visual system, the pilot station and the CLS host computer (Figure 2.8). To improve flexibility and provide less expert users with easier access to the simulator, the Simulink models can be run directly without need to generate any C code. Models that do not require different pilot controls set up can be quickly launched from the simulation host and set to run without any further modifications to the whole system; on the other hand, when implementation of different controls is needed, the simulator can be reconfigured and calibrated in one day.

#### 2.4.1 The XV-15 simulation model

A real-time tilt-rotor simulation model is available in the ReDSim, based on the original Bell/NASA XV-15 model described in Reference [7]. Development of the model was initiated in 2018 by Federico Barra, who reconstructed the whole mathematical model from report CR-166536 and adapted it for the Simulink environment of the ReDSim, in addition to performing a first series of validation activities. A description of all the activities carried out by Barra can be found in his Master's thesis, Reference [2].

The original rotor model was based on a combination of the Actuator Disk Theory and the Blade Element Theory; several simplifications had been made – for instance, small blade pitch and inflow angles as well as small flapping angles had been assumed, aerodynamic coefficients had been approximated as constant along the entire blade, and rotor inflow

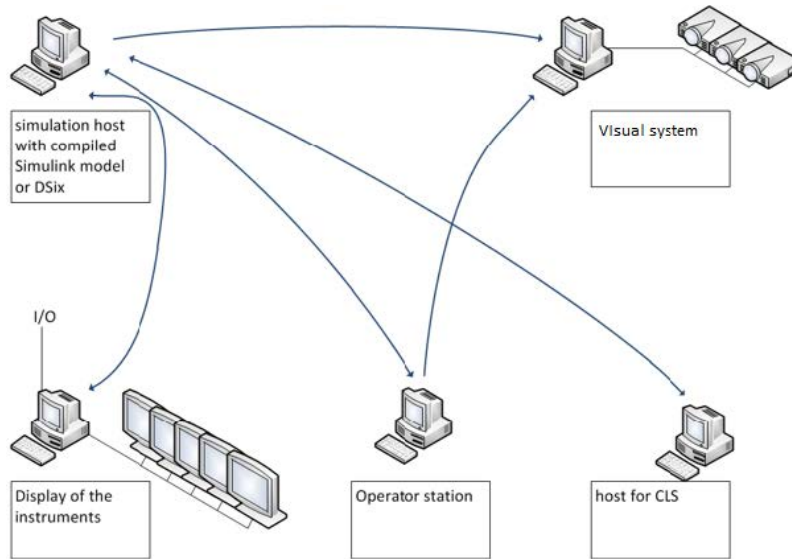


**Figure 2.8:** Schematic representation of the ReDSim hardware architecture (Reference [2])

dynamics had been neglected. In addition, many correction factors and customized terms had been introduced that best fit the model to experimental data, but made it also less suitable to application to other rotor configurations different from that of the XV-15. For these reasons, an entirely new, more accurate and more generic rotor model was deemed necessary. In 2019 Simone Godio, another Master student from Politecnico di Torino, proposed in his thesis (Reference [9]) a new multi-purpose rotor for implementation in the ZHAW ReDSim flight simulator. Further model refinement and development activities have been carried out by the author and are described in the present work.

## Chapter 3

# Review and development of the rotor mathematical model

A considerable portion of the activities carried out by the author during her period at ZHAW consisted in reviewing, debugging and refining the rotor model for the XV-15 flight simulator. Although the model had already been updated from the original one described in Reference [2]<sup>1</sup>, several simplifications and approximations were still present – most notably, the current formulation of flapping dynamics was not suitable to describe the behaviour of gimballed rotor such as the ones adopted in the XV-15. These factors, along with a few errors both in the mathematical formulation and in its implementation in the Simulink environment, negatively affected simulation accuracy and prevented trim algorithms from reaching convergence. As a result of the debugging and optimisation activities conducted by the author, the rotor gimbal is now taken into account and it has finally been possible to trim the model by means of the algorithm based on the Newton-Raphson method described in Section 3.3.

Developing a mathematical model for a real-time research flight simulator poses significant challenges as, on one side, maximum accuracy and fidelity must be achieved, but, on the other hand, complexity and computational costs must be limited to comply with the requirements for real-time simulation. Therefore, the present mathematical model has been formulated with the double goal to provide the closest possible representation of the aircraft actual behaviour with the minimum possible computational load. In addition, efforts have been made to preserve as much as possible the multi-purpose nature of the model, so as to allow the same model to be also used, with minimum changes, for simulation of other rotor types and configurations.

### 3.1 General description

#### 3.1.1 Reference frames

One of the first and most important steps to take when approaching the description of a dynamic system is choosing a suitable frame of reference. In the case at hand, different degrees of freedom must be taken into account, as each rotor, besides translating and rotating in space along with the entire aircraft, revolves around the hub, and each rotor blade, additionally, is free to flap. The resulting motion is rather complex, and difficult to describe using only one reference system. Therefore, the following three reference frames have been adopted:

---

<sup>1</sup>See Section 2.4.1 and Reference [9]

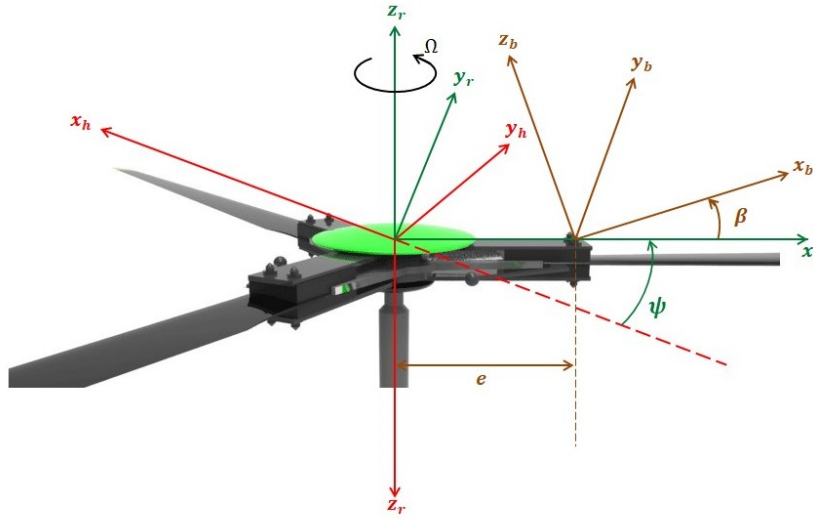


**Figure 3.1:** Reference frames for the right rotor

**Hub** – Fixed, centered in the rotor hub, with:

- $x_h$  in the hub plane and positive forward;
- $y_h$  in the hub plane and positive outboard (starboard for the right rotor, port for the left rotor);
- $z_h$  perpendicular to the hub plane and positive downwards.

**Rotating** – Centered in the rotor hub, rotating with angular speed equal to  $\Omega$ , and having:

- $x_r$  coincident with the projection of the blade axis on the hub plane and positive outwards;
- $z_r$  perpendicular to the hub plane and positive upwards;
- $y_r$  perpendicular to  $x_r$  and  $z_r$  (hence positive in the blade advancing direction).

**Blade** – Centered in the blade flapping hinge, rotating with angular speed equal to  $-\dot{\beta}$ ; its axes are:

- $x_b$  coincident with the blade axis and positive from the flapping hinge to the blade tip;
- $y_b$  parallel to  $y_r$  (perpendicular to the blade and positive in its advancing direction);
- $z_b$  perpendicular to  $x_b$  and  $y_b$ .

Figure 3.1 shows the layout of the three reference frames for the right rotor.

Conversion between different reference frames is obtained by means of the following rotation matrices:

- From Blade system to Rotating system:

$$\mathbf{T}_\beta = \begin{bmatrix} \cos \beta & 0 & -\sin \beta \\ 0 & 1 & 0 \\ \sin \beta & 0 & \cos \beta \end{bmatrix}$$

Where  $\beta$  is the blade flapping angle (i.e. the angle between  $x_b$  and  $x_r$ ), positive when the blade flaps upwards.

- From Rotating system to Hub system:

$$\mathbf{T}_\psi = \begin{bmatrix} -\cos \psi & \sin \psi & 0 \\ \sin \psi & \cos \psi & 0 \\ 0 & 0 & -1 \end{bmatrix}$$

Where  $\psi = \Omega t$  is the blade azimuth angle, i.e. the angle between  $x_r$  and the negative direction of  $x_h$ , and is positive according to the direction of the rotor angular speed  $\Omega$  (counter-clockwise for the right rotor, clockwise for the left rotor).

It can be easily observed that the reference systems for the left and right rotor are completely symmetrical about the aircraft longitudinal plane; moreover, the frame of reference adopted for the right rotor has right-handed coordinates, while the one adopted for the left rotor has left-handed coordinates. After a careful comparison of several different options, this particular configuration has proved to be the best one in terms of simplicity and ease when implementing the mathematical model into the XV-15 Simulink model: in fact<sup>2</sup>, it makes it possible to use the exact same library block for both the left and right rotor, requiring only a limited number of minor changes to model inputs and outputs to comply with the different sign conventions.

### 3.1.2 Rotor aerodynamics

Description of the rotor aerodynamic behaviour is based on the Blade Element Theory<sup>3</sup>: each rotor blade is divided into a finite number of sections, the aerodynamic loads being determined for each section and then integrated along the blade span.

To reduce the complexity and computational cost of the model, a two-dimensional analysis is conducted for each section, thus neglecting the reciprocal influence between the sections, as well as all the blade tip effects. For the same reason, flow compressibility is also not taken directly into account. However, effects of tip-loss and Mach number are evaluated as a function of the radial position along the blade using semi-empirical polynomial laws, by means of which corrective coefficients are obtained; the aerodynamic forces obtained with the Blade Element Theory are then multiplied by these coefficients to improve model accuracy.

The aerodynamic forces generated by a generic blade section are represented in Figure 3.2. Only lift and drag are considered in the present model, while the pitching moment about the aerodynamic centre is neglected.

In order to compute the aerodynamic forces, the angle of attack of each blade section must be determined. The latter is made up by the sum of different contributions:

$$\alpha = \vartheta_{\text{twist}} + \vartheta_{\text{pitch}} - K_1\beta - \alpha_0 + \phi \quad (3.1)$$

where:

- $\vartheta_{\text{twist}}$  is the twist angle, computed as a function of the position along  $x_b$  through a polynomial law;

---

<sup>2</sup>For further details, see Section 4.2

<sup>3</sup>Reference [14], [10]

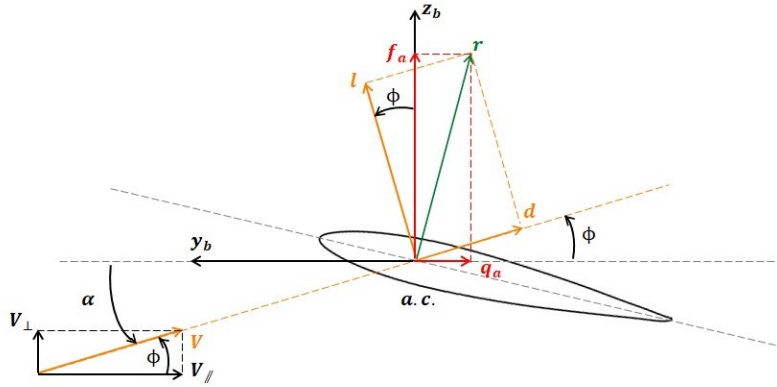


**Figure 3.2:** Sketch of a generic blade section

- $\vartheta_{\text{pitch}}$  is the blade pitch angle commanded by the pilot:

$$\vartheta_{\text{pitch}} = \vartheta_0 - A_1 \cos \psi - B_1 \sin \psi$$

where  $\vartheta_0$ ,  $A_1$  and  $B_1$  are, respectively, the collective pitch, the lateral and the longitudinal cyclic;

- $K_1 = \tan \delta_3$  is the pitch-flap coupling coefficient;
- $\alpha_0$  is the zero-lift angle of attack;
- $\phi$  is the inflow angle.

The inflow angle identifies the direction of the airflow affecting the blade section, and can in turn be expressed as:

$$\phi = \arctan \frac{V_{\perp}}{V_{\parallel}}$$

$V_{\perp}$  is the component of the airflow speed, in wind axes, which is perpendicular to the blade section; to determine it, the following three effects are taken into account:

- blade motion;
- rotor inflow speed;
- the influence of pitch dynamics (which is not modeled in the present case), approximated as  $x_{\text{uo}} \dot{\vartheta}_{\text{pitch}}$  (with  $x_{\text{uo}} = 0.25c$ ).

$V_{\parallel}$  is the component of the airflow speed, in wind axes, parallel to the blade section, for which only blade motion is taken into account.

Both  $V_{\perp}$  and  $V_{\parallel}$  are non-linear functions of the blade flapping angle  $\beta$  and of the flapping speed  $\dot{\beta}$ , thus making also  $\phi$  and  $\alpha$  non-linear functions of  $\beta$  and  $\dot{\beta}$ . To facilitate solution of the flapping dynamics equation, as well as interpolation of aerodynamic coefficients, a linearisation of these functions needs to be operated.

Assuming small flapping angles, it is possible to write:

$$\sin \beta \approx \beta$$

$$\cos \beta \approx 1$$

By applying the above approximation to the expressions of  $V_{\perp}$  and  $V_{\parallel}$ , two linear functions of  $\beta$  and  $\dot{\beta}$  are obtained. Since  $\phi$  is in its turn a non-linear function of  $V_{\perp}$  and  $V_{\parallel}$ , it is linearised by means of a first-order Taylor expansion around the point  $(\beta = 0, \dot{\beta} = 0)$ :

$$\phi(\beta, \dot{\beta}) \approx \phi(\beta=0, \dot{\beta}=0) + \left. \frac{\partial \phi}{\partial \dot{\beta}} \right|_{\substack{\beta=0 \\ \dot{\beta}=0}} \dot{\beta} + \left. \frac{\partial \phi}{\partial \beta} \right|_{\substack{\beta=0 \\ \dot{\beta}=0}} \beta$$

This way, the inflow angle becomes a linear function having the following form:

$$\phi = \phi_1 \dot{\beta} + \phi_2 \beta + \phi_3$$

Which, substituted into Equation 3.1, yields:

$$\alpha = \alpha_1 \dot{\beta} + \alpha_2 \beta + \alpha_3$$

where:

$$\begin{aligned} \alpha_1 &= \phi_1 \\ \alpha_2 &= -K_1 + \phi_2 \\ \alpha_3 &= \vartheta_{\text{twist}} + \vartheta_0 - A_1 \cos \psi - B_1 \sin \psi - \alpha_0 + \phi_3 \end{aligned}$$

The airfoil lift and drag polar curves being known<sup>4</sup>, the value of  $\alpha$  just obtained can be now used to determine the lift and drag coefficients for each blade section. Again, since both  $C_l$  and  $C_d$  depend on  $\alpha$  and the latter is a function of  $\beta$  and  $\dot{\beta}$ , their expressions are linearised using a first-order Taylor expansion in the neighbourhood of  $(\beta = 0, \dot{\beta} = 0)$ :

$$\begin{aligned} C_l &\approx C_l(\beta=0, \dot{\beta}=0) + \left. \frac{\partial C_l}{\partial \dot{\beta}} \right|_{\substack{\beta=0 \\ \dot{\beta}=0}} \dot{\beta} + \left. \frac{\partial C_l}{\partial \beta} \right|_{\substack{\beta=0 \\ \dot{\beta}=0}} \beta = \\ &= C_l \Big|_{\substack{\beta=0 \\ \dot{\beta}=0}} + \left. \frac{dC_l}{d\alpha} \frac{\partial \alpha}{\partial \dot{\beta}} \right|_{\substack{\beta=0 \\ \dot{\beta}=0}} \dot{\beta} + \left. \frac{dC_l}{d\alpha} \frac{\partial \alpha}{\partial \beta} \right|_{\substack{\beta=0 \\ \dot{\beta}=0}} \beta = \\ &= C_l \Big|_{\substack{\beta=0 \\ \dot{\beta}=0}} + C_{l\alpha} \Big|_{\substack{\beta=0 \\ \dot{\beta}=0}} \alpha_1 \dot{\beta} + C_{l\alpha} \Big|_{\substack{\beta=0 \\ \dot{\beta}=0}} \alpha_2 \beta \end{aligned}$$

$$\begin{aligned} C_d &\approx C_d(\beta=0, \dot{\beta}=0) + \left. \frac{\partial C_d}{\partial \dot{\beta}} \right|_{\substack{\beta=0 \\ \dot{\beta}=0}} \dot{\beta} + \left. \frac{\partial C_d}{\partial \beta} \right|_{\substack{\beta=0 \\ \dot{\beta}=0}} \beta = \\ &= C_d \Big|_{\substack{\beta=0 \\ \dot{\beta}=0}} + \left. \frac{dC_d}{d\alpha} \frac{\partial \alpha}{\partial \dot{\beta}} \right|_{\substack{\beta=0 \\ \dot{\beta}=0}} \dot{\beta} + \left. \frac{dC_d}{d\alpha} \frac{\partial \alpha}{\partial \beta} \right|_{\substack{\beta=0 \\ \dot{\beta}=0}} \beta = \\ &= C_d \Big|_{\substack{\beta=0 \\ \dot{\beta}=0}} + C_{d\alpha} \Big|_{\substack{\beta=0 \\ \dot{\beta}=0}} \alpha_1 \dot{\beta} + C_{d\alpha} \Big|_{\substack{\beta=0 \\ \dot{\beta}=0}} \alpha_2 \beta \end{aligned}$$

Once  $\phi$ ,  $\alpha$  and the aerodynamic coefficients are known, the aerodynamic forces can finally be computed. The lift and drag generated by each blade section are, respectively:

$$\begin{aligned} dl &= \frac{1}{2} \rho V^2 c C_l dr \\ dd &= \frac{1}{2} \rho V^2 c C_d dr \end{aligned}$$

---

<sup>4</sup>The method employed to derive the complete airfoil aerodynamic polar curves from available data is described in Section 4.3.1.

Where  $V = \sqrt{V_{\perp}^2 + V_{\parallel}^2}$  is the airflow speed. By projecting the lift and drag into the Blade reference frame, the following forces and moments are obtained:

- aerodynamic force along  $z_b$ :

$$df_a = dd \sin \phi + dl \cos \phi = \frac{1}{2} \rho V^2 c (C_d \sin \phi + C_l \cos \phi) dr$$

- aerodynamic force along  $-y_b$ :

$$dq_a = dd \cos \phi - dl \sin \phi = \frac{1}{2} \rho V^2 c (C_d \cos \phi - C_l \sin \phi) dr$$

- aerodynamic moment around  $-y_b$ :

$$dm_a = df_a r = \frac{1}{2} \rho V^2 c (C_d \sin \phi + C_l \cos \phi) r dr$$

- aerodynamic moment  $-z_b$ :

$$dn_a = dq_a r = \frac{1}{2} \rho V^2 c (C_d \cos \phi - C_l \sin \phi) r dr$$

The overall aerodynamic loads generated by each blade are subsequently obtained by integrating the above forces and moments along the whole length of the blade:

$$\begin{aligned} F_a &= \int_0^R df_a dr \\ Q_a &= \int_0^R dq_a dr \\ M_a &= \int_0^R dm_a dr \\ N_a &= \int_0^R dn_a dr \end{aligned}$$

### 3.1.3 Flapping dynamics

In order to express the flapping dynamics equation in a linear form, the assumption of small flapping angles has been made. An analysis of the validity of this hypothesis can be found in Reference [6]. As far as the XV-15 proprotors are concerned, it is actually acceptable to consider small flapping angles since, for safety reasons, their  $\beta$  was limited to a range of  $\pm 12^\circ$ .

The flapping equation is written for each blade by imposing dynamical equilibrium of the rotation around the flapping hinge, in the Blade reference frame. All the loads acting on the blade must be taken into account – namely:

- The aerodynamic moment  $M_a$ , which, applying the linearisation described in Section 3.1.2, can be expressed as a linear function of  $\beta$  and  $\dot{\beta}$ :

$$M_a = M_1 \dot{\beta} + M_2 \beta + M_3$$

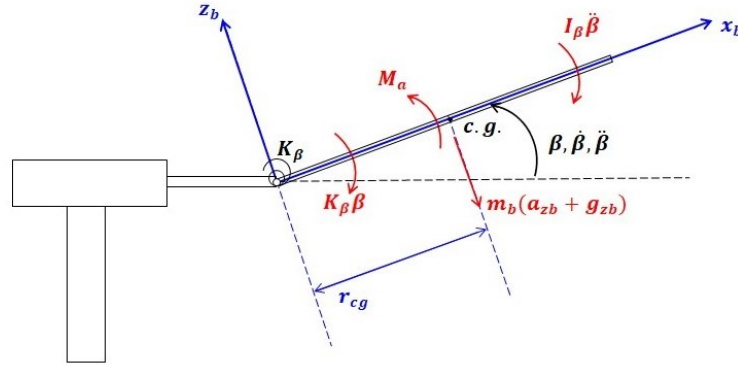


**Figure 3.3:** Sketch of the forces involved in the blade flapping dynamics

- Blade inertia; by applying the hypothesis of small flapping angles, the blade acceleration along  $z_b$  becomes a linear function of  $\beta$  and  $\ddot{\beta}$ , having the form:

$$a_z = r\ddot{\beta} + a_{z2}\beta + a_{z3}$$

The inertial torque acting on the blade can therefore be written as:

$$F_I = I_\beta\ddot{\beta} + m_b r_{cg}(a_{z2}\beta + a_{z3})$$

- Blade weight, supposed to be concentrated in the centre of gravity of the blade itself.
- The elastic torque generated by the flapping hinge; for the sake of model simplicity, the latter can be approximated as a torsional spring having a stiffness equal to  $K_\beta$ .

The equation thus obtained can be reduced to the typical form of second-order differential equations describing a driven oscillating dynamic system:

$$m\ddot{\beta} + c\dot{\beta} + k\beta = F_\beta \quad (3.2)$$

where:

$$\begin{aligned} m &= I_\beta \\ c &= -M_1 \\ k &= -M_2 + m_b r_{cg} a_{z2} + K_\beta \\ F_\beta &= M_3 - m_b r_{cg}(a_{z3} + g_z) \end{aligned}$$

It is interesting to note that, in this simple model applicable to generic articulated as well as elastic rotors, the flapping dynamics equations obtained for each blade are independent from one another – which means that the flapping behaviour of each blade is not influenced by the motion of the other blades. On the other hand, as will be described in detail in Section 3.2, the situation changes when a gimbaled rotor is considered, leading to a linear system of differential equations in which the  $\beta$  of each blade is also a function of the other blades flapping angles.

### 3.1.4 Multi-blade coordinates

Integration of the flapping dynamics equation leads to the determination of  $\beta$ ,  $\dot{\beta}$  and  $\ddot{\beta}$  for each rotor blade. Using the multi-blade coordinates<sup>5</sup> transformation, it is possible to write the flapping angle at each time instant as a function of the azimuth angle:

$$\beta = \beta_0 + \beta_{1s} \sin \psi + \beta_{1c} \cos \psi \quad (3.3)$$

with  $\beta_0$ ,  $\beta_{1s}$  and  $\beta_{1c}$  computed as follows:

$$\begin{aligned} \beta_0 &= \frac{1}{N} \sum_{j=1}^N \beta_j \\ \beta_{1s} &= \frac{2}{N} \sum_{j=1}^N \beta_j \sin \psi_j \\ \beta_{1c} &= \frac{2}{N} \sum_{j=1}^N \beta_j \cos \psi_j \end{aligned}$$

where  $N$  is the number of rotor blades. The angles  $\beta_{1s}$  and  $\beta_{1c}$  identify the orientation of the rotor tip-path-plane.

A similar formulation to that of the flapping angle can also be obtained for the flapping angular speed  $\dot{\beta}$ , by simply deriving Equation 3.3:

$$\dot{\beta} = \dot{\beta}_{1s} \sin \psi + \dot{\beta}_{1c} \cos \psi$$

Where:

$$\begin{aligned} \dot{\beta}_{1s} &= \frac{2}{N} \sum_{j=1}^N \dot{\beta}_j \sin \psi_j \\ \dot{\beta}_{1c} &= \frac{2}{N} \sum_{j=1}^N \dot{\beta}_j \cos \psi_j \end{aligned}$$

As will be described in detail in 3.2, multi-blade coordinates will play a major role in the formulation of the flapping dynamics equation for a gimbaled rotor.

### 3.1.5 Hub loads

The loads transmitted by each rotor to the airframe constitute the main output of the rotor model, and are of fundamental importance for the integration of the rotor model into the overall aircraft simulation model, as well as the evaluation of rotor and aircraft performance. To determine them, it is necessary to consider all the forces and moments to which each blade is subject, such as:

- aerodynamic loads;
- blade inertia;
- blade weight;
- forces and moments generated by the flapping hinge.

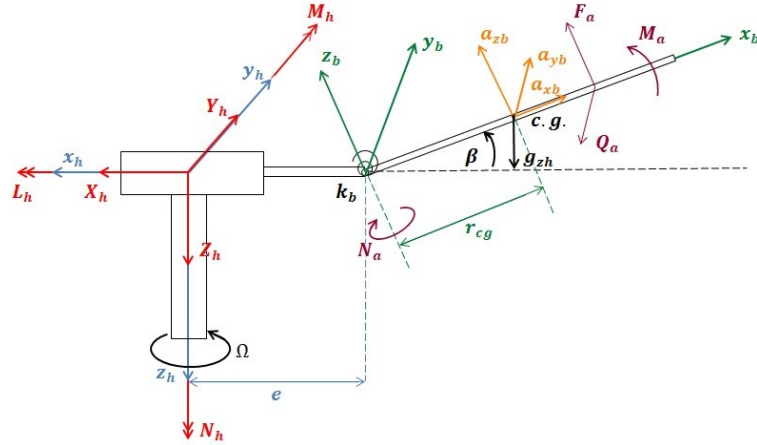


**Figure 3.4:** Forces and moments acting on each blade

Inertial and gravitational loads are assumed to be concentrated in the blade centre of gravity. In addition, no approximation of small flapping angles is made when evaluating blade speed and acceleration.

The method<sup>6</sup> adopted to compute hub loads for each rotor can be summarised in the following steps:

1. Once all forces and moments acting on each single blade are determined, the constraint reactions in the flapping hinge can be computed as:

$$\vec{R} = \vec{F}_{\text{ext}} - m_b \vec{a}_{\text{cg}} - \vec{F}_{\text{int}}$$

Where  $\vec{F}_{\text{ext}}$  denotes the external loads (i.e. those related to aerodynamics and gravity),  $\vec{F}_{\text{int}}$  indicates the internal loads produced by the flapping hinge, and  $\vec{a}_{\text{cg}}$  is the acceleration of the blade center of gravity.

2. Due to Newton's third law of motion, the loads transmitted by the flapping hinge to the rest of the aircraft, in the Blade reference frame, are simply:

$$\vec{F} = -\vec{R}$$

3. The vector  $\vec{F}$  obtained for each blade is transported to the center of the rotor hub and referred to the Hub frame of reference.
4. The overall hub loads are computed by summing up contributions from each blade.

Thus, the following forces and moments – directed, respectively, along  $x_h$ ,  $y_h$  and  $z_h$  – are obtained:<sup>7</sup>

$$\begin{aligned} \text{forces:} & \quad X_h, Y_h, Z_h \\ \text{moments:} & \quad L_h, M_h, N_h \end{aligned}$$

<sup>5</sup>Reference [19]

<sup>6</sup>Reference [10], [4]

<sup>7</sup>For the detailed expressions, see Appendix A.4

It is now possible to determine the thrust generated by each rotor:

$$T = \sqrt{X_h^2 + Y_h^2 + Z_h^2}$$

While the required torque is:

$$P = N_h$$

Both the above quantities can be expressed in a non-dimensional form by introducing the thrust and torque coefficients:

$$C_T = \frac{T}{\pi\rho\Omega^2 R^4} \quad C_P = \frac{P}{\pi\rho\Omega^2 R^5}$$

### 3.1.6 Inflow dynamics

Rotor dynamic inflow is modelled according to the formulation introduced by Pitt and Peters<sup>8</sup>. The following distribution is assumed for the non-dimensional flow velocity ( $\lambda = v_{\text{inflow}}/\Omega R$ ) induced by the rotor in the direction perpendicular to the tip-path-plane:

$$\lambda = \lambda_0 + \frac{r}{R}\lambda_{1s}\sin\psi + \frac{r}{R}\lambda_{1c}\cos\psi$$

In the above expression, rotor inflow velocity is defined within a reference system centered in the rotor hub, with the  $x$ - $y$  plane parallel to the tip-path-plane; conversion between this system and the Hub reference frame can be easily accomplished using the following rotation matrix:

$$\mathbf{T}_{HA} = \begin{bmatrix} \cos\beta_{1c} & \sin\beta_{1c}\sin\beta_{1s} & \sin\beta_{1c}\cos\beta_{1s} \\ 0 & \cos\beta_{1s} & -\sin\beta_{1s} \\ -\sin\beta_{1c} & \cos\beta_{1c}\sin\beta_{1s} & \cos\beta_{1c}\cos\beta_{1s} \end{bmatrix}$$

The Pitt-Peters formulation establishes a correlation between the inflow velocity components and the aerodynamic loads generated by the rotor; such correlation is described by the following differential equation:

$$\mathbf{M}_{pp} \begin{Bmatrix} \dot{\nu}_0 \\ \dot{\nu}_{1s} \\ \dot{\nu}_{1c} \end{Bmatrix} + \mathbf{L}_{pp}^{-1} \begin{Bmatrix} \nu_0 \\ \nu_{1s} \\ \nu_{1c} \end{Bmatrix} = \begin{Bmatrix} C_t \\ C_l \\ C_m \end{Bmatrix} \quad (3.4)$$

Where:

- $\nu_0$ ,  $\nu_{1s}$  and  $\nu_{1c}$  are the inflow velocity components in a reference frame which is still parallel to the tip-path-plane, but whose  $x$  axis is aligned with the aircraft speed:

$$\begin{Bmatrix} \nu_0 \\ \nu_{1s} \\ \nu_{1c} \end{Bmatrix} = \begin{bmatrix} \cos\beta_h & \sin\beta_h & 0 \\ -\sin\beta_h & \cos\beta_h & 0 \\ 0 & 0 & 1 \end{bmatrix} \begin{Bmatrix} \lambda_0 \\ \lambda_{1s} \\ \lambda_{1c} \end{Bmatrix}$$

$\beta_h$  being the sideslip angle.

- $C_t$ ,  $C_l$  and  $C_m$  are non-dimensional coefficients corresponding, respectively, to the aerodynamic vertical force, rolling moment and pitching moment generated by the rotor – again in the same reference system in which  $\nu$  is defined.

---

<sup>8</sup>Reference [18], [19]

- Matrices  $\mathbf{M}_{pp}$  and  $\mathbf{L}_{pp}$  are derived from semi-empirical considerations and are defined as follows:

$$\mathbf{M}_{pp} = \frac{1}{\Omega} \begin{bmatrix} \frac{128}{75\pi} & 0 & 0 \\ 0 & -\frac{16}{45\pi} & 0 \\ 0 & 0 & -\frac{16}{45\pi} \end{bmatrix}$$

$$\mathbf{L}_{pp} = \begin{bmatrix} \frac{1}{2v_t} & 0 & \frac{15\pi}{64v_m} \tan \frac{\chi}{2} \\ 0 & -\frac{4}{v_m(1 + \cos \chi)} & 0 \\ \frac{15\pi}{64v_t} \tan \frac{\chi}{2} & 0 & -\frac{4 \cos \chi}{v_m(1 + \cos \chi)} \end{bmatrix}$$

with:

$$v_t = \sqrt{\mu^2 + (\lambda_0 - \mu_z)^2}$$

$$v_m = \frac{\mu^2 + (\lambda_0 - \mu_z)(2\lambda_0 - \mu_z)}{v_t}$$

$$\chi = \arctan \frac{\mu}{\lambda_0 - \mu_z}$$

$\mu$  and  $\mu_z$  being the horizontal and vertical advance ratio, computed as:

$$\mu = \frac{\sqrt{u^2 + v^2}}{\Omega R} \quad \mu_z = \frac{w}{\Omega R}$$

Rotor inflow velocity components in the Hub reference frame are obtained by integrating Equation 3.4 and operating the necessary coordinate transformations. These results are necessary to compute the inflow angle  $\phi$  for each blade section, leading to the determination of rotor aerodynamic loads; in addition, they are also essential for the evaluation of induced velocities in all those areas in the aircraft which affected by rotor wake.

## 3.2 Gimbal model

The dynamic behaviour of gimballed rotors is very complex, making it extremely challenging to build a model capable of simulating it in an accurate way. Unlike in other rotor types, the blades of a gimballed rotor are not free to flap independently from one another, being all linked rigidly to the rotor hub. However, a certain degree of independence is conserved, due either to the presence of a hub coning hinge or to the intrinsic flexibility of the structure itself.

The strictest way to model the flapping dynamics of this complicated mechanism would require that the dynamics of all blades and their couplings are included in the formulation of the dynamical problem<sup>9</sup>. On the other hand, such a method would increase significantly the complexity and computational cost of the model, very likely resulting in the impossibility to perform a real-time simulation.

Therefore, a different approach has been sought, capable of affording at the same time a realistic description of the system at hand and compliance with the requirements for a real-time simulation. In the formulation described hereafter, instead of explicitly modelling the gimbal, the kinematic constraint on the blades is taken into account by introducing the following two assumptions:

---

<sup>9</sup>Reference [16]

- The flapping angle of each blade is computed by adding to the gimbal attitude,  $\beta_G$ , another contribution  $\Delta\beta$ , representing the variations of flapping angle in each blade due to structure flexibility or to a coning hinge:

$$\beta_j = \beta_{Gj} + \Delta\beta_j \quad j = 1, \dots, N$$

- The gimbal plane is assumed to be parallel to the rotor tip-path-plane – hence:

$$\beta_{Gj} = \beta_0 + \beta_{1s} \sin \psi_j + \beta_{1c} \cos \psi_j \quad j = 1, \dots, N$$

Strictly speaking, the second hypothesis would be verified only if  $\Delta\beta$  was identically null; however, it constitutes all the same an acceptable approximation, considering that the coning stiffness of the XV-15 rotor hub is in the order of  $10^5 \text{ Nm deg}^{-1}$ .

By evaluating  $\beta_G$  for each blade, and substituting in its expression the definitions of the multi-blade coordinates, the following identity is obtained:

$$\begin{Bmatrix} \beta_{G1} \\ \beta_{G2} \\ \vdots \\ \beta_{GN} \end{Bmatrix} = \frac{2}{N} \begin{bmatrix} 1 & \cos(\beta_2 - \beta_1) & \dots & \cos(\beta_N - \beta_1) \\ \cos(\beta_1 - \beta_2) & 1 & \dots & \cos(\beta_N - \beta_2) \\ \vdots & \vdots & \ddots & \vdots \\ \cos(\beta_1 - \beta_N) & \cos(\beta_2 - \beta_N) & \dots & 1 \end{bmatrix} \begin{Bmatrix} \beta_1 \\ \beta_2 \\ \vdots \\ \beta_N \end{Bmatrix}$$

or, more, concisely:

$$\beta_G = \mathbf{B}_\psi \cdot \beta \quad (3.5)$$

Where

$$\mathbf{B}_{\psi_{i,j}} = \frac{2}{N} \cos(\psi_j - \psi_i) \quad i, j = 1, \dots, N$$

Since the azimuth angle for each blade is given by:

$$\psi_j = \Omega t + \frac{(j-1)2\pi}{N} \quad j = 1, \dots, N$$

it is also possible to write:

$$\mathbf{B}_{\psi_{i,j}} = \frac{2}{N} \cos\left(\frac{(j-i)2\pi}{N}\right) \quad i, j = 1, \dots, N$$

Therefore,  $\beta_G$  is related to the blade flapping angle  $\beta$  through a matrix whose coefficients are constant in time and depend only on the number of blades. In an analogous way,

$$\dot{\beta}_G = \mathbf{B}_\psi \cdot \dot{\beta}$$

The flapping dynamics equation for each blade is written in the following form:

$$m\ddot{\beta} + c\dot{\beta} + c_{\text{struct}}\Delta\dot{\beta} + k\beta + k_G\beta_G + k_\beta\Delta\beta = F_\beta$$

where:

- $m$ ,  $c$  and  $F_\beta$  are unchanged with respect to what described in Section 3.1.3:

$$\begin{aligned} m &= I_\beta \\ c &= -M_1 \\ F_\beta &= M_3 - m_b r_{\text{cg}}(a_{z3} + g_z) \end{aligned}$$

- $k$  contains the contributions of aerodynamic and inertial loads to system stiffness:

$$k = -M_2 + m_b r_{cg} a_{z2}$$

- $c_{struct}$  takes into account the system structural damping;<sup>10</sup>
- $k_G$  is the torsional stiffness of the gimbal joint;
- $k_\beta$  can represent either the stiffness of the hub coning hinge (if present), or the structural stiffness.

By substituting  $\Delta\beta = \beta - \beta_G$  and Equation 3.5 in the flapping dynamics equation, and rewriting everything in matrix form, an equation in the following form<sup>11</sup> is obtained:

$$\mathbf{M}\ddot{\beta} + \mathbf{C}\dot{\beta} + \mathbf{K}\beta = \mathbf{F}_\beta \quad (3.6)$$

For a three-bladed rotor such as the XV-15 one, in particular, Equation appears as follows:

$$\begin{aligned} & \begin{bmatrix} I_\beta & 0 & 0 \\ 0 & I_\beta & 0 \\ 0 & 0 & I_\beta \end{bmatrix} \begin{Bmatrix} \ddot{\beta}_1 \\ \ddot{\beta}_2 \\ \ddot{\beta}_3 \end{Bmatrix} + \frac{1}{3} \begin{bmatrix} 3c_1 + c_{struct} & c_{struct} & c_{struct} \\ c_{struct} & 3c_2 + c_{struct} & c_{struct} \\ c_{struct} & c_{struct} & 3c_3 + c_{struct} \end{bmatrix} \begin{Bmatrix} \dot{\beta}_1 \\ \dot{\beta}_2 \\ \dot{\beta}_3 \end{Bmatrix} + \\ & + \frac{1}{3} \begin{bmatrix} 2k_G + 3k_1 + k_\beta & k_\beta - k_G & k_\beta - k_G \\ k_\beta - k_G & 2k_G + 3k_2 + k_\beta & k_\beta - k_G \\ k_\beta - k_G & k_\beta - k_G & 2k_G + 3k_3 + k_\beta \end{bmatrix} \begin{Bmatrix} \beta_1 \\ \beta_2 \\ \beta_3 \end{Bmatrix} = \begin{Bmatrix} F_{\beta_1} \\ F_{\beta_2} \\ F_{\beta_3} \end{Bmatrix} \quad (3.7) \end{aligned}$$

The dynamical problem is thus completely described by a linear system of second-order differential equations in which the only unknowns are the flapping angles of each blade. As anticipated, solution to this problem is slightly more complex than in the case described in Section 3.1.3, since flapping dynamics equations for each blade need now to be integrated simultaneously. Integration of Equation 3.2 can be efficiently performed using one of the many ODE solvers provided by Matlab.

### 3.3 Trim algorithm

The process of trimming a simulation model consists in the search for the set of system states and inputs which, given a certain flight condition, assure that the aircraft is in equilibrium, thus setting the model to a non-accelerated state. Finding the model trim condition can be useful for several purposes, such as evaluating aircraft performance and handling qualities, or starting the simulation from different flight conditions.

From a practical point of view, trimming an aircraft corresponds to solving its associated equations of motion; the algorithm implemented in the XV-15 model for this purpose is based on the Newton-Raphson method<sup>12</sup>, which can be used to solve any set of ordinary differential equations.

<sup>10</sup>As evaluating the structural damping is extremely difficult, it is a common practice to express this term as a function of other system parameters. In the present model,  $c_{struct}$  has been expressed as a function of the viscous equivalent critical damping ratio, following the formulation proposed in Reference [3]:

$$c_{struct} = 0.3 \cdot 2m \sqrt{\frac{k_\beta}{m}}$$

<sup>11</sup>See Appendix A.3 for further details

<sup>12</sup>Reference [5]

Assuming the dynamic problem to be well-posed, the aircraft equations of motion can be expressed in the standard form:

$$\begin{cases} \dot{\mathbf{x}} = f(\mathbf{x}, \mathbf{u}) \\ \mathbf{y} = g(\mathbf{x}, \mathbf{u}) \end{cases} \quad (3.8)$$

where  $\mathbf{u}$ ,  $\mathbf{x}$  and  $\mathbf{y}$  represent the system input, state and output vectors, respectively. In the case of the tilt-rotor model, typical examples of such vectors could be:

$$\begin{aligned} \mathbf{u} &= \{\vartheta_{0COLL}, X_{LN}, X_{LT}, X_{PD}, i_N, \Omega_{RPM}\}^T \\ \mathbf{x} &= \{x, y, h, u, v, w, p, q, r, \varphi, \vartheta, \psi, a_{1R}, b_{1R}, a_{1L}, b_{1L}\}^T \\ \dot{\mathbf{x}} &= \{\dot{x}, \dot{y}, \dot{h}, \dot{u}, \dot{v}, \dot{w}, \dot{p}, \dot{q}, \dot{r}, \dot{\varphi}, \dot{\vartheta}, \dot{\psi}, \dot{a}_{1R}, \dot{b}_{1R}, \dot{a}_{1L}, \dot{b}_{1L}\}^T \\ \mathbf{y} &= \{\gamma, V_{TAS}, \alpha, \beta, N_Y, N_Z\}^T \end{aligned} \quad (3.9)$$

Designating with the subscript 0 the values related to a steady-state (i.e. trim) condition, and linearising Equation 3.8 around this condition, it is possible to write:

$$\begin{cases} \dot{\mathbf{x}} - \dot{\mathbf{x}}_0 \\ \mathbf{y} - \mathbf{y}_0 \end{cases} = \begin{bmatrix} \mathbf{A} & \mathbf{B} \\ \mathbf{C} & \mathbf{D} \end{bmatrix} \begin{cases} \mathbf{x} - \mathbf{x}_0 \\ \mathbf{u} - \mathbf{u}_0 \end{cases} \quad (3.10)$$

Equation 3.10 provides a starting point from which the trim condition ( $\mathbf{x}_0, \mathbf{u}_0$ ) can be computed.

Given a certain trim condition, some of the quantities in Equation 3.9 are known<sup>13</sup>; therefore, it is possible to "freeze" their values. Freezing an element means setting a constraint on the problem – in particular:

- freezing a component of the state derivative or of the output vector to a certain value implies that the corresponding equation will be considered for the solution of the problem;
- freezing an element in the state or in the input vector means that such element will not be considered for the solution of the problem.

The remaining, "floated" (i.e. not frozen) quantities constitute the unknowns of the problem.

In order for a solution to be achievable, the number of unknowns should always be smaller or equal to that of constraints. Moreover, selection of "floated" and "frozen" parameters must be made with great care, as a wrong choice could lead to the removal of equations that are indeed needed for the solution of the problem, or to meaningless results due to constraints being placed on the wrong variables. Another vital aspect is the initialization of the various unknown values: since the Newton-Raphson algorithm performs a linear search, initial values far away from the searched solution may prevent the method from reaching convergence.

Once all constraints and target values have been identified, and initial guesses for  $\mathbf{u}_0$  and  $\mathbf{x}_0$  have been made, Equation 3.10 can be rewritten selecting only the rows of the matrix corresponding to the "frozen" outputs / state derivatives, and the columns corresponding to the "floated" inputs / states:

$$\begin{cases} \dot{\mathbf{x}}_{\text{FR}} - \dot{\mathbf{x}}_{0\text{FR}} \\ \mathbf{y}_{\text{FR}} - \mathbf{y}_{0\text{FR}} \end{cases} = \begin{bmatrix} \mathbf{A}_{\text{FR\&FL}} & \mathbf{B}_{\text{FR\&FL}} \\ \mathbf{C}_{\text{FR\&FL}} & \mathbf{D}_{\text{FR\&FL}} \end{bmatrix} \begin{cases} \mathbf{x}_{\text{FL}} - \mathbf{x}_{0\text{FL}} \\ \mathbf{u}_{\text{FL}} - \mathbf{u}_{0\text{FL}} \end{cases}$$

<sup>13</sup>For instance, if straight level flight at a given altitude is considered, the value of  $h$  will be obviously known; likewise, it is quite evident that, for example,  $q$ ,  $\gamma$  and  $\dot{w}$  will be all identically null. On the other hand,  $\alpha$ ,  $\vartheta$  and  $\dot{x}$  will probably be unknown. The same reasoning can be applied to all components of the vectors in Equation 3.9.

Which yields:

$$\begin{aligned} \begin{Bmatrix} \mathbf{x}_{\text{FL}} \\ \mathbf{u}_{\text{FL}} \end{Bmatrix} &= \begin{Bmatrix} \mathbf{x}_{0\text{FL}} \\ \mathbf{u}_{0\text{FL}} \end{Bmatrix} + \begin{bmatrix} \mathbf{A}_{\text{FR\&FL}} & \mathbf{B}_{\text{FR\&FL}} \\ \mathbf{C}_{\text{FR\&FL}} & \mathbf{D}_{\text{FR\&FL}} \end{bmatrix}^{-1} \begin{Bmatrix} \dot{\mathbf{x}}_{\text{FR}} - \dot{\mathbf{x}}_{0\text{FR}} \\ \mathbf{y}_{\text{FR}} - \mathbf{y}_{0\text{FR}} \end{Bmatrix} = \\ &= \begin{Bmatrix} \mathbf{x}_{0\text{FL}} \\ \mathbf{u}_{0\text{FL}} \end{Bmatrix} + \begin{bmatrix} \mathbf{A}_{\text{FR\&FL}} & \mathbf{B}_{\text{FR\&FL}} \\ \mathbf{C}_{\text{FR\&FL}} & \mathbf{D}_{\text{FR\&FL}} \end{bmatrix}^{-1} \begin{Bmatrix} \dot{\mathbf{x}}_{\text{FR}} - f_{\text{FR}}(\mathbf{x}_0, \mathbf{u}_0) \\ \mathbf{y}_{\text{FR}} - g_{\text{FR}}(\mathbf{x}_0, \mathbf{u}_0) \end{Bmatrix} \end{aligned} \quad (3.11)$$

Results of Equation 3.11 are subsequently combined with the remaining frozen input and state variables to form the estimated input and state vectors  $\mathbf{u}_e$  and  $\mathbf{x}_e$ . It is now possible to compute the error  $e$  between the approximation just obtained and the expected solution:

$$e = \left\| \begin{Bmatrix} \dot{\mathbf{x}}_{\text{FR}} - f_{\text{FR}}(\mathbf{x}_e, \mathbf{u}_e) \\ \mathbf{y}_{\text{FR}} - g_{\text{FR}}(\mathbf{x}_e, \mathbf{u}_e) \end{Bmatrix} \right\|$$

The whole procedure is repeated until the evaluated error falls within a specified tolerance. The values for  $\mathbf{u}_0$  and  $\mathbf{x}_0$  are updated at each iteration, using the estimated solutions from the previous step:

$$\begin{aligned} \mathbf{u}_0^{(j)} &= \mathbf{u}_e^{(j-1)} \\ \mathbf{x}_0^{(j)} &= \mathbf{x}_e^{(j-1)} \end{aligned}$$



## Chapter 4

# Implementation of the Simulink model

Following the update and correction activities carried out by the author, all changes to the mathematical model had to be implemented into the XV-15 simulation model. In addition to extensive debugging and "cleaning" of the existing code, major modifications were made to improve the treatment of blade aerodynamics and to include the gimbal into the flapping dynamics formulation. In addition, a new approach was adopted to replicate and adapt the isolated rotor model for representation of the two counter-rotating rotors.

### 4.1 Overview

The XV-15 model has been built in the Matlab/Simulink environment and is integrated with the ReDSim flight simulator of the ZAV Centre for Aviation at ZHAW. To comply with real-time requirements, the simulation is time-discrete with fixed time step duration.

A schematic representation of the complete aircraft model<sup>1</sup> is provided in Figure 4.1. Controls from the pilot interface and from the actuation system model are mixed in the *Mixer* block and sent as inputs to the A/C model; a dedicated subsystem called *Weight & Balance* then computes any displacements from the initial condition of the aircraft moments of inertia and center of gravity position. Four blocks evaluate the forces and moments produced by all the major components of the aircraft:

- In the *Gravity* block, intensity and direction of the gravity force acting on the aircraft are determined.
- The *Rotors* block contains the left and right rotor models, together with a subsystem in which rotor wake induced velocities are computed.
- The *Aerodynamics* subsystem provides the aerodynamic forces and moments generated by the aircraft fuselage, wing-pylon assembly, vertical and horizontal stabilizers.
- The *Landing Gear* block evaluates the loads produced by the landing gear.

All forces and moments are then summed in a dedicated subsystem and fed to the *Equations of Motion* block, in which aircraft position, attitude and motion are computed. An additional subsystem called *Environment* contains all equations related to the atmosphere and evaluates the atmospheric conditions, as well as the Mach number, according to the

---

<sup>1</sup>For a detailed description, see Reference [2]

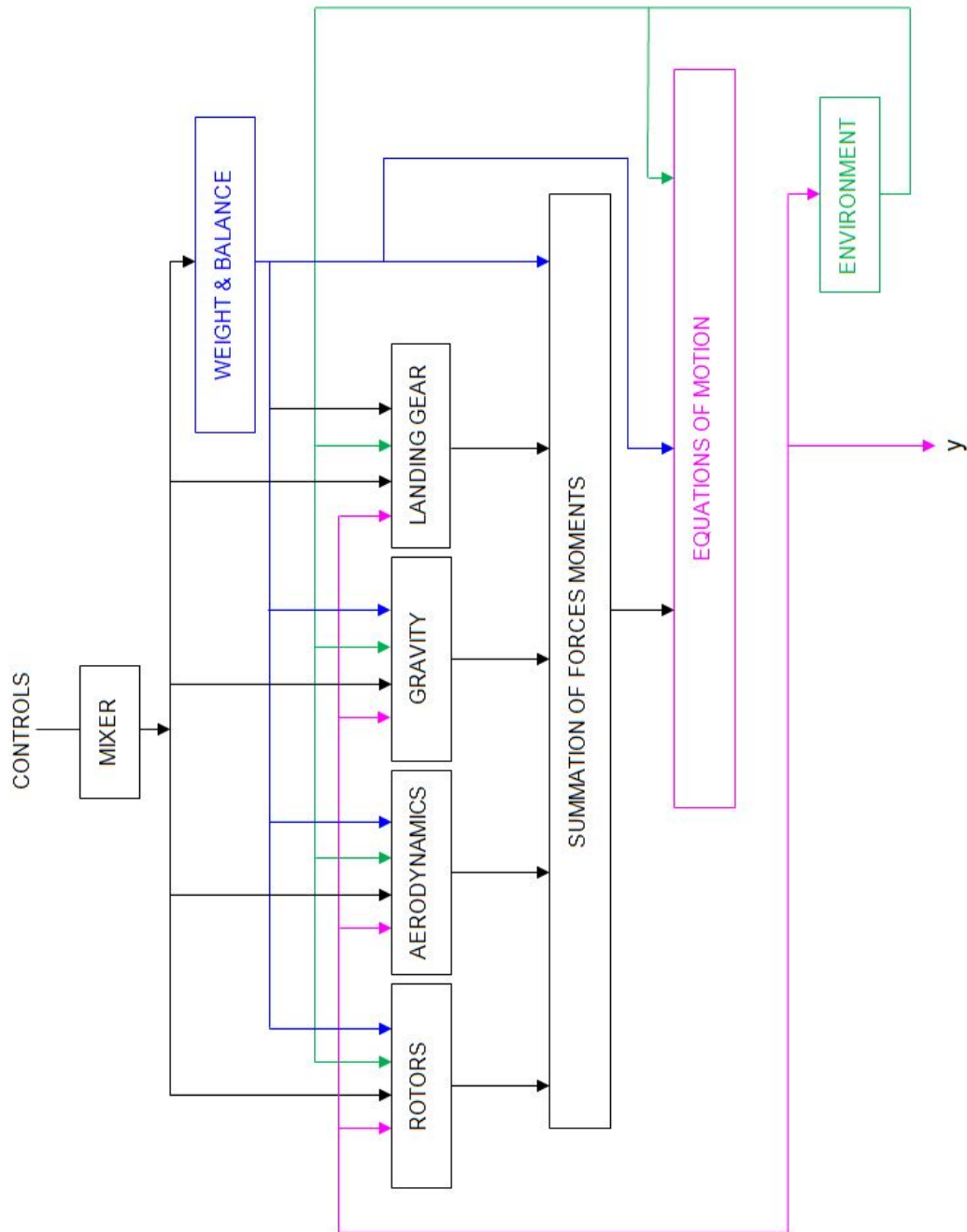


**Figure 4.1:** Block diagram representing the architecture of the complete XV-15 aircraft model

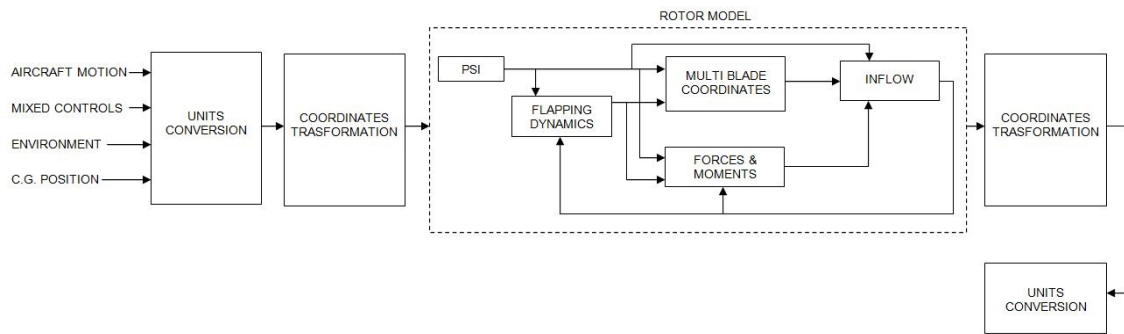


**Figure 4.2:** Architecture of the rotor Simulink model

motion of the aircraft. Finally, outputs from the *Equations of Motion* and *Environment* block are fed back to all the other subsystems.

## 4.2 Rotor model architecture

Since the XV-15 was equipped with two counter-rotating propellers, two separate rotor models are implemented within the aircraft Simulink model – one for the left and one for the right rotor. Both share the same architecture, which is represented in Figure 4.2.

The following inputs are fed to the rotor model from other subsystems in the aircraft model:

- the aircraft linear and rotational speeds and accelerations, in body axes;
- environment data such as speed of sound, air density and the gravity acceleration vector (the latter again in body axes);
- center of gravity position (from the *Weight & Balance* subsystem);
- controls.

While the aircraft model is entirely based on the U.S. customary system of units, the rotor model has been developed using units from the International System; therefore, units of measurement of the various inputs are converted in a dedicated block to comply with the rotor model requirements. In addition, all vectors are projected from the main aircraft body axes to the rotor Hub reference frame.

The actual rotor model is composed of five blocks; its workflow can be summarized as follows:

1. The *Psi* subsystem computes the blade azimuth angle  $\psi$  for each blade as a function of simulation time and the rotor rotational speed; blade tip speed  $V_{\text{tip}}$  is also evaluated. These outputs are then used in all the other model blocks.
2. In the *Flapping Dynamics* block, the flapping dynamics differential equation is solved to compute, for each blade, the flapping angle  $\beta$  and its derivatives  $\dot{\beta}$  and  $\ddot{\beta}$ .
3. Output from *Flapping Dynamics* is fed to two subsystems:
  - the *Multi Blade Coordinates* block, in which the multi-blade coordinates transformation is operated to determine the orientation of the rotor tip-path-plane;

- the *Forces and Moments* subsystem, in which rotor hub loads (in the Hub reference frame), thrust and required torque are computed.
4. The results obtained in the previous two blocks constitute the inputs of the *Inflow* subsystem, where rotor inflow velocity is determined by integrating the inflow dynamics equation.
  5. The components of the inflow velocity thus obtained are fed back to the *Flapping Dynamics* and *Forces and Moments* (where they are needed to compute the angle of attack of each blade section).

Rotor forces and moments, along with the inflow velocities, constitute the main output of the rotor model. To make them suitable for use in other subsystems of the aircraft model, all these outputs are again referred to the main aircraft body axes, and their units of measurement are converted into the U.S. customary system.

Thanks to the choice of reference frames described in Section 3.1.1, all the equations implemented in the rotor model are valid for both the right and left rotor, independently from the direction in which such rotors rotate. This characteristic has represented a huge advantage, as it has allowed to use the exact same library block (by literally copying and pasting it) for both rotors – thus ensuring that the rotors are perfectly simmetrical, in addition to greatly speeding up the whole implementation process, reducing model complexity and (not less importantly) minimizing the chances of involuntary mistakes.

Differences between the two rotor models are found only when conversion of inputs and outputs is performed between the aircraft body axes system and the Hub reference frame. In fact, since specular frames of reference are used for the left and right side of the vehicle, a few minor changes had to be made in the **left** rotor model to adapt to the different sign conventions; in particular:

- Since the aircraft body axis  $y_B$  is positive to the right of the vehicle while the  $y_h$  axis in the Hub system is positive to the left, all the linear speed and acceleration components and all the forces along  $y_B$  have been multiplied by -1.
- Moreover, as left-handed coordinates are adopted in the rotor model, all rotational speeds and accelerations, as well as all the moments, around the body axes  $x_B$  and  $z_B$  have been again multiplied by -1.
- Finally, the sign of the lateral cyclic input ( $A_1$ ) has also been inverted; this way, when a lateral input is given to the aircraft model, the forces along  $y_b$  generated by the two rotors are both oriented towards the same direction.

### 4.3 Blade aerodynamics

The method described in Section 3.1.2 for the evaluation of rotor aerodynamic loads by means of the Blade Element Theory has been implemented by dividing each blade into 20 sections of equal length. Chord length and blade twist angle are computed for each section as functions of the radial position, using polynomial laws; therefore, geometry variations along the blade can be easily taken into account. Ninth-degree polynomials are employed to evaluate tip-loss and flow compressibility correction factors.

Once the angle of attack is known, the lift and drag coefficients and their derivatives are determined for each section through linear interpolation of the aerodynamic data contained in the model initialization file (`iniac.m`). To reduce complexity, a NACA 64-208 airfoil

has been adopted for the whole length of each blade<sup>2</sup>; however, the model can be easily modified to take into account variations in airfoil geometry.

Aerodynamic loads are symbolically integrated along the blade span using the method of the trapezoids<sup>3</sup>; therefore, no numerical integration is needed during the simulation, and mere algebraic calculations performed at each time step.

### 4.3.1 Airfoil aerodynamic coefficients

As the blades of a tilt-rotor aircraft proprotors operate at a wide range of angles of attack, the complete airfoil polar curves (i.e. for angles of attack spanning from -180 to +180 degrees) need to be included in the model initialization file. Available data for the NACA 64-208 airfoil covered only a limited range of angles of attack; therefore, the missing parts of the polar curves have been reconstructed using the empirical approach described hereafter.

1. The airfoil lift and drag coefficients can be expressed as a function of the angle of attack using the approximation proposed by Hoerner (Reference [13]):

$$\begin{aligned} C_l &= k_{Cl} \sin \alpha \cos \alpha \\ C_d &= k_{Cd} \sin^2 \alpha \end{aligned} \tag{4.1}$$

An attempt value is assigned to the coefficients  $k_{Cl}$  and  $k_{Cd}$ .

2. The missing portions of the polar curves are determined using Equation 4.1, and introducing corrections in order to best fit the available aerodynamic data.
3. The derivatives of the aerodynamic coefficients with respect to the angle of attack ( $C_{l\alpha}$  and  $C_{d\alpha}$ ) are computed using the centered difference method:

$$f'(x_j) \approx \frac{f(x_{j+1}) - f(x_{j-1}))}{x_{j+1} - x_{j-1}}$$

4. The aerodynamic coefficients thus obtained are initialized within the isolated rotor model. A series of simulations is run to evaluate rotor performance in hovering conditions, for different values of the collective pitch  $\vartheta_0$ .
5. Results of these simulation are compared with experimental data from wind-tunnel tests of the XV-15 rotor provided by Franklin D. Harris in Reference [11].
6. All the previous steps are repeated, each time changing the combination of attempt values assigned to  $k_{Cl}$  and  $k_{Cd}$  in Equation 4.1.
7. The definitive values for  $k_{Cl}$  and  $k_{Cd}$  are selected by choosing the combination providing the best match between the simulated performance and the reference experimental data.

The process described above yielded the following results:

$$\begin{aligned} k_{Cl} &= 1.9 \\ k_{Cd} &= 1.2 \end{aligned}$$

---

<sup>2</sup>This is indeed an approximation, as in the actual XV-15 proprotors a NACA 64-935 airfoil was used for the blade root section (Reference [11]).

<sup>3</sup>For further details, see Appendix A.2.2 and Reference [9].

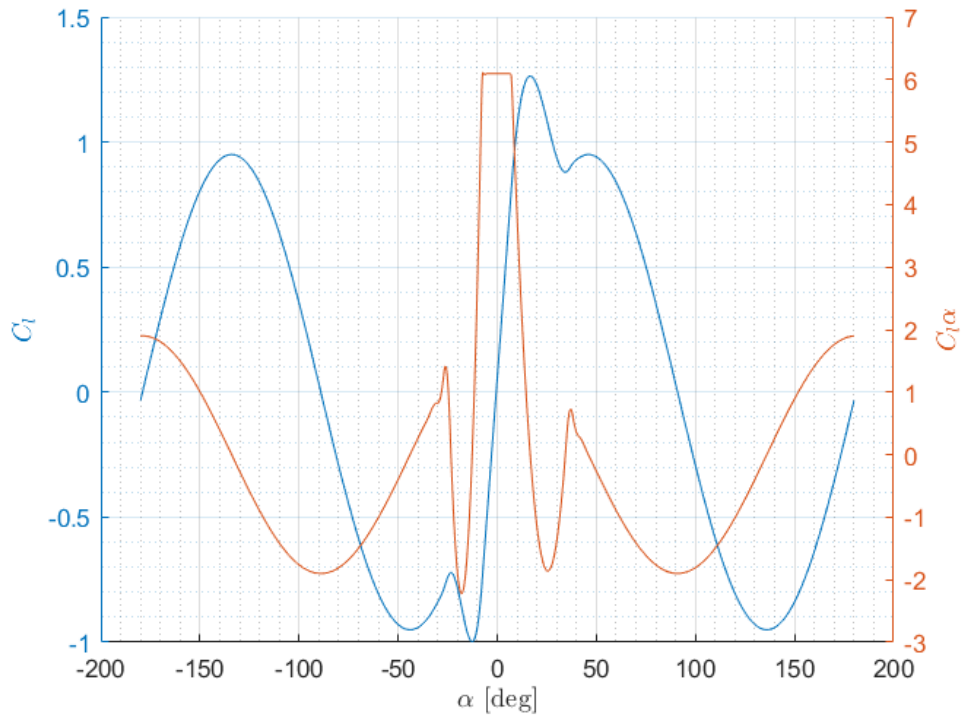


**Figure 4.3:** Complete  $C_l - \alpha$  and  $C_{l\alpha} - \alpha$  curves for the NACA 64-208 airfoil

The complete lift and drag polar curves obtained using these values, along with their derivatives, constitute the data implemented in `iniac.m` and are reported in Figures 4.3 and 4.4. A comparison between simulation results based on these data and the wind-tunnel test data from Reference [11] is provided in Figure 4.5 to 4.7.

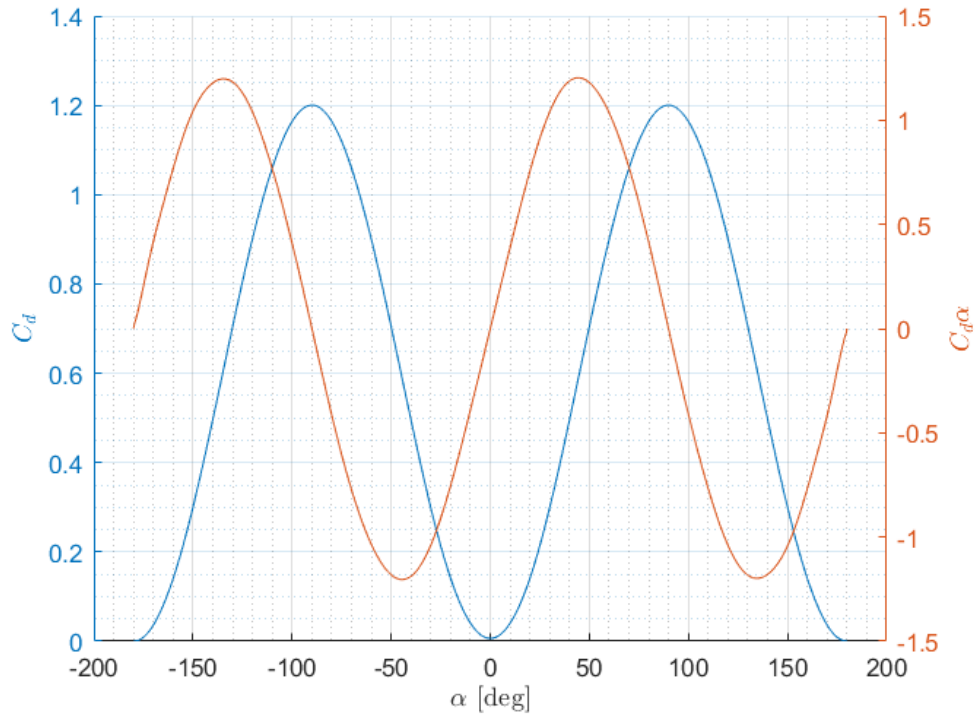


**Figure 4.4:** Complete  $C_d - \alpha$  and  $C_{d\alpha} - \alpha$  curves for the NACA 64-208 airfoil

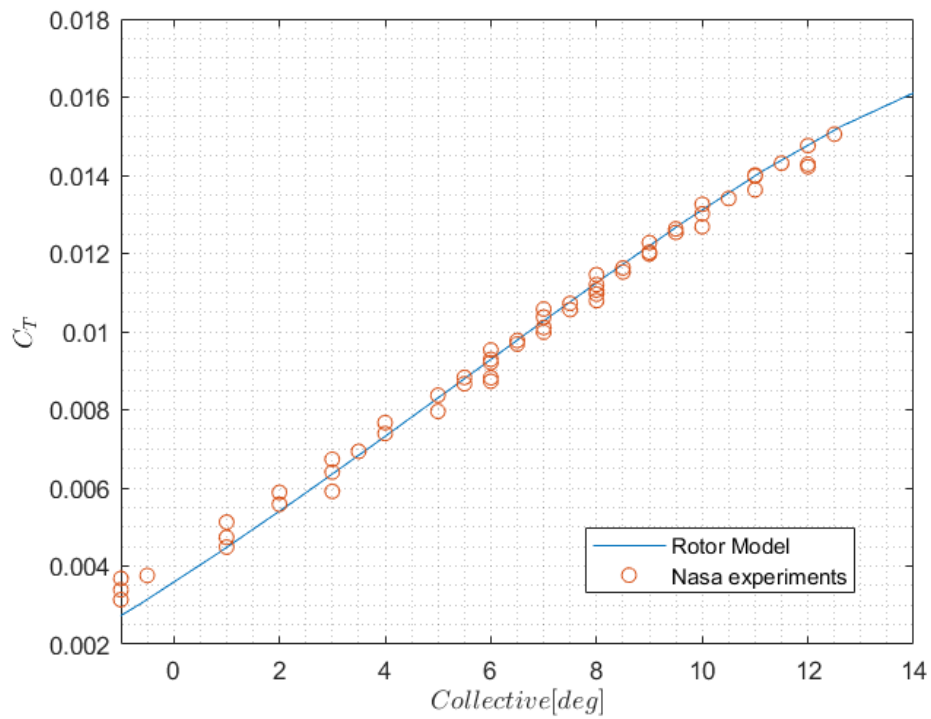


**Figure 4.5:** Rotor hover performance – Variation of the thrust coefficient with the collective pitch

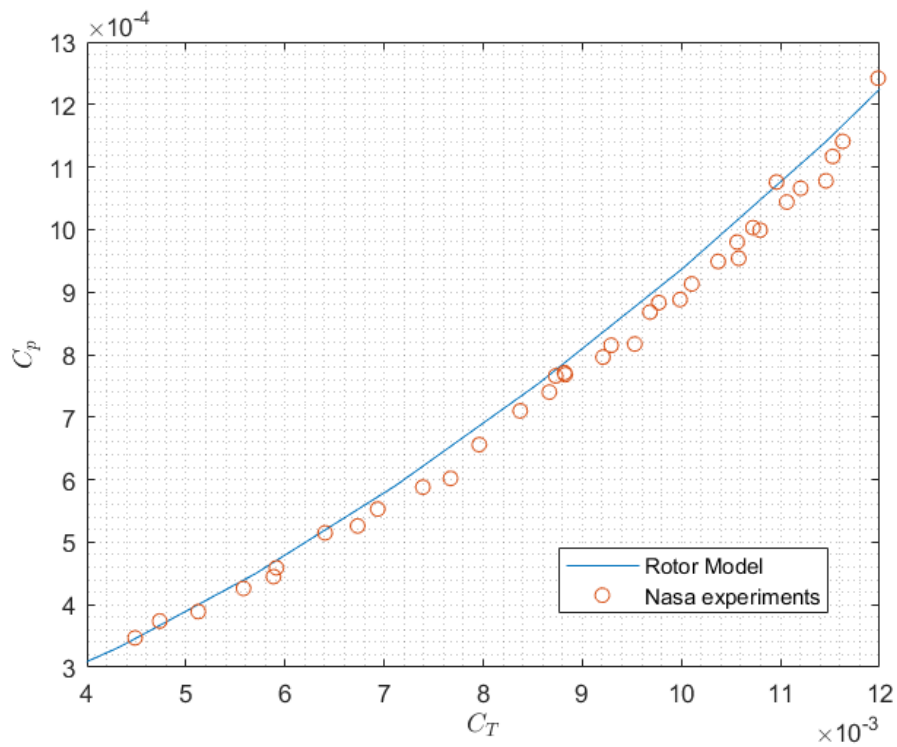


**Figure 4.6:** Rotor hover performance – Torque coefficient versus thrust coefficient

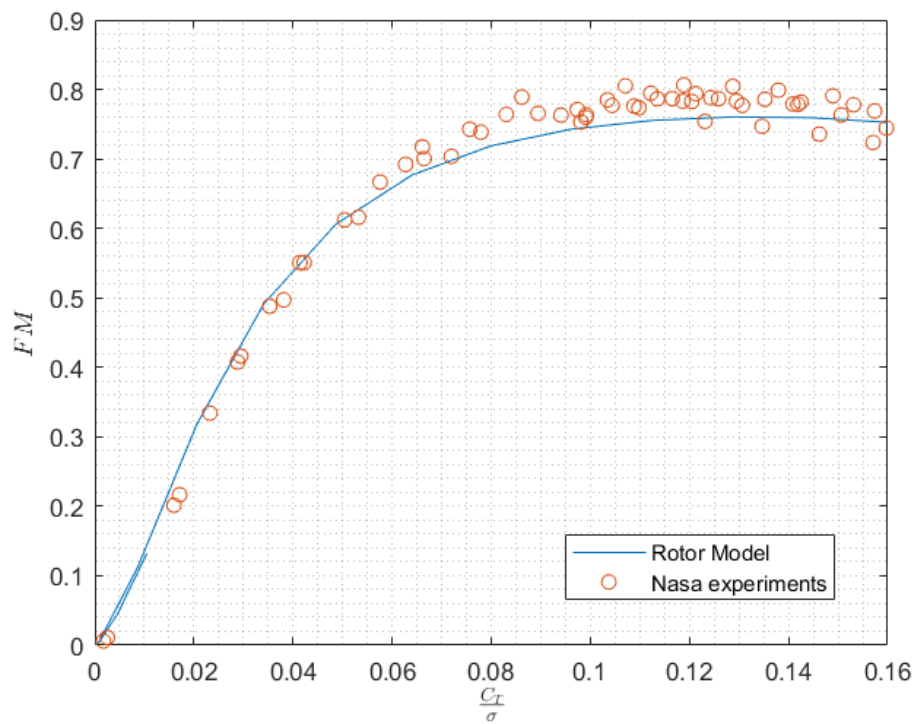


**Figure 4.7:** Rotor hover performance – Thrust-to-solidity ratio versus Figure of Merit ( $FM = \sqrt{C_T^3/2}/C_P$ )

## 4.4 Integration of differential equations

### 4.4.1 Flapping dynamics

The rotor model is meant for a fixed-step, time-discrete simulation: therefore, all differential equations within the model must be integrated using discrete-time-step solvers.

In general, two parameters affect the accuracy of the solution of a given system. One is the sampling time of the simulation, which in the case at hand is limited in terms of minimum duration due to real-time simulation requirements, and has been set at 1/400 seconds. The other factor is the method implemented within the solver; the latter must be selected with great care, keeping in mind that:

- Higher-order methods afford better accuracy and stability, but on the other hand require the solution of a higher number of mathematical operations at each time step, thus increasing computational cost.
- Lower-order methods, conversely, are less computationally expensive but are also less precise, and, depending on the time constant of the system at issue, could require too short sampling times to avoid insurgence of numerical instability problems.

The situation described in this second point actually occurred when the model was modified to introduce the formulation of the gimballed rotor flapping dynamics described in Section ???. Previously to that, the second-order Tustin solver implemented in the *Flapping Dynamics* subsystem had been sufficient to provide adequate accuracy in the solution of the flapping dynamics equation<sup>4</sup>. On the contrary, following the introduction of the gimbal model, this method manifested a numerical instability which resulted in simulation divergence and disappeared for sampling times inferior to 1/5000 seconds. Such a short time-step being incompatible with a real-time simulation, the Tustin solver has been replaced with a fourth order Runge-Kutta solver:

$$y_{n+1} = y_n + \frac{1}{6}(k_1 + 2k_2 + 2k_3 + k_4)$$

with:

$$\begin{aligned} k_1 &= hf(t_n, y_n) \\ k_2 &= hf\left(t_n + \frac{h}{2}, y_n + \frac{k_1}{2}\right) \\ k_3 &= hf\left(t_n + \frac{h}{2}, y_n + \frac{k_2}{2}\right) \\ k_4 &= hf(t_n + h, y_n + k_3) \end{aligned}$$

where  $h$  corresponds to the simulation sampling time  $T_s$ . The new method is numerically stable for  $T_s$  up to 1/100 seconds and provides sufficiently accurate solutions at the current sampling time of 1/400 seconds.

The reason behind the instability of the Tustin method can be understood through the following simplified reasoning. Recalling Equation 3.2 on page 29, the flapping blade can be considered as a typical second-order dynamic system:

$$m\ddot{\beta} + c\dot{\beta} + k\beta = F_\beta$$

---

<sup>4</sup>See Reference [9] for further details

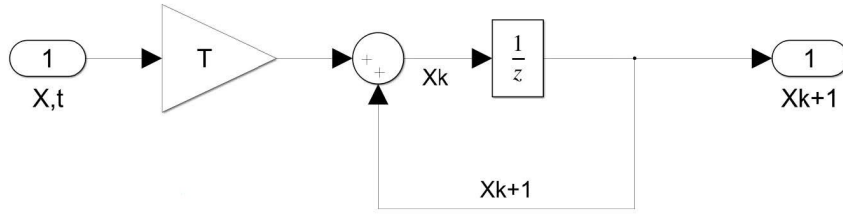


**Figure 4.8:** Implementation of the Forward Euler Method in the Simulink model

The time constant of such system is inversely proportional to its natural frequency, which in turn can be computed as:

$$\omega_n = \sqrt{\frac{k}{m}} \quad (4.2)$$

where for the system at hand  $m$  is equal to the blade moment of inertia.

In the previous rotor model, to account for the comparatively large flapping angles due to the presence of the gimbal, an assumption was made that the stiffness  $K_\beta$  of the flapping hinge was equal to that of the gimbal joint, i.e.  $K_\beta = k_G = 305.05 \text{ Nm deg}^{-1}$ . If contributions from inertial and aerodynamic loads to the system stiffness  $k$  are neglected, Equation 4.2 becomes:

$$\omega_n \approx \sqrt{\frac{K_\beta}{I_\beta}} = \sqrt{\frac{k_G}{I_\beta}} = 11.21 \text{ rad/s}$$

On the other hand, in the updated model the stiffness of both the gimbal joint and the hub coning spring ( $k_\beta = 244\,047.23 \text{ Nm deg}^{-1}$ ) is taken into account. From Equation 3.7 on page 35, considering each blade to be independent from the others and again neglecting all aerodynamic and inertial contributions:

$$k \approx \frac{1}{3}(2k_G + k_\beta) = 4.673 \times 10^6 \text{ Nm deg}^{-1}$$

which, substituted in Equation 4.2, yields:

$$\omega_n = \sqrt{\frac{k}{I_\beta}} \approx 183.4 \text{ rad/s}$$

As can be easily observed even from this much-simplified treatment, the natural frequency of the system in this second case is one degree of magnitude higher than that provided by the previous formulation – which means that the dynamic behaviour of the system varies much more rapidly than before, thus can be adequately described only by adopting a higher-order method or, alternatively, reducing the sampling time.

#### 4.4.2 Inflow dynamics

The inflow dynamics equation can be solved using a simple first-order method such as the Forward Euler Method:

$$y_{n+1} = y_n + h f(t_n, y_n)$$

where  $h$  corresponds again to the sampling time  $T_s$ . Implementation of this method in the Simulink model is shown in Figure 4.8.

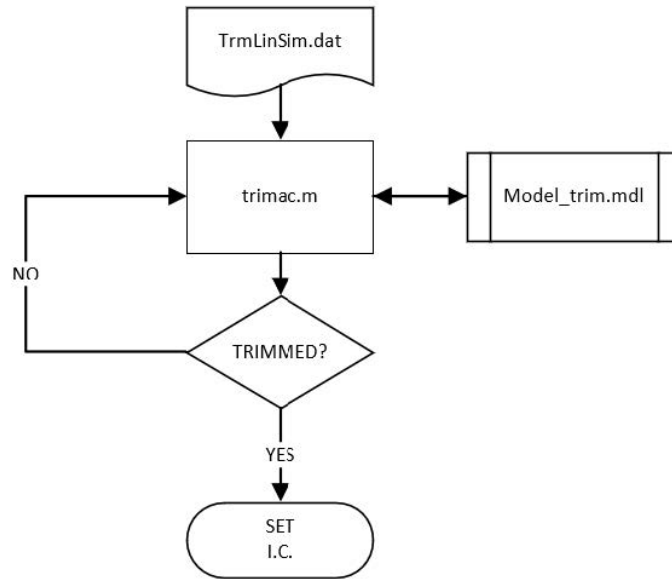


**Figure 4.9:** Flow chart of the process adopted to trim the model

## 4.5 Trimming the model

The trim of the XV-15 model is operated using a dedicated Matlab function (`trimac.m`) developed by Pierluigi Capone of ZHAW. The routine contained in this function is based on a rotorcraft trim strategy called "periodic shooting"<sup>5</sup>, in which the initial conditions and controls necessary for a trimmed solution are found by means of an integration through one rotor revolution (to obtain errors), followed by iteration of the Newton-Raphson algorithm described in Section 3.3.

The trim procedure is summarized in Figure 4.9. All trim parameters are set by editing the `TrmLinSim.dat` file, which is then read by `trimac.m`. At each iteration, simulation of one rotor revolution is performed in a dedicated Simulink model, `model_trim.mdl`, in which all the states and input signals of the aircraft model are set directly by the trim function. When convergence of the Newton-Raphson algorithm is achieved, all the parameters identifying the aircraft trim condition are printed on-screen.

---

<sup>5</sup>Reference [17]



## Chapter 5

# Validation and results

The validation process has the aim of assessing the accuracy of a simulation, by comparing its results against reference data. To this purpose, all the elements of which the simulation is composed, from the hardware and software environment to the mathematical model, from cockpit and controls to visual, motion and aural systems, play an equally important role and should be taken into account.

In the present case, the validation effort was focused specifically on the mathematical model, and was aimed essentially at verifying and quantifying the effects of all the modifications introduced by the author and described in the previous chapters. This goal has been pursued by means of two different activities:

1. On one hand, outputs from off-line simulations have been compared with existing XV-15 data.
2. On the other hand, a series of pilot-in-the-loop tests has been carried out, to evaluate the pilots' perception of the aircraft model and assess the fidelity of the simulation to a real piloting experience.

### 5.1 Comparison of trim results

Ideally, the validation of the off-line simulation outputs would have required that data from the XV-15 flight tests be used as a benchmark. Unfortunately, such data are mostly not in the public domain, or are reported in literature in the form of diagrams from which it is hard to extract any precise values. On the other hand, a vast amount of data has been published by NASA regarding the performance of the Generic Tilt-Rotor Simulation (GTRS) developed by Bell and NASA to support the XV-15 tilt-rotor research project. These data can be considered as a good basis of comparison for the model at hand, as the GTRS was extensively validated and corrected over the years, to make it closely match the data gathered from XV-15 flight tests.<sup>1</sup>

In particular, Reference [8] reports the results of the computation of trim conditions for a wide variety of flight conditions, spanning from hover to conversion and high-speed forward flight, with different values of airspeed, nacelle angle, rotor speed, flap setting and altitude. An example of a page containing these results can be seen in Figure 5.1. Such results have been compared by the author with those obtained by trimming the model object of this work, in the same flight conditions, using the trim routine described in Section 4.5.

---

<sup>1</sup>As described in detail in report CR-166537, Reference [8]

```

***** AIRCRAFT TRIM FLIGHT CONDITIONS *****
*****
*** VT = 60.00 KTS *** NACELLE INCIDENCE = 75.0 DEG *** CONVERSION ***
*** GW = 13000.0 RPM = 589.00 SLCG = 299.86 WLCG = 80.80 ***
*** MAST ANGLE = 15.00 DEG ***** FLAP SETTING = 40/25 DEG ***
*****

----- EARTH REFERENCE -----
RATE (FPS) 101.3 UE VE WE
ACCEL (FPS2) 0.4322E-04 0.0000E+00 -.9537E-06
0.2496E-06 -.1529E-03

----- BODY REFERENCE -----
RATE (FT OR DEG/SEC) 100.8 UB VB WB P Q R
ACCEL(FT OR DEG/SEC2) 0.1009E-06 9.852 0.0000E+00 0.0000E+00 0.0000E+00
0.0000E+00 0.1217E-02 -.1830E-05

----- ATMOSPHERIC CONDITIONS ----- FLIGHT PATH CONDITIONS ----- INERTIAS ----- CENTER OF GRAVITY -----
ALTITUDE (FT) 5000.00 CAL. AIRSPEED (KNOTS) 60.01 (SLUGS-FT2) (IN)
DENSITY ALT. (FT) 0.00 RATE OF DESCENT (FPS) 0.00
PRESSURE ALT. (FT) 0.00 G-LEVEL (G S) 1.00 IXX 0.5249E+05 S.L. 299.9
AMBIENT TEMP (DEG-R) 288.16 DYN PRES (SLUGS/FT-SEC2) 12.19 IXZ 1208. B.L. 0.0000E+00
OUTSIDE AIR TEMP (DEG-C) 15.00 ANGLE OF ATTACK (DEG) 5.583 IYY 0.2119E+05 W.L. 80.80
AIR DENSITY (SLUGS/FT3) 0.2377E-02 FLIGHT PATH ANGLE (DEG) 0.000 IZZ 0.6647E+05
THETES (ND) 1.00000 ROLL ANGLE (DEG) 0.000
DELSTD (ND) 1.00000 PITCH ANGLE (DEG) 5.583
SIGMA PRIME (ND) 1.00000 YAW ANGLE (DEG) 0.000

----- CONTROL DISPLACEMENTS ----- POWER/TORQUE ----- BLADE -----
COLL (UP) (+) (IN) (PER) POWER TORQUE GOV. PITCH TIP SPEED BLADE TIP MACH NO.
LONG (FWD) 4.5420 47.31 LEFT 506.5 4516. 1.212 869.2 0.7786
LAT (RT) 4.8000 50.00 RIGHT 506.5 4516. 1.212 869.2 0.7786
PEDAL (RT) 2.5000 50.00 ENGINE 554.6

----- SWASH PLATE ANGLE (DEG) ----- ROTOR -----
THETAO LEFT ROTOR RIGHT ROTOR AD LONG LAT THRUST H-FORCE Y-FORCE JET
B1 41.8044 41.8044 (DEG) (DEG) (DEG) (LBS) (LBS) (LBS) (LBS)
A1 -0.4739 -0.4739 LEFT 2.3643 1.3843 4.4837 5012.95 189.03 141.81 32.36
RIGHT 2.3643 1.3843 4.4837 5012.95 189.03 141.81 32.36

----- SURFACE POSITIONS -----
ELEVATOR -1.2215 LEFT 0.4050 0.1296 20.3212 0.0478 0.000521 0.007228 0.016194
AILERON 0.0000 RIGHT 0.4050 0.1296 20.3212 0.0478 0.000521 0.007228 0.016194
RUDDER 0.0000 CDRISE CTCL CDALPHA CDLIM CDMACH CDFACT
LEFT -0.01330 0.01174 0.01000 0.85000 0.35000 0.20000
RIGHT -0.01330 0.01174

TIME USED FOR THIS TRIM = 0.0180 MIN

```

Figure 5.1: Example of the trim results contained in Reference [8]

The flight conditions considered for the present analysis are summarised in Table 5.1. Such conditions represent a relevant portion of the flight envelope of the XV-15: helicopter mode has been investigated both in hover and for various advance ratios, and conversion at three different nacelle angles has been considered; airplane mode has been studied for airspeed up to 220 knots, as the trim algorithm could not reach convergence for higher speed. For all flight conditions an aircraft gross weight of 13 000 lb has been considered.

The comparison of trim results has been focused especially on the following parameters:

- Pilot controls, in particular the root collective pitch ( $\vartheta_0$ ) and the longitudinal cyclic (the longitudinal cyclic and pedals being always in neutral position for all the conditions examined);
- the Euler angles  $\varphi$ ,  $\vartheta$  and  $\psi$ ;
- the aircraft angle of attack ( $\alpha_a$ ), sideslip angle ( $\beta_a$ ) and flight path angle ( $\gamma$ );
- the velocity components along the aircraft body axes ( $u$ ,  $v$  and  $w$ ) and the aircraft roll, pitch and yaw rates ( $p$ ,  $q$  and  $r$ );
- the overall forces and moments generated by the two rotors ( $X_{rot}$ ,  $Y_{rot}$ ,  $Z_{rot}$ ,  $L_{rot}$ ,  $M_{rot}$  and  $N_{rot}$ , in body axes);
- the rotor multi-blade coordinates ( $\beta_0$ ,  $\beta_{1s}$  and  $\beta_{1c}$  – results are the same for both left and right rotor).

The complete results of the comparison are reported in form of diagrams in Appendix B.

Some of the parameters listed above, besides being aligned with the reference data, present the typical values characterising straight and level flight: in fact, the roll, yaw,

**Table 5.1:** Flight conditions considered for the comparison of trim results

Nacelle angle	Rotor rpm	Flap setting	Altitude	Airspeed [kts]
90°	589	40/25	Sea Level Standard	0.01, 20, 40, 60, 80, 100
75°	589	40/25	Sea Level Standard	40, 60, 80, 100, 120
60°	589	20/12.5	Sea Level Standard	80, 100, 120, 140
30°	589	20/12.5	Sea Level Standard	100, 120, 140, 160
0°	589	20/12.5	Sea Level Standard	120, 140, 160, 180
0°	589	0/0	Sea Level Standard	140, 160, 180, 200, 220
0°	517	0/0	Sea Level Standard	140, 160, 180, 200, 220
0°	517	0/0	12 000 ft Standard	140, 160, 180, 200, 220

sideslip and flight path angles, as well as the angular rates  $p$ ,  $q$  and  $r$  and the lateral velocity  $v$ , are either identically null or very close to zero, in all the conditions examined.

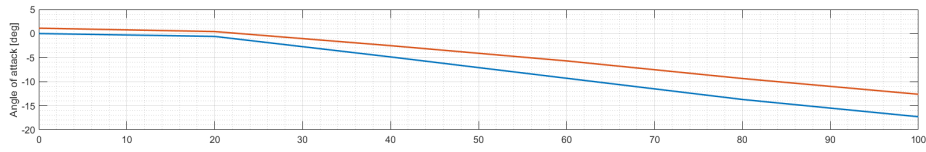
The value of the aircraft angle of attack computed by the present model is also generally close to what reported in Reference [8], as can be seen in Figure 5.2. The only exception is represented by the flight conditions in which flaps are set to 0/0: in this situation, a constant offset of about  $-7$  degrees is observed with respect to the reference data. The cause of such discrepancy could be an error within the aerodynamic model of the wing, or an incorrect initialization of the aerodynamic data.

As regards the values of pilot controls necessary to achieve the trim condition, the following observations can be made:

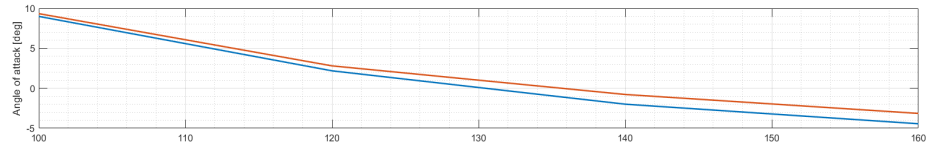
- The value of the root collective pitch shows good correspondence with the reference data at low speed and for high nacelle angle (90, 75 degrees). As speed increases and nacelle angle decreases, the computed value maintains the same trend as the one of reference data, but presents a more or less constant offset of  $+2$  degrees (Figure 5.3). To interpret this results, it must be taken into account that several doubts still exist concerning the actual range of the collective pitch allowed in the various flight modes, and particularly in airplane mode and at low nacelle angles; to this purpose, a deeper analysis of available literature on the subject shall be conducted.
- The longitudinal cyclic is in general aligned with the values reported in Reference [8], with an offset that is very narrow at lower speed and tends to increase for higher-speed flight conditions (Figure 5.4).

When comparing the rotor flapping parameters computed by the present model with those provided by the reference NASA simulator, it is important to keep in mind that these results come from two different rotor mathematical models. In fact, to comply with real-time simulation requirements, the rotor model implemented in the NASA GTRS simulator adopted a simplified treatment of rotor flapping dynamics<sup>2</sup>; the present model, on the other hand, has been modified to include a more detailed and realistic description of this dynamics. Results related to the rotor coning angle  $\beta_0$  (Figure 5.5) indicate that the value predicted by the present model is significantly lower than the reference one. A possible element which could contribute to this discrepancy is the fact that the value currently

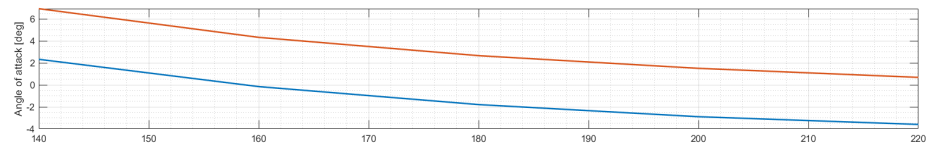
<sup>2</sup>Reference [7]



(a) Helicopter mode

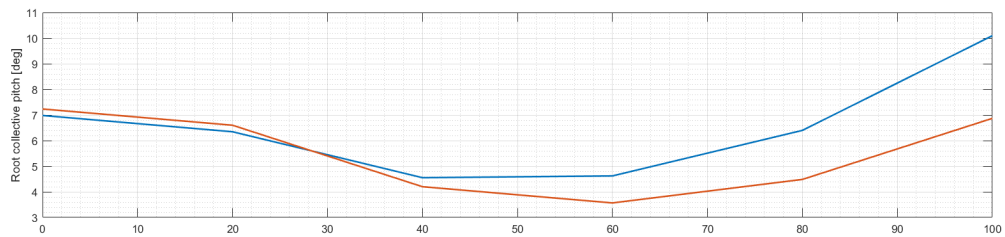


(b) Conversion,  $i_N = 30^\circ$

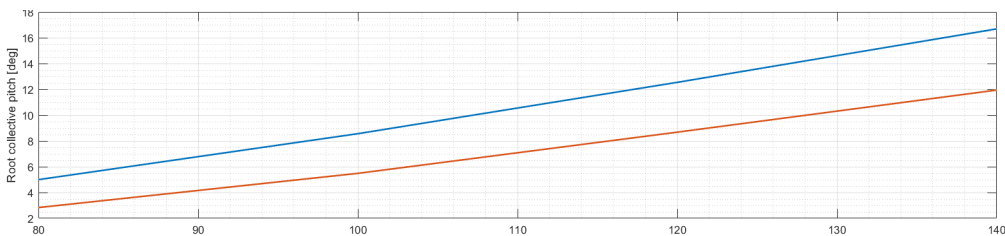


(c) Airplane mode, 517 rpm, flap setting: 0/0, Sea Level Standard

**Figure 5.2:** Comparison of trim results – Angle of attack

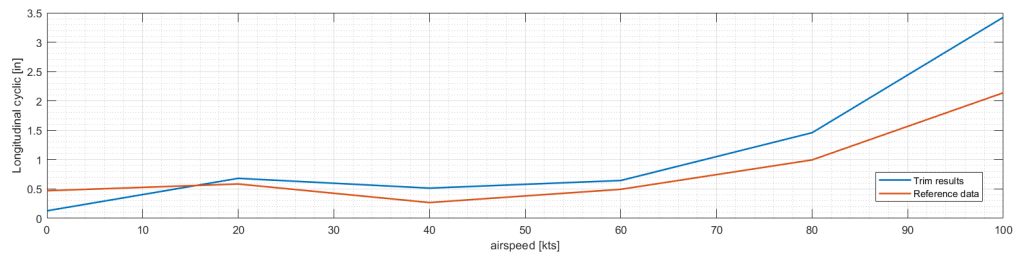


(a) Helicopter mode

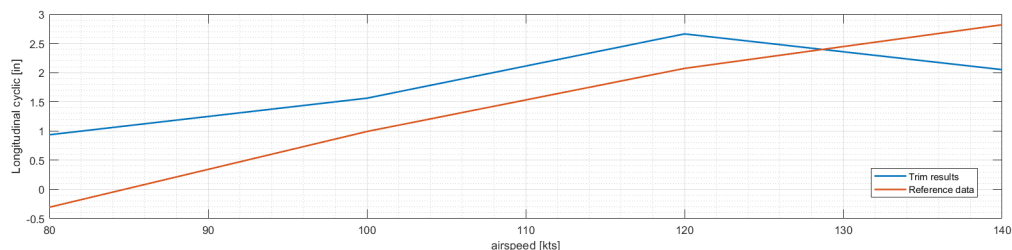
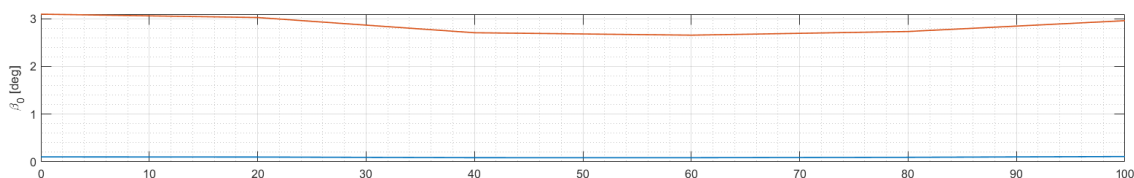


(b) Conversion,  $i_N = 60^\circ$

**Figure 5.3:** Comparison of trim results – Root collective pitch



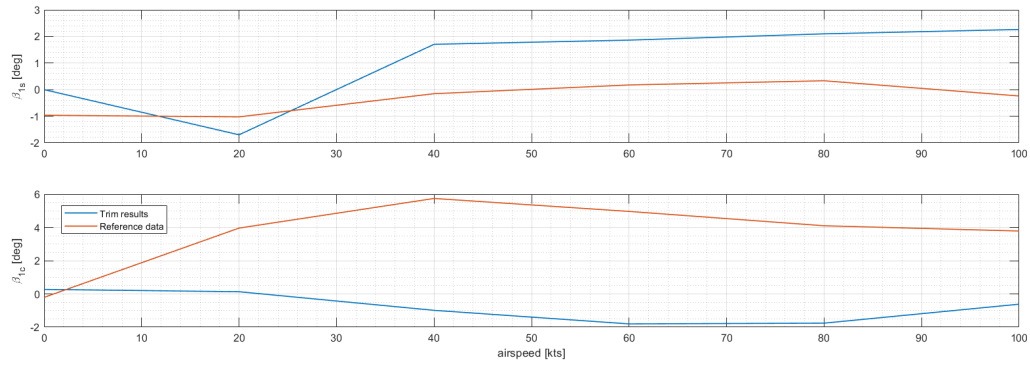
(a) Helicopter mode

(b) Conversion,  $i_N = 60^\circ$ **Figure 5.4:** Comparison of trim results – Longitudinal cyclic**Figure 5.5:** Comparison of trim results – Rotor coning angle (Helicopter mode)

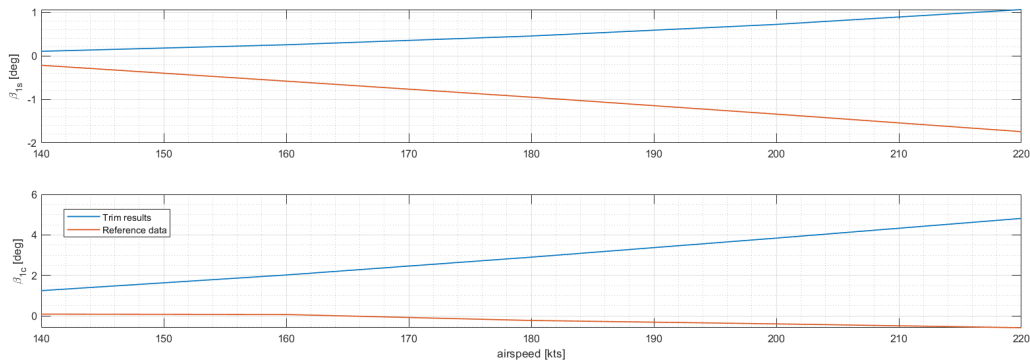
assigned to the hub stiffness  $k_\beta$ , extracted from Reference [7], might not correspond to the actual XV-15 value; a further review of available literature is necessary. Evident differences can also be observed, in any flight mode and at any speed (Figure 5.6), in the orientation of the rotor tip-path-plane as computed by the two models; an in-depth investigation shall be conducted to understand whether the reason for this incoherency resides in a mistake in the present formulation and implementation of rotor flapping dynamics, or in lack of accuracy in the reference model.

Finally, the analysis of the overall forces and moments generated by the rotors shows that the lateral force  $Y_{rot}$ , roll moment  $L_{rot}$  and yaw moment  $N_{rot}$  are always identically null, indicating that the two rotors are actually symmetric. Regarding instead the forces and moment in the longitudinal plane, their values are aligned with the reference data in helicopter mode and in general for high nacelle angles. In flight conditions characterised by higher speed and lower nacelle angle, on the other hand, such quantities display the same trends as in the reference NASA model, but differences with the reference values are more evident: in particular, rotor thrust (represented in airplane mode by the  $X$  force) is always significantly overestimated, as is the vertical force  $Z$ . A possible reason for this discrepancy could be the higher collective input computed by the present model at the same flight condition. The overall pitching moment is also overestimated with respect to reference data, as a natural consequence of the higher values of both the  $X$  and  $Z$  force.

To sum up the overall outcome of the present analysis, it is possible to affirm that the computation of trim conditions yields in general acceptable results for helicopter mode and for the initial phases of conversion. The representation of conditions typical of flight in



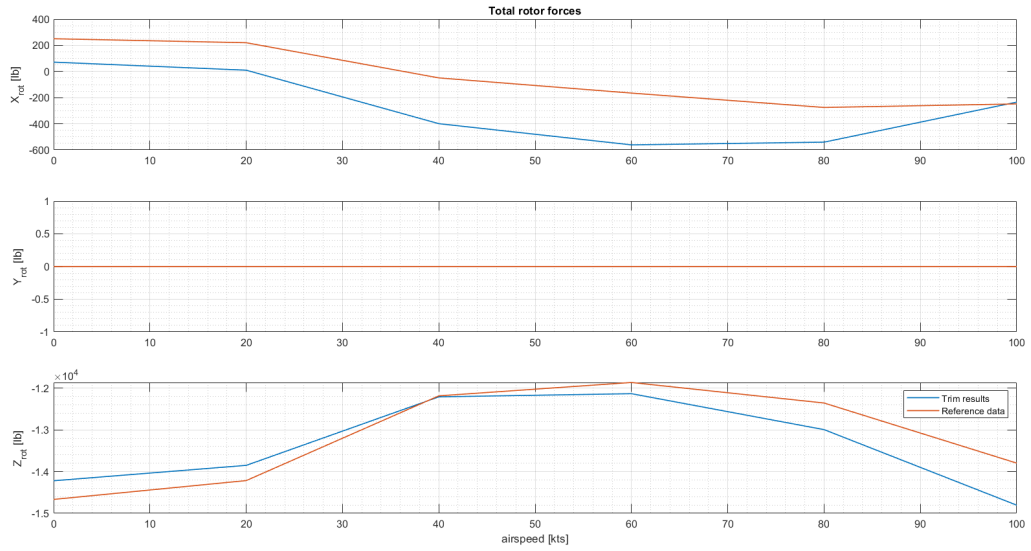
(a) Helicopter mode



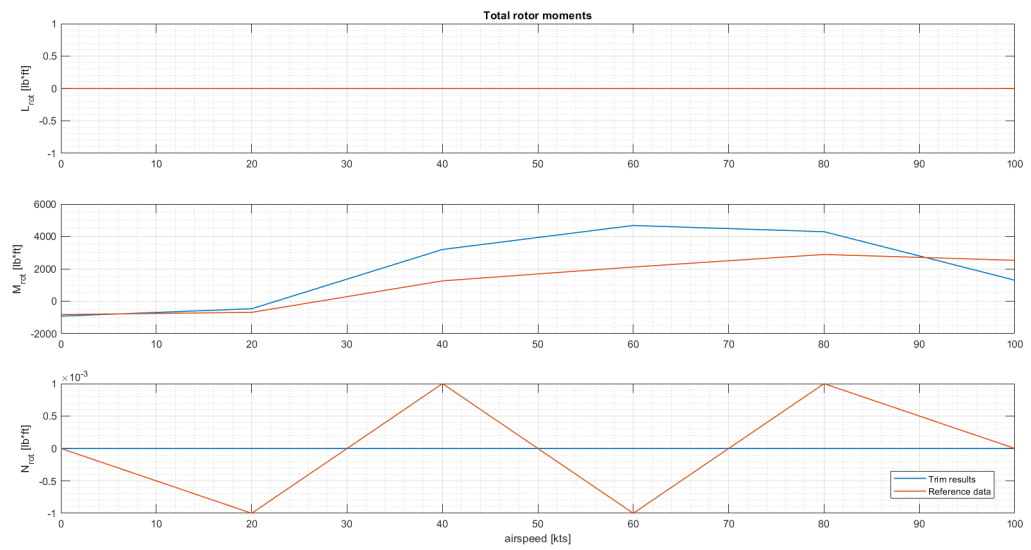
(b) Airplane mode, 517 rpm, flap setting: 0/0, Sea Level Standard

**Figure 5.6:** Comparison of trim results – Tip-path-plane orientation

airplane mode is instead rather distant from the one provided by the reference model. It has to be considered that the latter mode of flight has been investigated with less depth and accuracy during the development and implementation of the present rotor model, and that a few major features still need to be introduced within the overall aircraft model in order to obtain more realistic results.

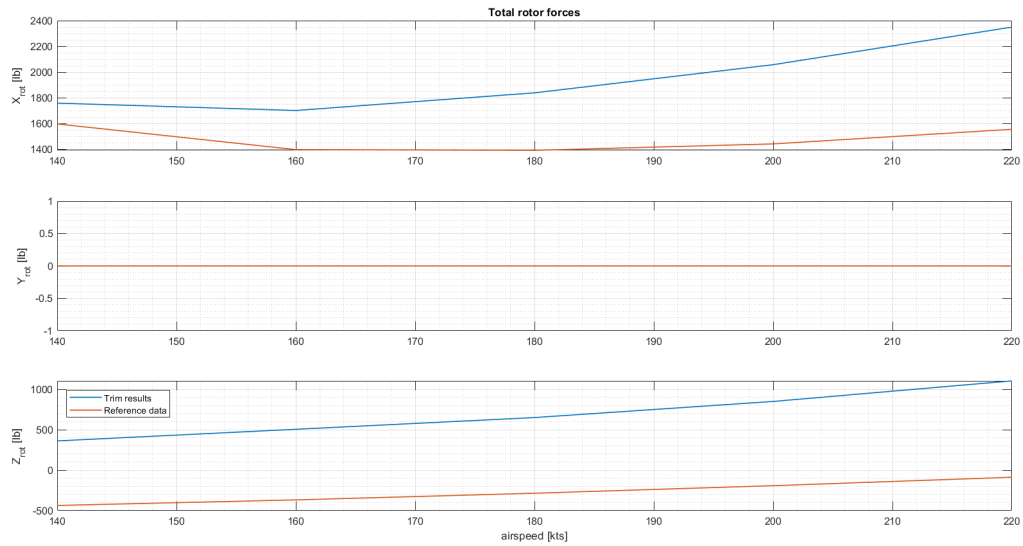


(a) Forces

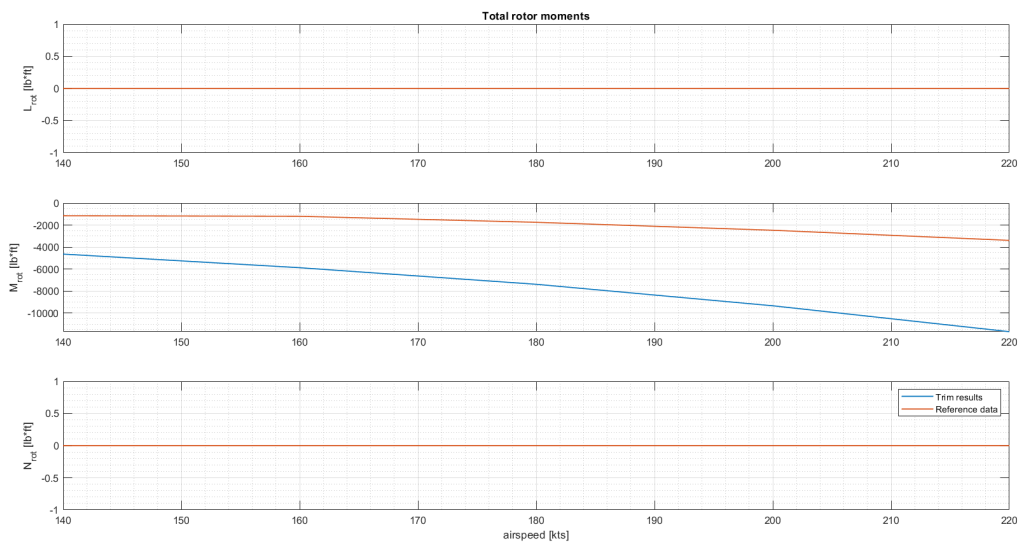


(b) Moments

Figure 5.7: Comparison of trim results – Overall rotor forces and moments, Helicopter mode



(a) Forces



(b) Moments

**Figure 5.8:** Comparison of trim results – Overall rotor forces and moments, Airplane mode, 517 rpm, 12 000 ft

## 5.2 Pilot-in-the-loop tests

As anticipated at the beginning of this chapter, validation of the model has also been performed by evaluating the piloting experience through a series of pilot-in-the-loop tests. To make the investigation as objective as possible, specific tasks have been defined, that could highlight the most significant characteristics of the behaviour of the simulated aircraft. The outcome of such tasks has been evaluated both by recording and analysing the simulation data, and by collecting the impressions of the pilots; the latter have been used to assess the level of handling qualities of the simulated aircraft, with particular reference to the Cooper-Harper rating scale (Figure C.1).<sup>3</sup>

All the piloted simulations were completed between the 10th and 14th February 2019. All tasks were carried out by helicopter pilots Davide Guscetti and Raphael Monstein of the ZAV Centre for Aviation of ZHAW. During each test, feedback from the pilots and additional notes by the author were registered in simplified flight test cards, a few examples of which are reported in Appendix C.

When planning the testing activities, the following limitations had to be taken into account:

- Although the model is suitable to simulate in-flight conversion between helicopter and airplane mode, a few major features still need to be implemented in the simulation platform before a realistic representation of this phase of flight can be obtained. Therefore, conversion was not investigated, and all tests were performed either completely in helicopter mode or entirely in airplane mode.
- Neither of the pilots involved in the activities is a test-pilot, and (as can be expected) neither of them has ever had any real experience piloting tilt-rotor aircraft. As a consequence, a significant amount of time was required by the pilots to become sufficiently acquainted with both the model and the appointed tasks.
- Test schedule was heavily conditioned by the limited availability of the pilots, of the ReDSim simulator, and of the author herself.

### 5.2.1 Helicopter mode

For the evaluation of the simulation in helicopter mode, the following three Mission Task Elements have been defined, with reference to the ADS-33E-PRF standard:<sup>4</sup>

- Hover task;
- Pirouette;
- Sidestep.

Before proceeding with the actual test session, the pilots had the possibility to familiarise with both the model and the test course by performing a series of free practice flights.

#### Overview

The first impression related by both pilots has been that the model is now more controllable and has a more predictable behaviour, compared to the previous versions. That said, the response is still very lively, with important oscillations especially in terms of pitch

<sup>3</sup>Pilots' evaluations have been recorded in the flight test cards reported in Appendix C.

<sup>4</sup>Reference [1]

and roll. The implementation of a rudimentary SCAS, having a simple proportional pitch damper and roll damper, has been sufficient to mitigate this undesired behaviour, providing higher stability and lower pilot workload.

While on one hand the increase of flight speed results in improved stability and controllability, on the other hand an unexpected and, so far, unexplained phenomenon was repeatedly observed: for airspeed higher than 60 - 70 knots, and usually in the presence of a certain amount of sideslip, pilots often experienced a variation of pitch and roll moment so sudden and violent that any attempt at recovery was useless and the simulation had to be aborted. An important clue regarding this irregular behaviour can be found in report CR-166537:

Results generally compare quite well [to XV-15 flight test data] at 90 deg nacelle incidence up to a calibrated airspeed of approximately 75 kts. At this airspeed, a strange thing happens in that the mathematical model predicts a strong nose-up pitching moment as the power required also increases dramatically. The XV-15 does not seem to exhibit this trend.<sup>5</sup>

The description reported above presents a striking similarity to what observed in the ReDSim model. Therefore, it might be possible that the cause of this phenomenon resides in the formulation of the mathematical model itself. A deeper and more detailed investigation needs to be conducted to explain and solve this issue.

Piloted simulations were also conditioned by a few deficiencies in the ReDSim simulator itself, especially in terms of stability of the visual system and integration of pilot controls. In particular, all tasks in helicopter mode have been performed without activating the Control Loading System, as, according to both pilots, the feedback provided by this system was not sufficiently realistic, being quite often even misleading.

### Hover task

**Task description** Starting from a ground speed of 6 to 10 knots and an altitude of less than 20 feet, the pilot shall approach the target hover point and decelerate so as to achieve a stabilised hover above the target; transition to hover should be accomplished in one smooth maneuver. At the start of the maneuver, the target hover point shall be oriented approximately 45 degrees relative to the heading of the aircraft.

To provide the pilot with adequate ground reference to detect deviations from the hovering condition, the test course was arranged as suggested by the ADS-33 and is represented in Figure 5.9.

---

<sup>5</sup>Reference [8, p. 34]

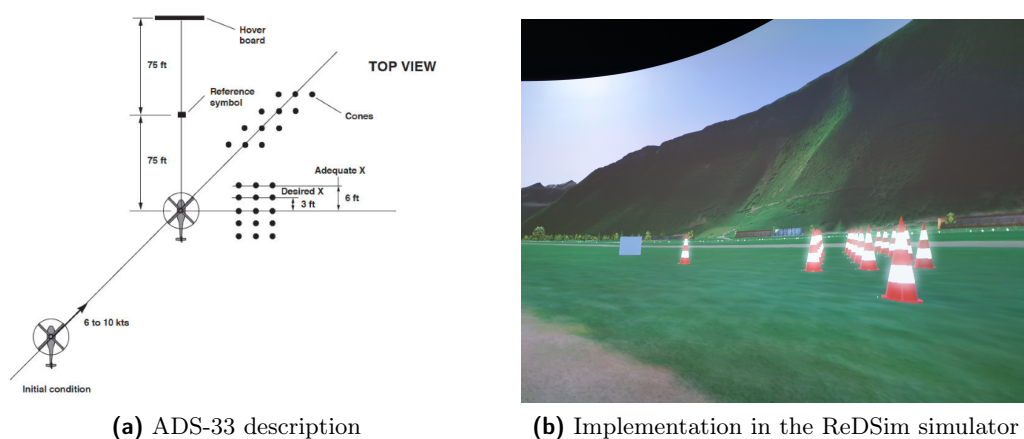


**Figure 5.9:** Test course for the Hover task

The performance standards defined within the ADS-33 for this task are reported in Table 5.2.

**Review of the task** Both the pilots' reports and the author's own observations agree in noting that deceleration to hover was far from being smooth and took much more time than required to classify the performance as adequate. In particular, when airspeed approached to null the simulated aircraft would become definitely unstable, making it difficult for the pilot to halt on the reference point and establish a stabilised hover.

Even when the hover condition was finally achieved, maintaining it required continuous pilot compensation. In particular, oscillations in both pitch and roll were very important, and at such a frequency that the pilot's corrections frequently ended up amplifying the instability instead of damping it. The activation of the SCAS did not succeed in entirely correcting this behaviour, but was all the same sufficient to allow the pilot to maintain a more or less stabilised hover for the 30 seconds required by the ADS-33. With the SCAS off, the hovering condition could be maintained for 15, 20 seconds at most, after which the pilot was forced to gain speed to avoid definitely losing control of the aircraft.

The outcome of the test was also significantly affected by some technical limits of the

**Table 5.2:** Performance standards for the Hover task (Reference [1])

	Desired	Adequate
Attain a stabilized hover within $X$ seconds of initiation of deceleration:	5 sec	8 sec
Maintain a stabilized hover for at least:	30 sec	30 sec
Maintain the longitudinal and lateral position within $\pm X$ ft of a point on the ground:	3 ft	6 ft
Maintain altitude within $\pm X$ ft:	2 ft	4 ft
Maintain heading within $\pm X$ deg:	5 deg	10 deg
There shall be no objectionable oscillations in any axis either during the transition to hover or the stabilized hover.	✓	✗

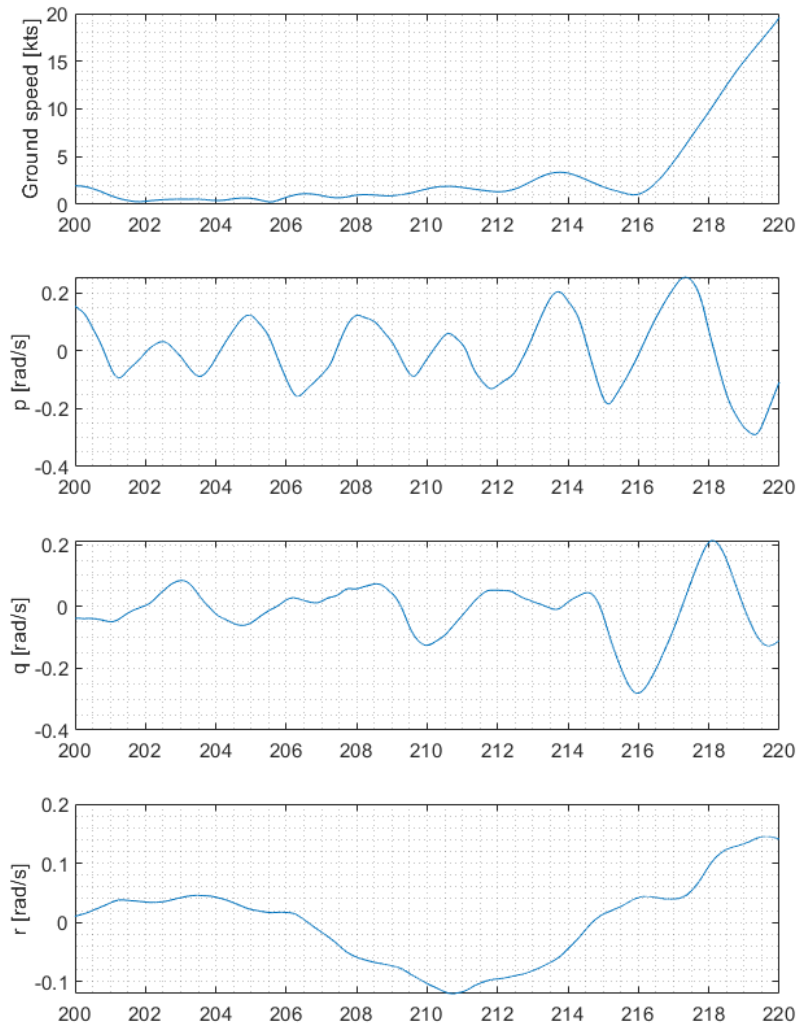


**Figure 5.10:** Simulation data records for Hover task, SCAS off – Aircraft angular rates

simulation environment. In particular, the low resolution of the image provided by the visual system, together with the absence of motion feedback, prevented the pilot from rapidly detecting variations in altitude and pitch – thus delaying the pilot’s response to such variations. Moreover, the view angle provided by the ReDSim curved screen was not wide enough to provide complete visibility of the visual cues placed on the side of the pilot.

**Results and evaluation** The simulation data recorded during the hovering tests confirm the observations reported above.

Considering an attempt at hovering with the SCAS off, it is easy to see from Figure 5.10 that important oscillations occur simultaneously around all three axes. This translates into a great amount of pilot workload: as can be observed from Figure 5.11, the pilot is forced to continuously act on all controls at the same time. It is also interesting to note the relation between the pilot’s inputs and the corresponding angular rates. Considering

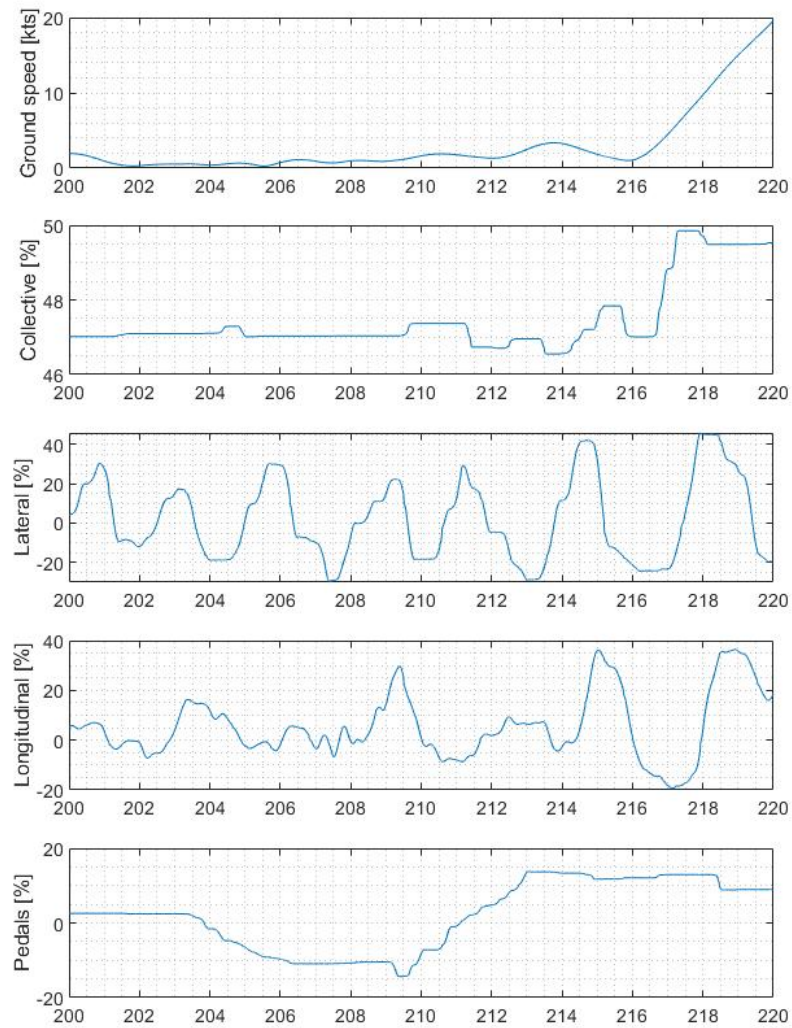


**Figure 5.11:** Simulation data records for Hover task, SCAS off – Pilot controls

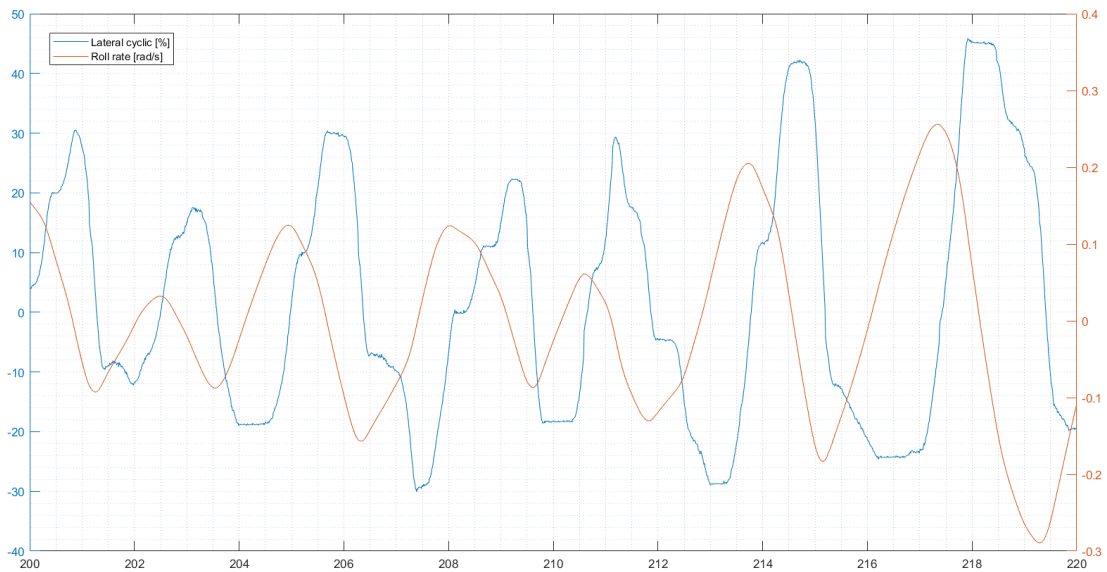


**Figure 5.12:** Simulation data records for Hover task, SCAS off – Comparison between lateral cyclic input and aircraft roll rate

for example the roll axis, the commanded lateral cyclic input and the aircraft roll rate are reported in Figure 5.12.

With the SCAS on, the amplitude of all oscillations is significantly reduced (Figure 5.13), to the point that the pilot was actually able to maintain a hovering condition for more than 30 seconds. Constant compensation in all axes is still needed, as can be observed from Figure 5.14, but with much shorter travel than in the case discussed above.

The aircraft ground speed and trajectory during a SCAS-on maneuver are reported in Figure 5.15. It is easy to see that establishing a more or less stabilised hover takes much longer time, since the initiation of deceleration, than the 8 seconds prescribed in the ADS-33; however, once such condition is finally achieved, the variations in altitude, lateral and longitudinal position are actually comparable with the standard requirements for an adequate performance.

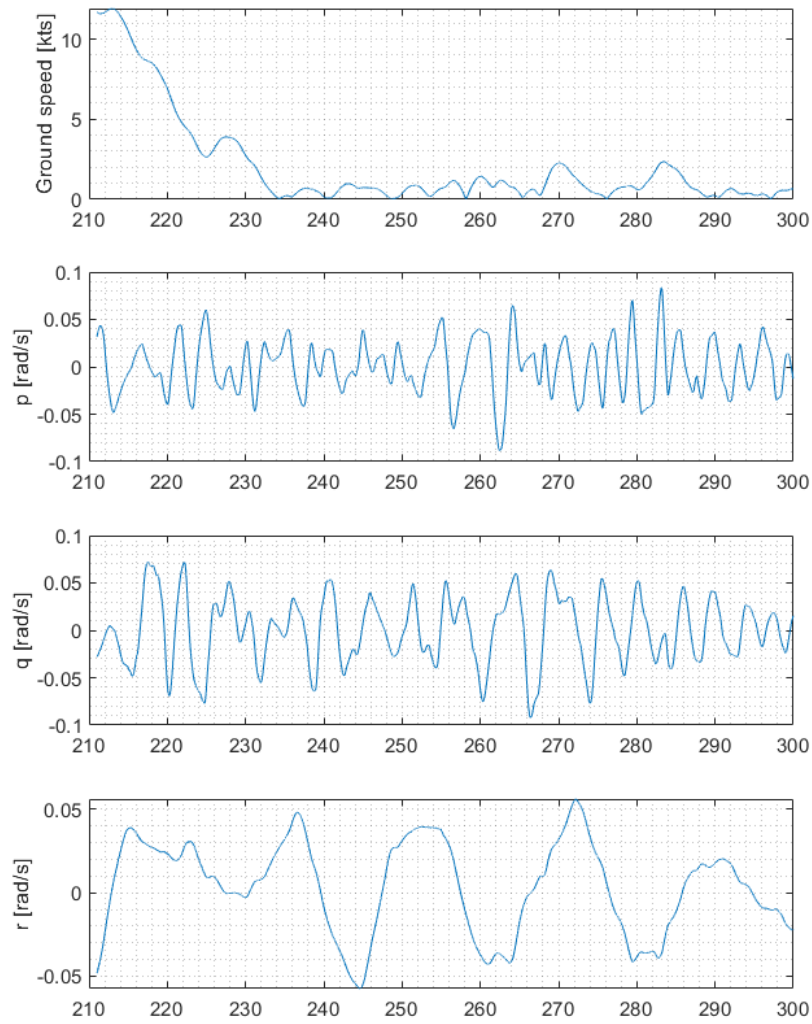


**Figure 5.13:** Simulation data records for Hover task, SCAS on – Aircraft angular rates

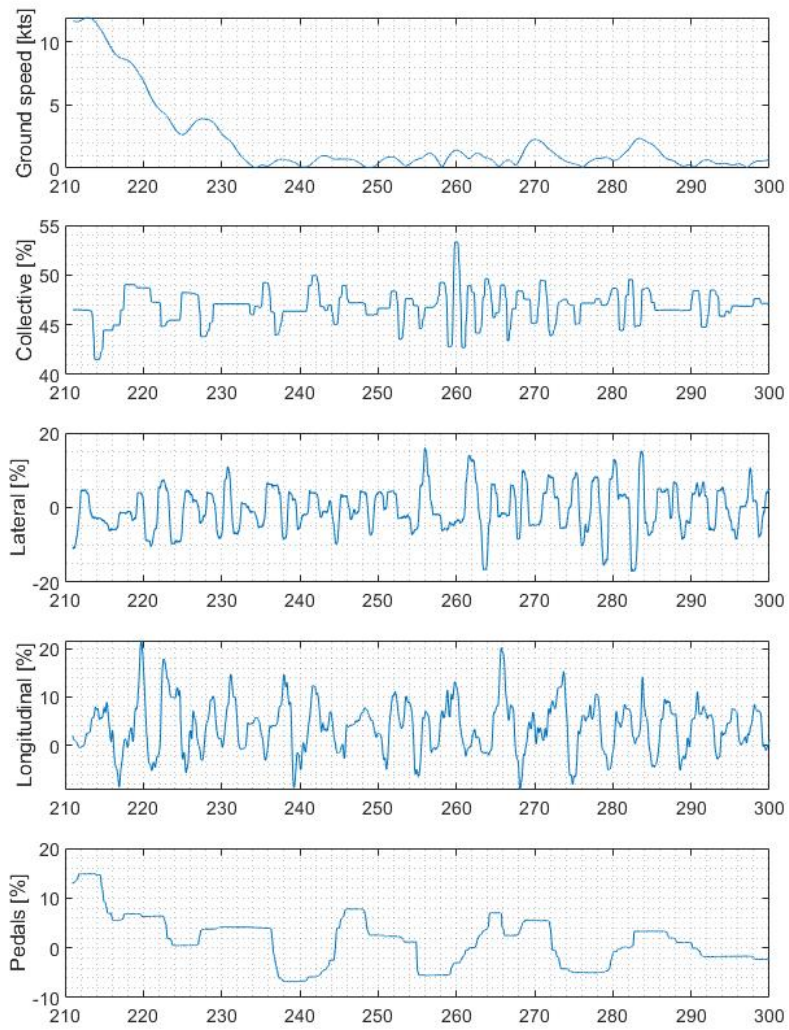


**Figure 5.14:** Simulation data records for Hover task, SCAS on – Pilot controls

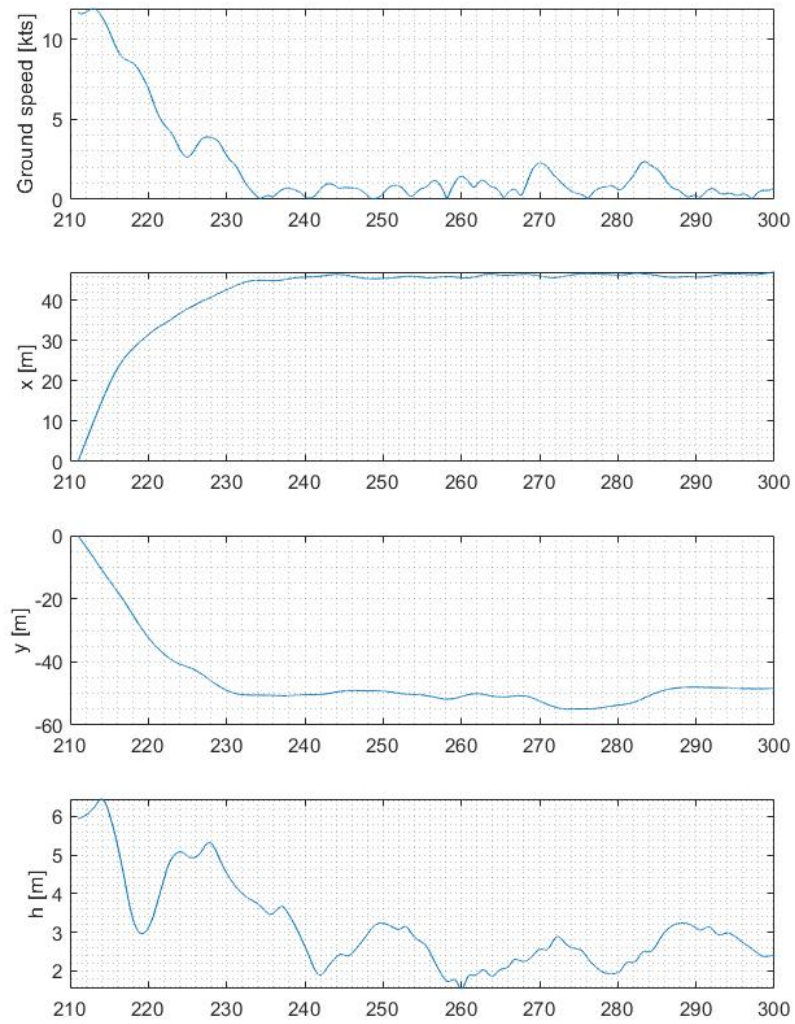


**Figure 5.15:** Simulation data records for Hover task, SCAS on – Trajectory

## Pirouette

**Task description** The test course for the Pirouette task consists of a 100-foot-radius circumference with a post at its centre and is represented in Figure 5.16.

Starting from a stabilised hover over a point on the circumference at an altitude of approximately 10 feet, the pilot shall accomplish a lateral translation around the whole circular pathway, keeping the nose of the aircraft pointed at the centre of the circle, and the circumference of the circle under a selected reference point on the aircraft. Lateral groundspeed should be maintained constant throughout the translation. The maneuver shall be concluded with a stabilised hover over the starting point. The pirouette should be performed both clockwise and counter-clockwise. The desired and adequate performance standards set by the ADS-33 are summarised in Table 5.3.

**Review of the task** Considered the difficulty of achieving and holding a stabilised hover, the author and pilots agreed on avoiding starting and concluding the Pirouette task with the prescribed 5-second hover. Pilots related that once a certain lateral speed was reached, the aircraft actually displayed sufficient stability to allow the task to be completed without excessive workload. This characteristic was maintained even when the SCAS was switched off, although in this case pitch oscillations became more evident; pilots also noted the presence of yaw oscillations, which had to be corrected with the pedals.

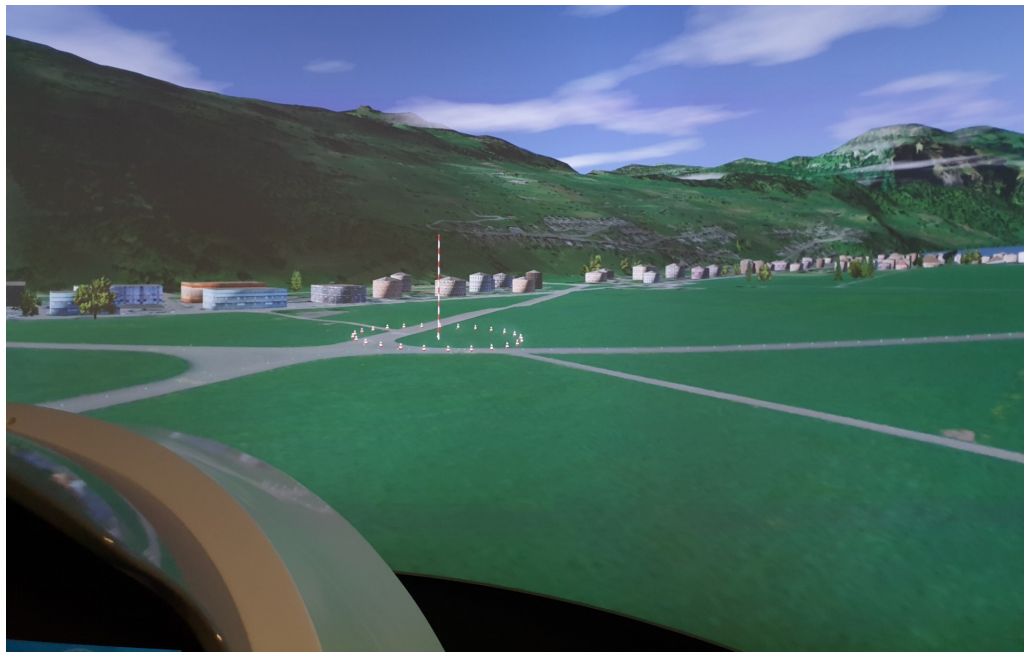
The issues related to the limits of the simulation environment were highlighted during this task as well, leading to difficulties in holding aircraft altitude and pitch attitude constant. In addition, the ReDSim cockpit configuration afforded very limited visibility on the left side (the pilot being seated on the right); therefore, performing the task clockwise was harder and resulted generally in worse performance.

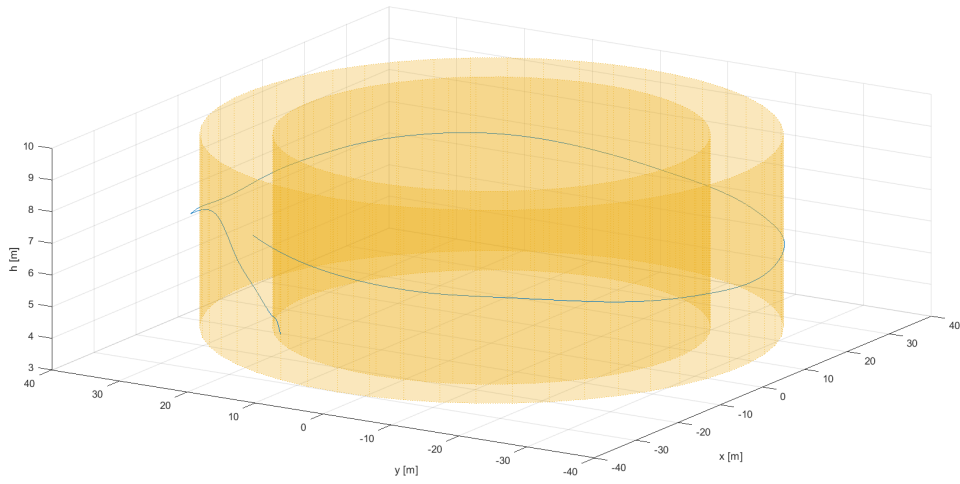
**Results and evaluation** Although it was not possible to achieve the required 5-second hover at the beginning and end of the task, the actual Pirouette maneuver could be performed, even with the SCAS off, with rather satisfactory results. The counter-clockwise, SCAS-off maneuver represented in the following figures was completed in 42 seconds and is aligned, as far as trajectory and altitude are concerned, with the ADS-33 standards for an adequate performance (Figure 5.17).

Figures 5.18 and 5.19 confirm that, as already observed by the pilots, an increase in lateral speed leads to better aircraft stability: as the maneuver progresses and the aircraft gains speed, oscillations of both roll and pitch angle decrease in amplitude, and the pilot's action, especially on the lateral and longitudinal cyclic, is limited to small corrections. Compensation with the pedals is required through the whole duration of the task.

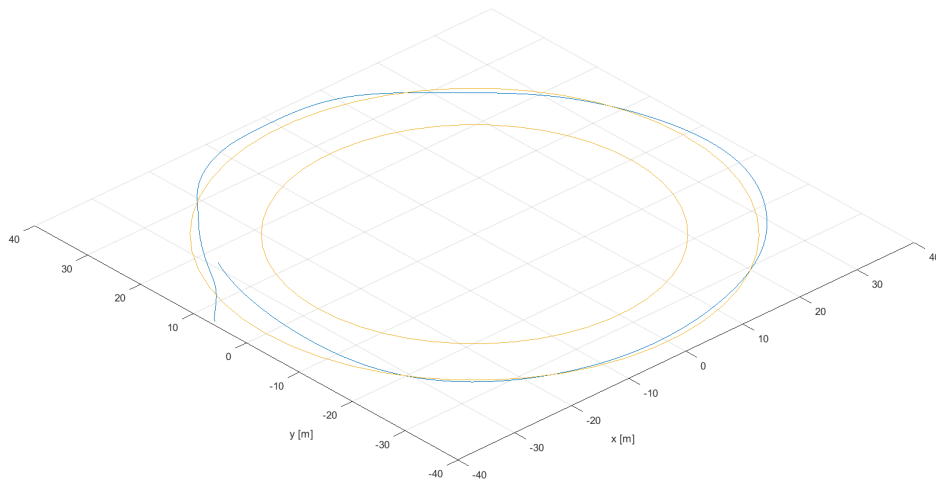
**Table 5.3:** Performance standards for the Pirouette task (Reference [1])

	Desired	Adequate
Maintain a selected reference point on the aircraft within $\pm X$ ft of the circumference of the circle:	10 ft	15 ft
Maintain altitude within $\pm X$ ft:	3 ft	10 ft
Maintain heading so that the nose of the aircraft points at the center of the circle within $\pm X$ deg:	10 deg	15 deg
Complete the circle and arrive back over the starting point within:	45 sec	60 sec
Achieve a stabilized hover (within desired hover reference point) within $X$ seconds after returning to the starting point:	5 sec	10 sec
Maintain the stabilized hover for $X$ sec:	5 sec	5 sec

**Figure 5.16:** Test course for the Pirouette task, as implemented in the ReDSim simulator



(a)



(b)

**Figure 5.17:** Simulation data records for Pirouette task, SCAS off – Trajectory (the yellow boundaries indicate the requirements for adequate performance)

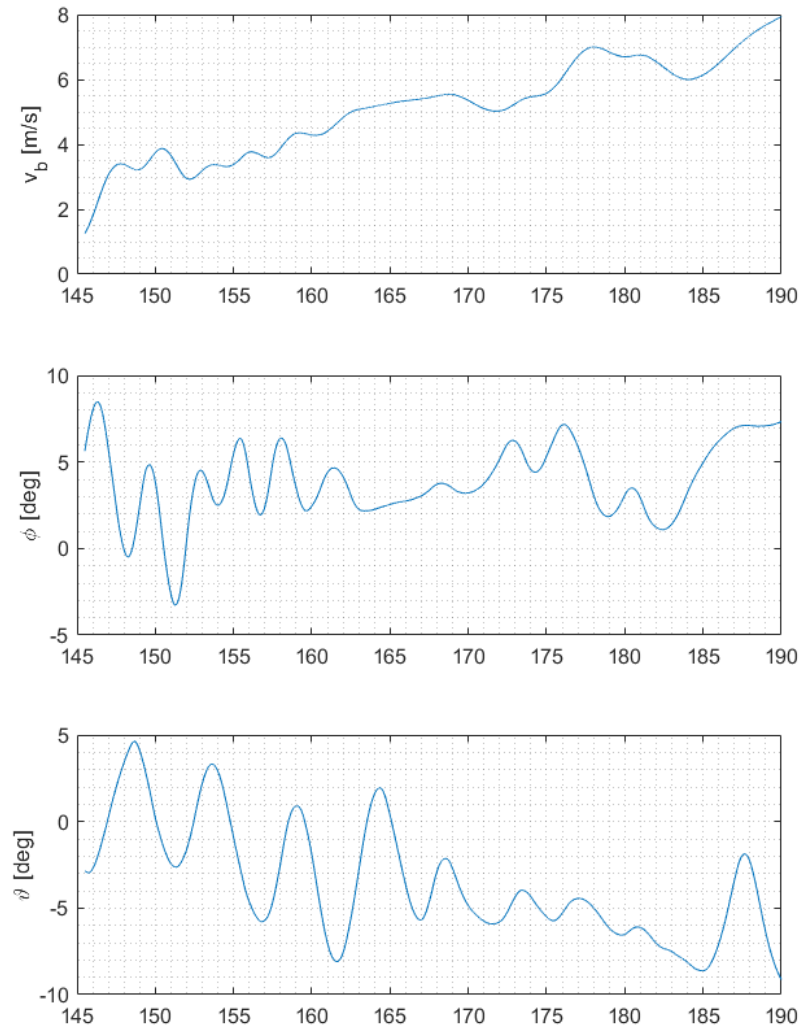


**Figure 5.18:** Simulation data records for Pirouette task, SCAS off – Lateral speed, roll angle and pitch angle

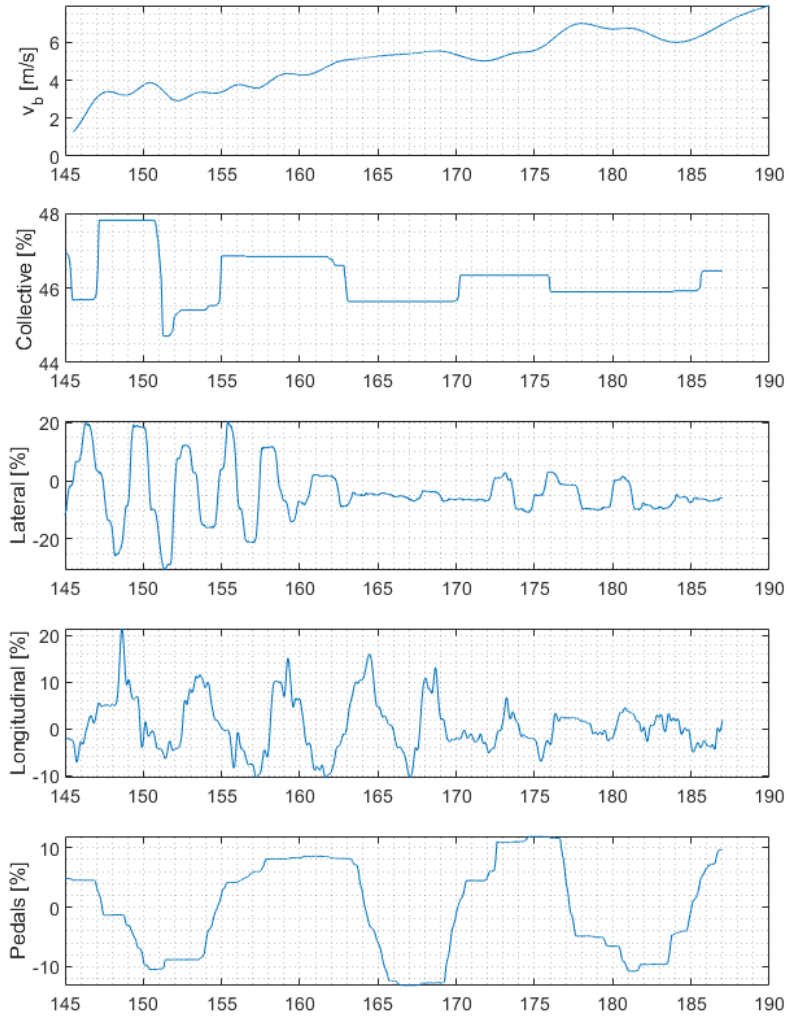


**Figure 5.19:** Simulation data records for Pirouette task, SCAS off – Pilot controls

### Sidestep

**Task description** The task starts with a stabilised hover over a point on a reference line marked on the ground, with the longitudinal axis of the aircraft oriented 90 degrees to said reference line. The pilot shall then initiate a rapid lateral acceleration at constant altitude, until a target lateral velocity is reached (in this case, target speed has been set to 20 knots). After holding the target velocity for 5 seconds, the pilot shall perform an aggressive deceleration at constant altitude to again establish a stabilised hover. Hover shall be maintained for 5 seconds, before immediately repeating the whole maneuver in the opposite direction. Table 5.4 contains the performance standards for the Sidestep task, as defined in the ADS-33.

The test course employed for this task is based on the one suggested in the ADS-33 and is represented in Figure 5.20.

**Review of the task** In a task such as the Sidestep, in which a lateral translation is required, the visibility problems due to the cockpit configuration and limited view angle of the ReDSim played a major role and affected in a negative way the achievable performance. Seeing the reference line from the cockpit while keeping the required aircraft orientation was not possible. This being the case, the pilots used two different approaches to get around this issue:

- The first pilot performed the whole task keeping the aircraft a few metres behind the reference line, rather than over it; this choice allowed him to maintain a constant heading, but made it more difficult to effectively achieve a straight trajectory.
- The second pilot, on the other hand, remained over the reference line but slightly tilted the nose of the aircraft in the direction of the translation, so as to command a better view of the visual cues. This way, following the reference line was easier, but also required additional compensation in the longitudinal plane.

The task proved extremely difficult to complete even with the SCAS on. In particular, performing the sidestep maneuver in a more aggressive way caused greater oscillations and resulted in reduced precision in following the prescribed trajectory and keeping altitude constant. On the contrary, a less aggressive maneuver allowed to better follow the reference line but prevented the fulfillment of bank angle and lateral speed requirements. Furthermore, achieving a stabilised hover as demanded by the ADS-33 was extremely problematic.

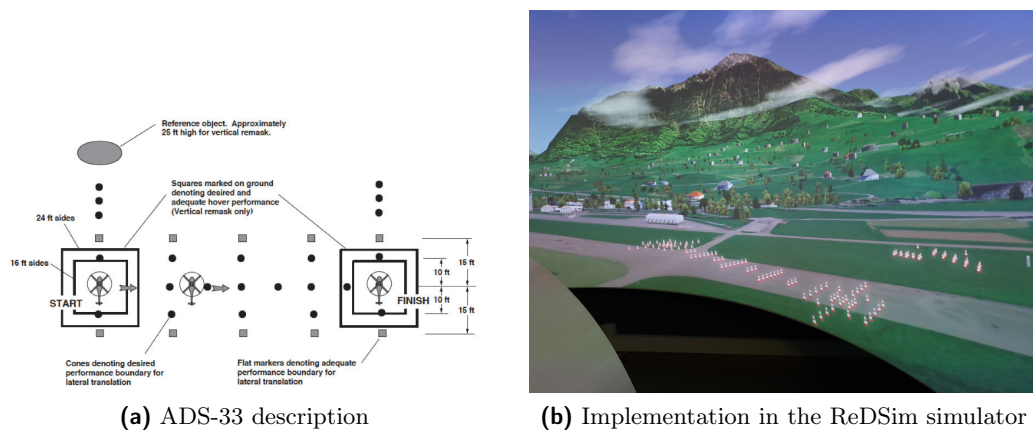


**Figure 5.20:** Test course for the Sidestep task

**Table 5.4:** Performance standards for the Sidestep task (Reference [1])

	Desired	Adequate
Achieve at least 25 deg of bank angle change from trim, or target airspeed, within $X$ sec of initiating the maneuver:	1.5 sec	3.0 sec
Achieve a target airspeed of $X$ kts:	< 40 kts	< 40 kts
Achieve at least 30 deg of bank angle within $X$ sec of initiating deceleration:	1.5 sec	3.0 sec
Maintain selected reference point on the aircraft within $\pm X$ ft of the ground reference line:	10 ft	15 ft
Maintain altitude within $\pm X$ ft at a selected altitude below 30 ft:	10 ft	15 ft
Maintain heading within $\pm X$ deg:	10 deg	15 deg
Achieve a stabilized hover within $X$ sec after reaching the hover point:	5 sec	10 sec

A few attempts were also made at performing the task with the SCAS off, but the impossibility of establishing a stable hover on one side, and the significant pitch oscillations on the other, always resulted in the abortion of the maneuver.

**Results and evaluation** The following figures report simulation data for a sidestep maneuver carried out by the first pilot. The task was performed in a rather aggressive way, reaching lateral speeds of more than 30 knots (Figure 5.21) and a peak bank angle of 30 degrees (Figure 5.22). The higher aggressiveness, combined with the lack of appropriate visual cues, resulted however in higher fluctuations of both altitude and longitudinal position. In particular, with the increase in lateral speed the aircraft appears to also move forwards.

The difficulty in reaching a hover condition is evident from the presence of significant pitch and roll oscillations in the central part of the diagrams in Figure 5.22. A high amount of corrections is also required to the pilot through the entire duration of the task (Figure 5.23)

A "softer" maneuver, such as the one performed by the second pilot and described in Figures 5.24 to 5.27, allows the pilot to better follow the reference line, meeting the requirements for an adequate trajectory. Oscillations, especially in the pitch axis, are also significantly reduced. Nevertheless, pilot workload is still definitely unacceptable.

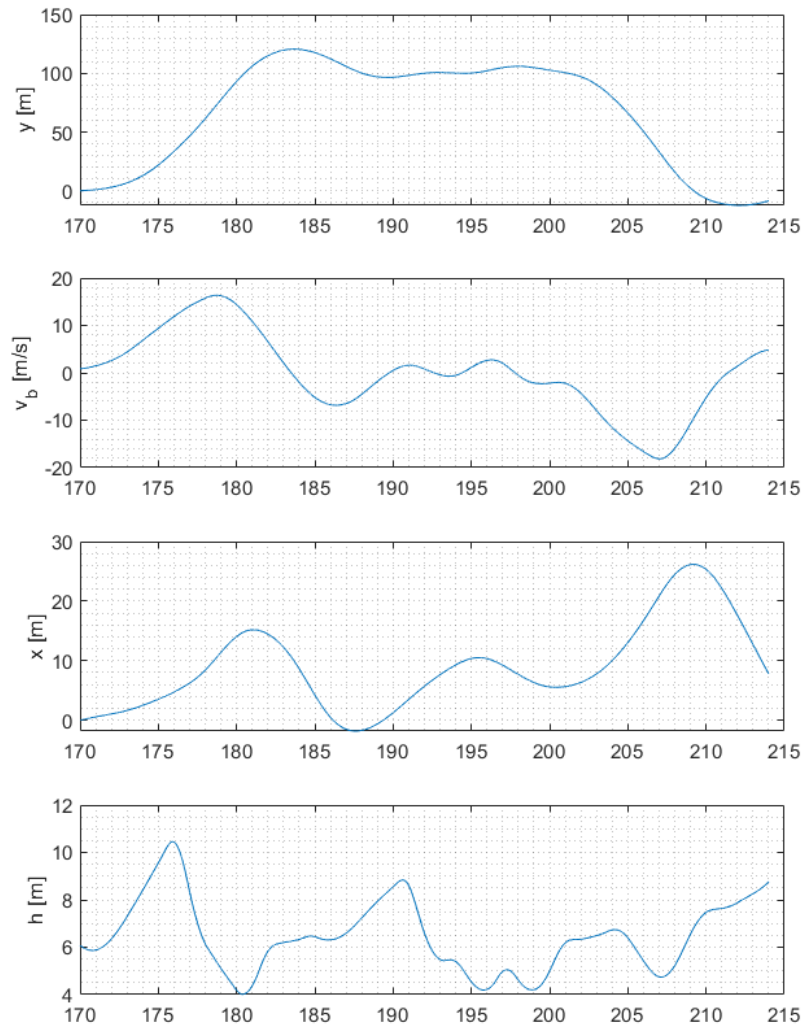


**Figure 5.21:** Simulation data records for Sidestep task, SCAS on, Pilot 1 – Lateral speed and trajectory

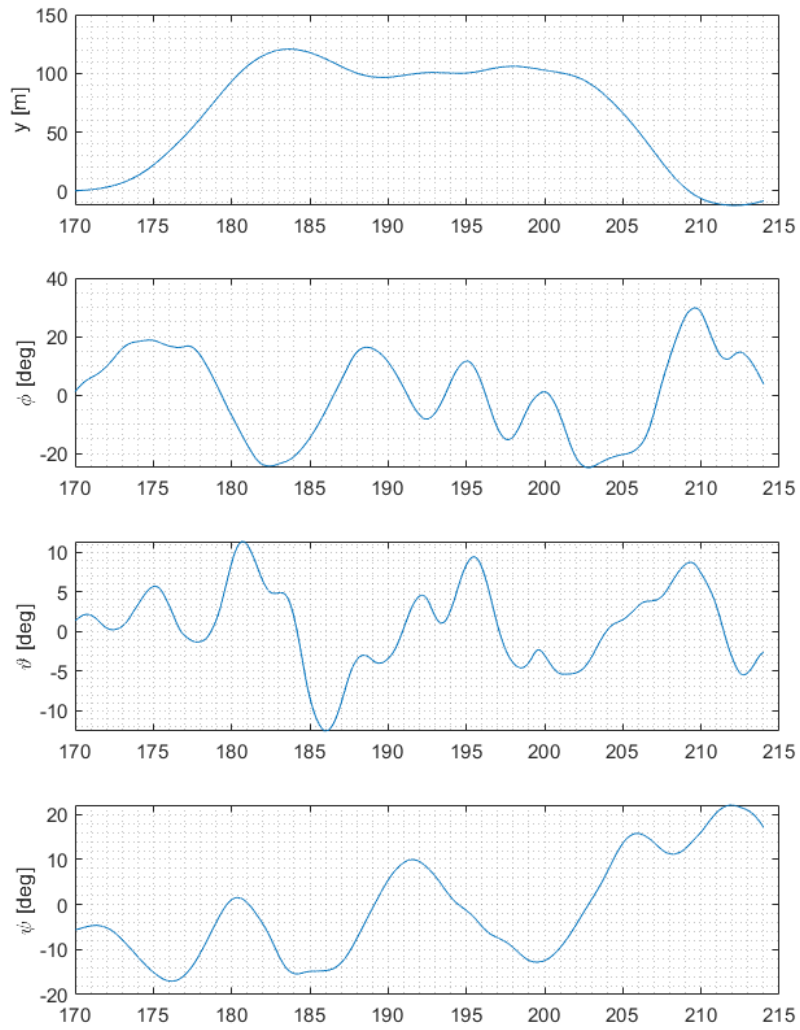


**Figure 5.22:** Simulation data records for Sidestep task, SCAS on, Pilot 1 – Euler angles

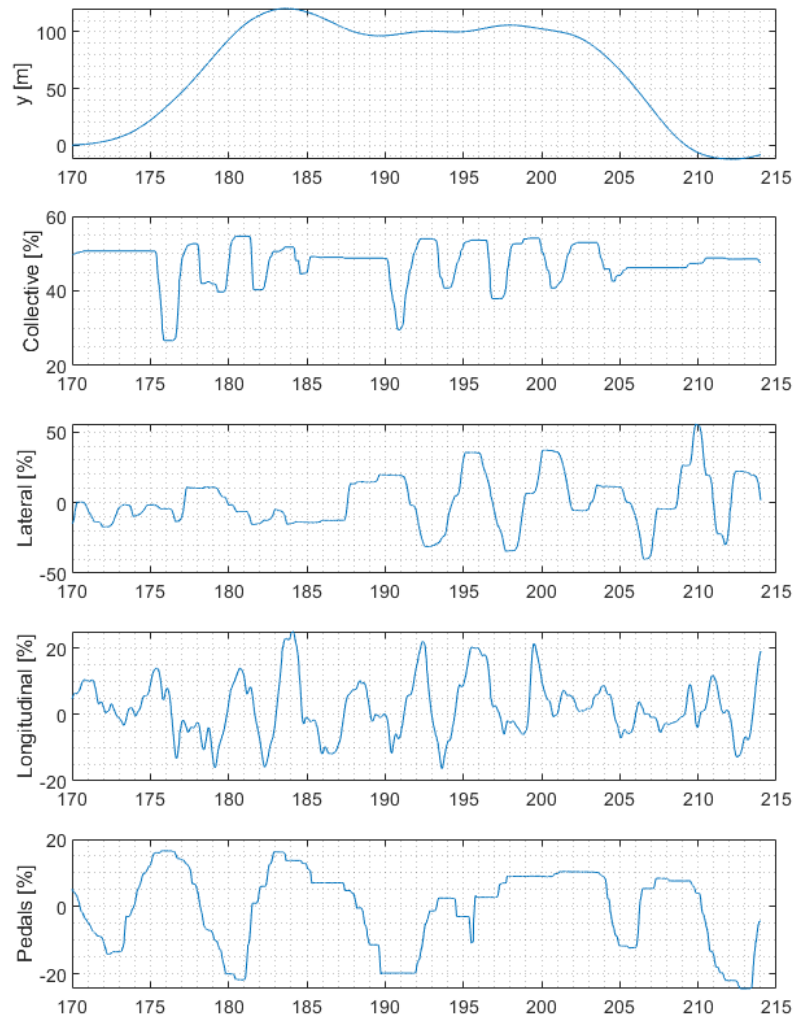


**Figure 5.23:** Simulation data records for Sidestep task, SCAS on, Pilot 1 – Pilot controls

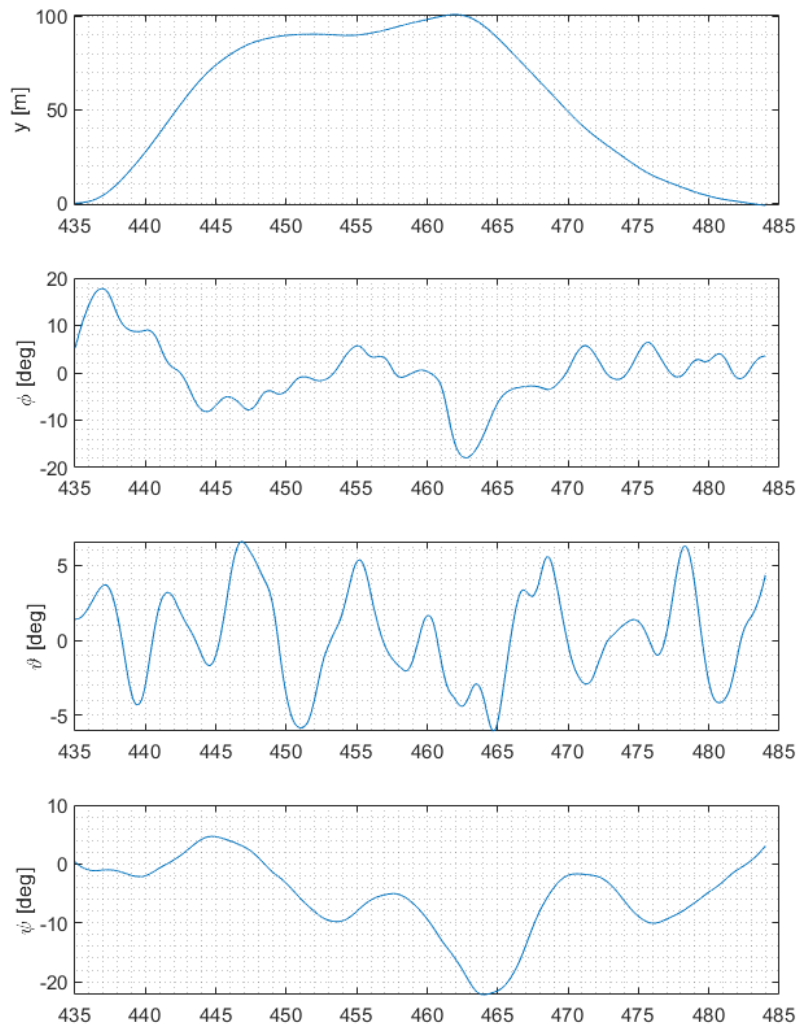


**Figure 5.24:** Simulation data records for Sidestep task, SCAS on, Pilot 2 – Euler angles

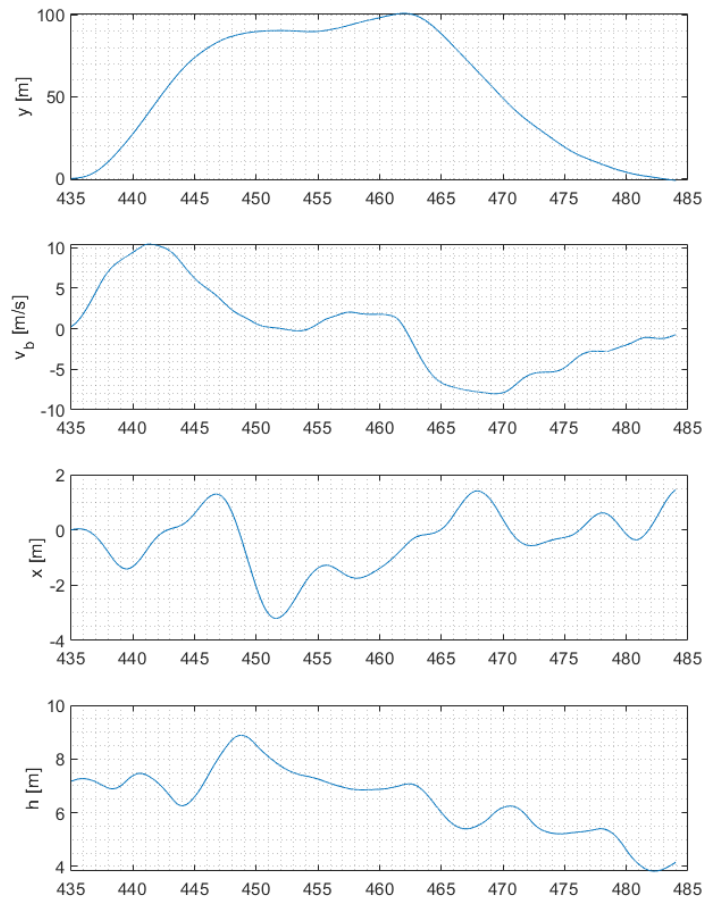


**Figure 5.25:** Simulation data records for Sidestep task, SCAS on, Pilot 2 – Lateral speed and trajectory

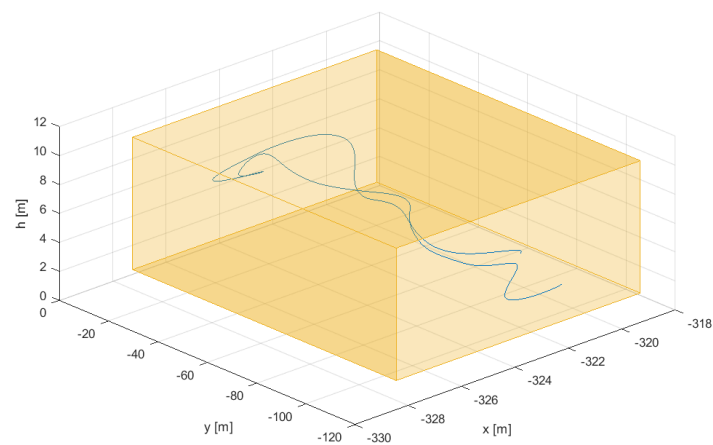


**Figure 5.26:** Simulation data records for Sidestep task, SCAS on, Pilot 2 – Trajectory (the yellow boundaries indicate the requirements for adequate performance)

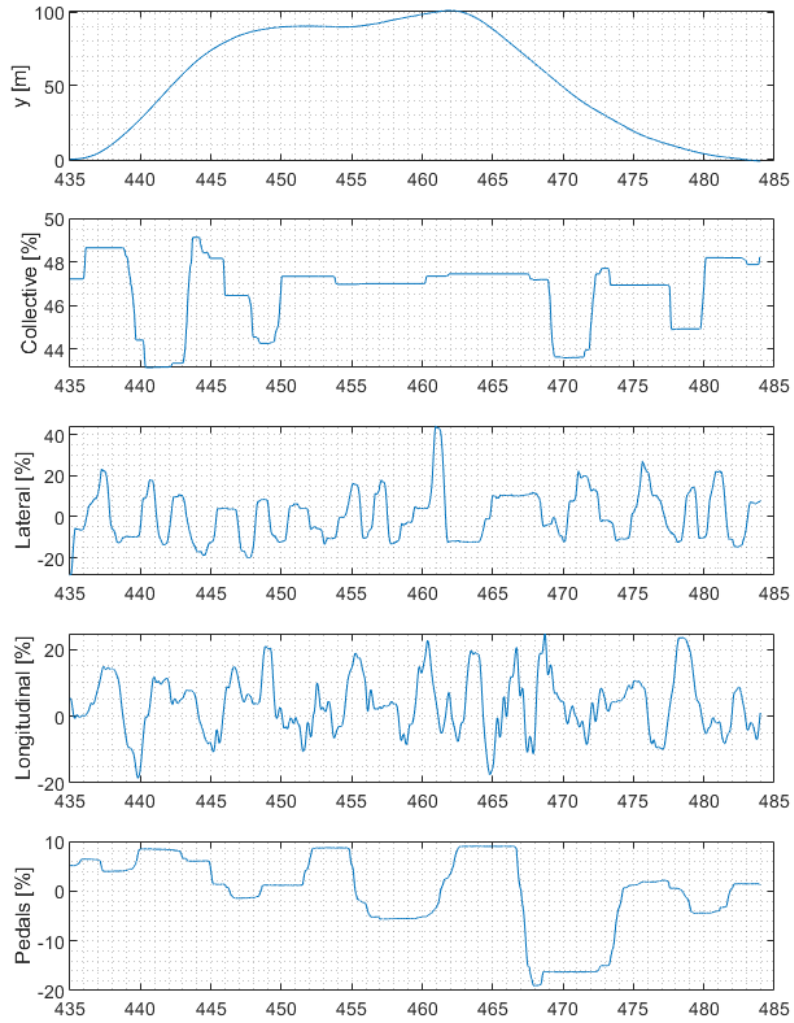


**Figure 5.27:** Simulation data records for Sidestep task, SCAS on, Pilot 2 – Pilot controls

### 5.2.2 Airplane mode

#### Overview

All tests in airplane mode were started from a trim condition, namely level flight at 120 knots, at an altitude of 550 metres.

The first attempts at flying the simulator in airplane mode highlighted an incoherent response of the model to pilot inputs. A rapid review of the model led to the detection of a few inverted signs related to the deflections of both the rudder and ailerons. This fact had not been noticed in previous helicopter mode tests, as these flight control surfaces have limited authority in low speed regimes. Following the correction of this error the model responded in a proper way to pilot commands and could be flown without any problems.

Since the engine model had not been implemented yet, the simulated aircraft was much overpowered. Although this characteristic was not relevant for the purpose of the current tests, it led all the same to experience flight conditions that significantly exceeded the actual XV-15 flight envelope, especially in terms of cruise speed climb rate.

The model in airplane mode appears controllable and rather easy to fly. However, the fact that power control is achieved using the collective lever, and that this function has not been properly calibrated yet, leads the piloting experience to be still not completely faithful to reality. On the other hand, the Control Loading System provides a much more realistic feedback in this mode of flight than in helicopter mode, and was kept active for the whole duration of the airplane-mode tests.

In general, the simulated aircraft is very responsive: a minimum input from the pilot generates immediately evident effects. Important and low-damped oscillations have been observed especially in the roll axis; again, the implementation of a simple SCAS with proportional pitch and roll damper improved significantly the overall stability of the aircraft.

#### Rudder kicks

To evaluate the response of the aircraft in the lateral-directional plane, the pilot was asked to give a rapid doublet input with the pedals, and then maintain all controls fixed until all oscillations subsided.

As far as the assigned task was concerned, both the pilot's perceptions and the simulation data attest that the Rudder kicks maneuver produced highly damped oscillations in both roll and yaw. Such oscillations can be observed in the first 10 seconds of the time history reported in Figure 5.29.

Interesting information comes also from the second part of the same test flight, where, following a lateral input given by the pilot, high-amplitude, low-damped oscillations appear in both roll and pitch rate.

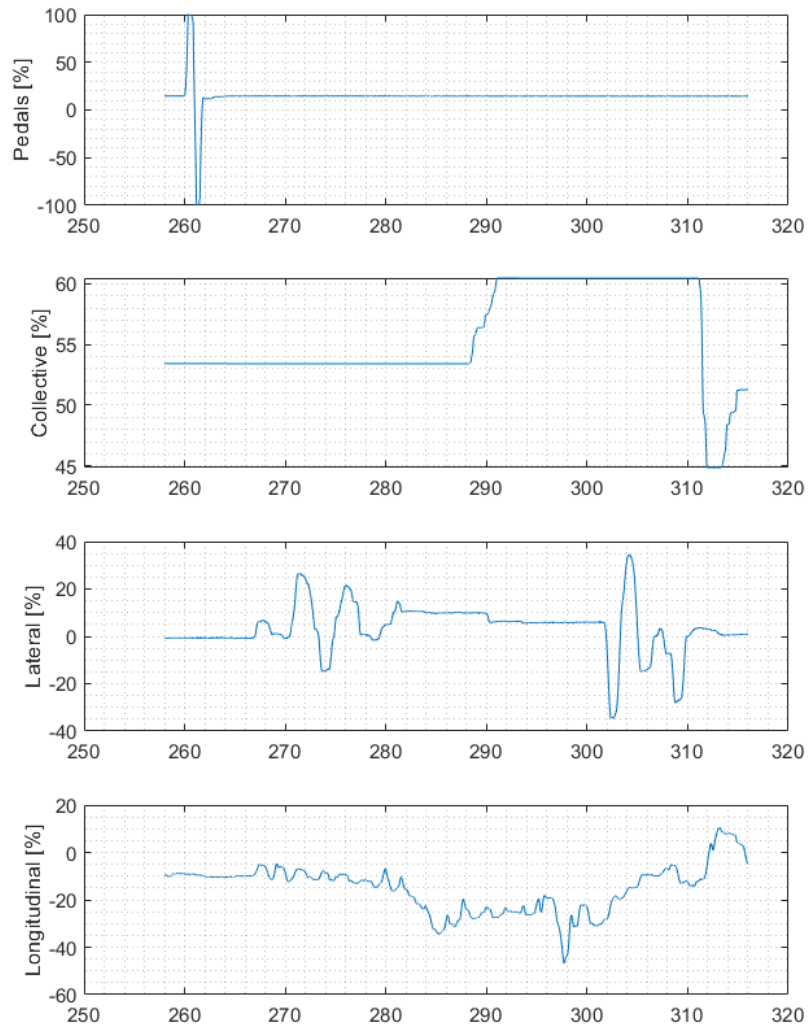


**Figure 5.28:** Simulation data records for airplane mode, SCAS off – Pilot controls

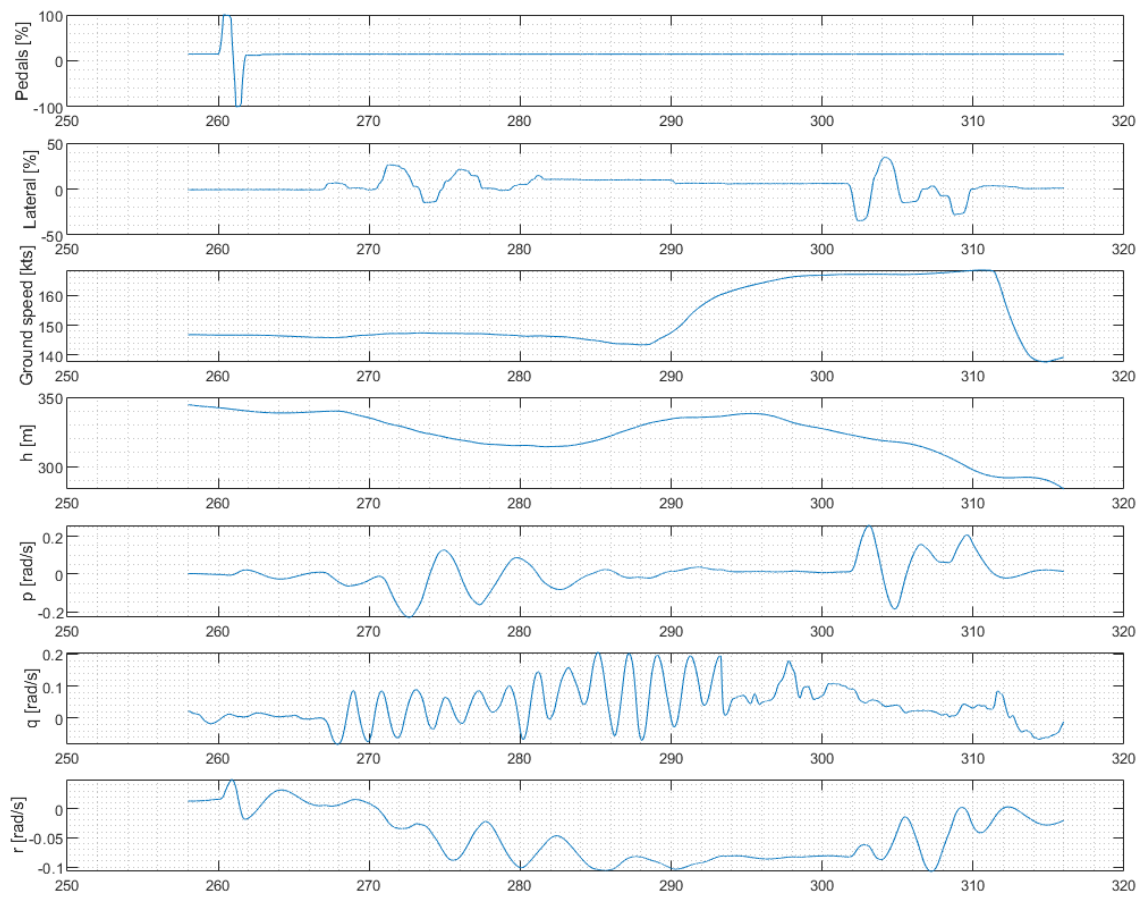


**Figure 5.29:** Simulation data records for airplane mode, SCAS off – Ground speed, altitude and angular rates



## Chapter 6

# Conclusions

The main result of the work carried out by the author is represented by a significant improvement of the tilt-rotor model implemented in the ZAV ReDSim flight simulator. The model is now more realistic and controllable both in helicopter and in airplane mode, as testified by several piloted simulations. In addition, it is now possible to trim the model, with satisfying results especially within low-speed flight conditions.

Such results have been obtained thanks to a series of activities focused mainly on the rotor model, and particularly through:

- an extensive review of the existing model, with subsequent correction of all detected errors;
- the removal of several simplifications and approximations;
- the introduction of a new formulation of rotor flapping dynamics, capable of reproducing with higher fidelity the dynamic behaviour of a gimbaled rotor, while still complying with the requirements for a real-time simulation.

The various activities performed for the purpose of this thesis highlighted a few issues, which exceed the scope of this work, but shall be necessarily addressed in order to further improve the tilt-rotor model. These aspects can represent a good starting point for planning the next steps to be taken within the present project:

- The same review and debugging work carried out by the author on the rotor model should be extended also to all other subsystems in the aircraft model.
- The rotor model itself still needs to be refined and fully validated; future efforts shall be especially oriented at improving the representation of the airplane mode of flight.
- A deep investigation shall be conducted to finally determine the actual range of rotor blade collective pitch available for each mode of flight; the automatic variation of such range during conversion shall be implemented into the model.
- A representation of the rotor collective governor as well as engine dynamics still needs to be developed and included into the aircraft model.



# Appendix A

## Rotor mathematical model equations

### A.1 Blade position, speed and acceleration

In the following sections, position, speed and acceleration of a generic blade section S are determined, with respect to the three frames of reference defined in Section 3.1.1.

Conversion between different reference frames is obtained by means of the following rotation matrices.

From Blade system to Rotating system:

$$T_{\beta} = \begin{bmatrix} \cos \beta & 0 & -\sin \beta \\ 0 & 1 & 0 \\ \sin \beta & 0 & \cos \beta \end{bmatrix}$$

From Rotating system to Hub system:

$$T_{\psi} = \begin{bmatrix} -\cos \psi & \sin \psi & 0 \\ \sin \psi & \cos \psi & 0 \\ 0 & 0 & -1 \end{bmatrix}$$

The following vectors are defined, representing, respectively, the aircraft linear speed, linear acceleration, rotational speed and rotational acceleration, with respect to the Hub reference frame:

$$\begin{aligned} V_h &= \begin{bmatrix} u_h \\ v_h \\ w_h \end{bmatrix} & a_h &= \begin{bmatrix} \dot{u}_h \\ \dot{v}_h \\ \dot{w}_h \end{bmatrix} \\ \omega_h &= \begin{bmatrix} p_h \\ q_h \\ r_h \end{bmatrix} & \dot{\omega}_h &= \begin{bmatrix} \dot{p}_h \\ \dot{q}_h \\ \dot{r}_h \end{bmatrix} \end{aligned}$$

#### A.1.1 Position

Position vector of the blade section in the Blade reference frame:

$$r_{S,b} = \begin{bmatrix} r \\ 0 \\ 0 \end{bmatrix}$$

Position of S in the Rotating reference frame:

$$r_{S,r} = T_\beta \cdot r_{S,b} + \begin{bmatrix} e \\ 0 \\ 0 \end{bmatrix} = \begin{bmatrix} \cos(\beta) r + e \\ 0 \\ \sin(\beta) r \end{bmatrix}$$

Position with respect to the Hub reference system:

$$r_{S,h} = T_\psi \cdot r_{S,r} = \begin{bmatrix} -\cos(\psi) (\cos(\beta) r + e) \\ \sin(\psi) (\cos(\beta) r + e) \\ -\sin(\beta) r \end{bmatrix}$$

### A.1.2 Speed

The speed of the blade section in the Rotating reference frame is composed of the following three contributions.

1. Relative speed of S with respect to the Rotating system, due to blade rotation around the flapping hinge:

$$V_{S,rel,r} = T_\beta \cdot \left( \begin{bmatrix} 0 \\ -\dot{\beta} \\ 0 \end{bmatrix} \times r_{S,b} \right) = \begin{bmatrix} -\sin(\beta) \dot{\beta} r \\ 0 \\ \cos(\beta) \dot{\beta} r \end{bmatrix}$$

2. Linear speed of the origin of the Rotating system (due to aircraft motion):

$$V_r = T_\psi^{-1} \cdot V_h = \begin{bmatrix} -\cos(\psi) u_h + \sin(\psi) v_h \\ \sin(\psi) u_h + \cos(\psi) v_h \\ -w_h \end{bmatrix}$$

3. Tangential speed owing to reference frame rotation, which in turn is due to aircraft motion and rotor spinning:

$$V_{S,tang,r} = \omega_r \times r_{S,r} = \begin{bmatrix} (\sin(\psi) p_h + \cos(\psi) q_h) \sin(\beta) r \\ -(-\cos(\psi) p_h + \sin(\psi) q_h) \sin(\beta) r + (-r_h + \Omega) (\cos(\beta) r + e) \\ -(\sin(\psi) p_h + \cos(\psi) q_h) (\cos(\beta) r + e) \end{bmatrix}$$

where:

$$\omega_r = T_\psi^{-1} \cdot \omega_h + \begin{bmatrix} 0 \\ 0 \\ \Omega \end{bmatrix} = \begin{bmatrix} -\cos(\psi) p_h + \sin(\psi) q_h \\ \sin(\psi) p_h + \cos(\psi) q_h \\ -r_h + \Omega \end{bmatrix}$$

Therefore, the total section speed in the Rotating reference frame is:

$$V_{S,r} = V_{S,rel,r} + V_r + V_{S,tang,r}$$

The resulting vectos has the following components:

$$V_{S,r}[1] = -\sin(\beta) \dot{\beta} r - \cos(\psi) u_h + \sin(\psi) v_h + (\sin(\psi) p_h + \cos(\psi) q_h) \sin(\beta) r$$

$$V_{S,r}[2] = \sin(\psi) u_h + \cos(\psi) v_h - (-\cos(\psi) p_h + \sin(\psi) q_h) \sin(\beta) r + \\ + (-r_h + \Omega) (\cos(\beta) r + e)$$

$$V_{S,r}[3] = \cos(\beta) \dot{\beta} r - w_h - (\sin(\psi) p_h + \cos(\psi) q_h) (\cos(\beta) r + e)$$

Blade section speed in the Blade system can be computed as:

$$V_{S,b} = T_\beta^{-1} \cdot V_{S,r}$$

which yields the following components:

$$V_{S,b}[1] = (-e \cos(\psi) q_h - e \sin(\psi) p_h - w_h) \sin(\beta) - \cos(\beta) (\cos(\psi) u_h - \sin(\psi) v_h)$$

$$V_{S,b}[2] = r(-r_h + \Omega) \cos(\beta) + r(\cos(\psi) p_h - \sin(\psi) q_h) \sin(\beta) + \cos(\psi) v_h + \sin(\psi) u_h + \\ + e(-r_h + \Omega)$$

$$V_{S,b}[3] = \dot{\beta} r + (-e \cos(\psi) q_h - e \sin(\psi) p_h - w_h) \cos(\beta) + (\sin(\beta) u_h - r q_h) \cos(\psi) + \\ - \sin(\psi) (v_h \sin(\beta) + r p_h)$$

In a similar way, blade section speed in the Hub reference system is determined as:

$$V_{S,h} = T_\psi \cdot V_{S,r}$$

### A.1.3 Acceleration

The blade section acceleration in the Rotating reference frame is made up by the sum of the following five contributions:

1. Relative acceleration of S (due to blade flapping) with respect to the Rotating system, which in turn comprises a tangential and a centrifugal component:

$$a_{S,rel,r} = T_\beta \cdot \left( \left( \begin{bmatrix} 0 \\ -\ddot{\beta} \\ 0 \end{bmatrix} \times r_{S,b} + \begin{bmatrix} 0 \\ -\dot{\beta} \\ 0 \end{bmatrix} \times \left( \begin{bmatrix} 0 \\ -\dot{\beta} \\ 0 \end{bmatrix} \times r_{S,b} \right) \right) = \\ = \begin{bmatrix} -\cos(\beta) \dot{\beta}^2 r - \sin(\beta) \ddot{\beta} r \\ 0 \\ -\sin(\beta) \dot{\beta}^2 r + \cos(\beta) \ddot{\beta} r \end{bmatrix}$$

2. Linear acceleration of the origin of the Rotating system (due to aircraft motion):

$$a_r = T_\psi^{-1} \cdot a_h = \begin{bmatrix} -\cos(\psi) \dot{u}_h + \sin(\psi) \dot{v}_h \\ \sin(\psi) \dot{u}_h + \cos(\psi) \dot{v}_h \\ -\dot{w}_h \end{bmatrix}$$

3. Tangential acceleration owing to reference frame angular acceleration, which in turn is due to aircraft motion and rotor angular acceleration:

$$a_{S,tang,r} = \dot{\omega}_r \times r_{S,r} = \begin{bmatrix} (\sin(\psi) \dot{p}_h + \cos(\psi) \dot{q}_h) \sin(\beta) r \\ -(-\cos(\psi) \dot{p}_h + \sin(\psi) \dot{q}_h) \sin(\beta) r + (-\dot{r}_h + \dot{\Omega}) (\cos(\beta) r + e) \\ -(\sin(\psi) \dot{p}_h + \cos(\psi) \dot{q}_h) (\cos(\beta) r + e) \end{bmatrix}$$

where:

$$\dot{\omega}_r = T_\psi^{-1} \times \dot{\omega}_h + \begin{bmatrix} 0 \\ 0 \\ \dot{\Omega} \end{bmatrix} = \begin{bmatrix} -\cos(\psi) \dot{p}_h + \sin(\psi) \dot{q}_h \\ \sin(\psi) \dot{p}_h + \cos(\psi) \dot{q}_h \\ -\dot{r}_h + \dot{\Omega} \end{bmatrix}$$

4. Centrifugal acceleration, due to rotation of the Rotating reference frame:

$$a_{S,centr,r} = \omega_r \times (\omega_r \times r_{S,r})$$

whose components are:

$$a_{S,centr,r}[1] = -(\sin(\psi) p_h + \cos(\psi) q_h)^2 (\cos(\beta) r + e) + (-r_h + \Omega) (-(-\cos(\psi) p_h + \sin(\psi) q_h) \sin(\beta) r + (-r_h + \Omega) (\cos(\beta) r + e))$$

$$a_{S,centr,r}[2] = (-\cos(\psi) p_h + \sin(\psi) q_h) (\sin(\psi) p_h + \cos(\psi) q_h) (\cos(\beta) r + e) + (-r_h + \Omega) (\sin(\psi) p_h + \cos(\psi) q_h) \sin(\beta) r$$

$$a_{S,centr,r}[3] = (-\cos(\psi) p_h + \sin(\psi) q_h) (-(-\cos(\psi) p_h + \sin(\psi) q_h) \sin(\beta) r + (-r_h + \Omega) (\cos(\beta) r + e)) - (\sin(\psi) p_h + \cos(\psi) q_h)^2 \sin(\beta) r$$

5. Coriolis acceleration:

$$a_{S,Cor,r} = 2\omega_r \times V_{S,rel,r} = \begin{bmatrix} (2 \sin(\psi) p_h + 2 \cos(\psi) q_h) \cos(\beta) \dot{\beta} r \\ -(-2 \cos(\psi) p_h + 2 \sin(\psi) q_h) \cos(\beta) \dot{\beta} r - (-2 r_h + 2 \Omega) \sin(\beta) \dot{\beta} r \\ (2 \sin(\psi) p_h + 2 \cos(\psi) q_h) \sin(\beta) \dot{\beta} r \end{bmatrix}$$

The resulting total blade section acceleration in the Rotating system is:

$$a_{S_r} = a_{S,rel,r} + a_r + a_{S,tang,r} + a_{S,centr,r} + a_{S,Cor,r}$$

$$a_{S_r}[1] = -\cos(\beta) \dot{\beta}^2 r - \sin(\beta) \ddot{\beta} r - \cos(\psi) \dot{u}_h + \sin(\psi) \dot{v}_h + (\sin(\psi) \dot{p}_h + \cos(\psi) \dot{q}_h) \sin(\beta) r - (\sin(\psi) p_h + \cos(\psi) q_h)^2 (\cos(\beta) r + e) + (-r_h + \Omega) (-(-\cos(\psi) p_h + \sin(\psi) q_h) \sin(\beta) r + (-r_h + \Omega) (\cos(\beta) r + e)) + (2 \sin(\psi) p_h + 2 \cos(\psi) q_h) \cos(\beta) \dot{\beta} r$$

$$a_{S_r}[2] = \sin(\psi) \dot{u}_h + \cos(\psi) \dot{v}_h - (-\cos(\psi) \dot{p}_h + \sin(\psi) \dot{q}_h) \sin(\beta) r + (-\dot{r}_h + \dot{\Omega}) (\cos(\beta) r + e) + (-\cos(\psi) p_h + \sin(\psi) q_h) (\sin(\psi) p_h + \cos(\psi) q_h) (\cos(\beta) r + e) + (-r_h + \Omega) (\sin(\psi) p_h + \cos(\psi) q_h) \sin(\beta) r + (-2 \cos(\psi) p_h + 2 \sin(\psi) q_h) \cos(\beta) \dot{\beta} r - (-2 r_h + 2 \Omega) \sin(\beta) \dot{\beta} r$$

$$\begin{aligned}
a_{S,r}[3] = & -\sin(\beta)\dot{\beta}^2 r + \cos(\beta)\ddot{\beta}r - \dot{w}_h - (\sin(\psi)\dot{p}_h + \cos(\psi)\dot{q}_h)(\cos(\beta)r + e) + \\
& + (-\cos(\psi)p_h + \sin(\psi)q_h) \left( -(-\cos(\psi)p_h + \sin(\psi)q_h)\sin(\beta)r + \right. \\
& \left. + (-r_h + \Omega)(\cos(\beta)r + e) \right) - (\sin(\psi)p_h + \cos(\psi)q_h)^2 \sin(\beta)r + \\
& + (2\sin(\psi)p_h + 2\cos(\psi)q_h)\sin(\beta)\dot{\beta}r
\end{aligned}$$

Total acceleration in the Hub and Blade reference frames can be computed, respectively, as:

$$a_{S,h} = T_\psi \cdot a_{S,r}$$

$$a_{S,b} = T_\beta^{-1} \cdot a_{S,r}$$

For implementation in the flapping dynamics equation, the component of  $a_{S,b}$  directed along the  $z_b$  axis is computed in the blade center of gravity ( $r = r_{cg}$ ) and linearized as:

$$a_{cg,b}[3] = r_{cg}\ddot{\beta} + a_{z2}\beta + a_{z3} \quad (\text{A.1})$$

with:

$$\begin{aligned}
a_{z2} = & -r_{cg} \left( (p_h^2 - q_h^2) (\cos(\psi))^2 - 2\sin(\psi)p_h q_h \cos(\psi) + (q_h + r_h - \Omega)(q_h - r_h + \Omega) \right) + \\
& + (-p_h^2 + q_h^2) e (\cos(\psi))^2 + (2e\sin(\psi)p_h q_h + \dot{u}_h) \cos(\psi) - \dot{v}_h \sin(\psi) + e (p_h^2 + (r_h - \Omega)^2)
\end{aligned}$$

$$\begin{aligned}
a_{z3} = & 2r_{cg}(r_h - \Omega)(\cos(\psi)p_h - \sin(\psi)q_h) - e((-r_h + 2\Omega)p_h + \dot{q}_h)\cos(\psi) + \\
& - ((r_h - 2\Omega)q_h + \dot{p}_h)e\sin(\psi) - \dot{w}_h - r_{cg}((p_h r_h + \dot{q}_h)\cos(\psi) + (-q_h r_h + \dot{p}_h)\sin(\psi))
\end{aligned}$$

## A.2 Blade aerodynamics

### A.2.1 Angle of attack

The inflow angle of a generic blade section is defined as:

$$\phi = \arctan \frac{V_\perp}{V_\parallel}$$

where:

$$V_\parallel = V_{S,b}[2]$$

$$V_\perp = V_{S,b}[3] + V_{inflow} + V_{pitch\ dyn}$$

$$V_{inflow} = \Omega R \left( \lambda_0 + \frac{r}{R} \lambda_{1c} \cos \psi - \frac{r}{R} \lambda_{1s} \sin \psi \right)$$

$$V_{pitch\ dyn} = x_{uo} \dot{\vartheta}_{pitch}$$

$$x_{uo} = 0.25c$$

$$\vartheta_{pitch} = \vartheta_0 - A_1 \cos \psi - B_1 \sin \psi$$

By operating the linearization described in Section 3.1.2, the following inflow angle is obtained:

$$\phi = \phi_1 \dot{\beta} + \phi_2 \beta + \phi_3$$

where:

$$\begin{aligned}\phi_1 &= \frac{n_1 d_3}{n_3^2 + d_3^2} \\ \phi_2 &= \frac{n_2 d_3 - n_3 d_2}{n_3^2 + d_3^2} \\ \phi_3 &= \arctan \frac{n_3}{d_3}\end{aligned}$$

$$\begin{aligned}n_1 &= -r \\ n_2 &= u_h \cos(\psi) + v_h \sin(\psi) \\ n_3 &= (eq_h + (-B_1 x_{uo} - r\lambda_{1c})\Omega + q_h r) \cos(\psi) + \\ &\quad + (ep_h + (A_1 x_{uo} - r\lambda_{1s})\Omega + p_h r) \sin(\psi) - \Omega R\lambda_0 + w_h \\ d_2 &= r(\cos(\psi)p_h - \sin(\psi)q_h) \\ d_3 &= r(-r_h + \Omega) + \cos(\psi)v_h + \sin(\psi)u_h + (-r_h + \Omega)e\end{aligned}$$

The angle of attack of the generic blade section is therefore:

$$\alpha = \alpha_1 \dot{\beta} + \alpha_2 \beta + \alpha_3$$

with:

$$\begin{aligned}\alpha_1 &= \phi_1 \\ \alpha_2 &= -K_1 + \phi_2 \\ \alpha_3 &= \vartheta_{\text{twist}} + \vartheta_0 - A_1 \cos \psi - B_1 \sin \psi - \alpha_0 + \phi_3\end{aligned}$$

### A.2.2 Aerodynamic forces and moments

The aerodynamic forces and moments generated by a generic blade section are:

- aerodynamic force along  $z_b$ :

$$df_a = dd \sin \phi + dl \cos \phi = \frac{1}{2} \rho V^2 c (C_d \sin \phi + C_l \cos \phi) dr$$

- aerodynamic force along  $-y_b$ :

$$dq_a = dd \cos \phi - dl \sin \phi = \frac{1}{2} \rho V^2 c (C_d \cos \phi - C_l \sin \phi) dr$$

- aerodynamic moment around  $-y_b$ :

$$dm_a = df_a r = \frac{1}{2} \rho V^2 c (C_d \sin \phi + C_l \cos \phi) r dr$$

- aerodynamic moment  $-z_b$ :

$$dn_a = dq_a r = \frac{1}{2} \rho V^2 c (C_d \cos \phi - C_l \sin \phi) r dr$$

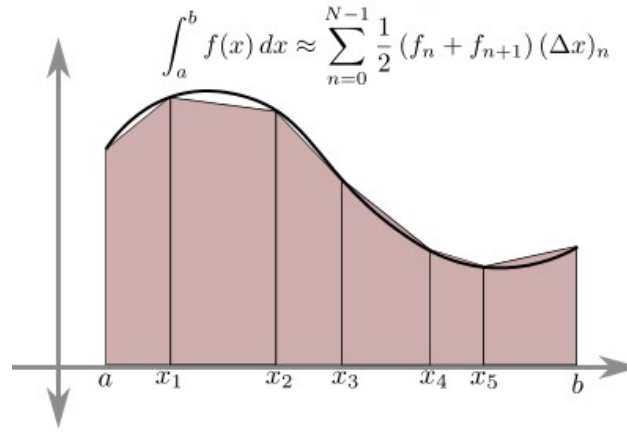


**Figure A.1:** Integration using the method of the trapezoids

where  $V = \sqrt{V_{\perp}^2 + V_{\parallel}^2}$ .

For implementation in the flapping dynamics equation, the moment  $m_a$  is linearized as follows:

$$dm_a = dm_1 \dot{\beta} + dm_2 \beta + dm_3$$

with:

$$\begin{aligned} dm_1 &= \frac{1}{2} \rho V^2 c (C_{d\alpha}(\alpha_3) \sin \phi + C_{l\alpha}(\alpha_3) \cos \phi) \alpha_1 r dr \\ dm_2 &= \frac{1}{2} \rho V^2 c (C_{d\alpha}(\alpha_3) \sin \phi + C_{l\alpha}(\alpha_3) \cos \phi) \alpha_2 r dr \\ dm_3 &= \frac{1}{2} \rho V^2 c (C_d(\alpha_3) \sin \phi + C_l(\alpha_3) \cos \phi) r dr \end{aligned}$$

The overall aerodynamic loads generated by each blade are obtained by integrating the above forces and moments along the whole length of the blade:

$$\begin{aligned} F_a &= \int_0^R df_a dr & Q_a &= \int_0^R dq_a dr \\ M_a &= \int_0^R dm_a dr & N_a &= \int_0^R dn_a dr \end{aligned}$$

$$M_1 = \int_0^R dm_1 dr \quad M_2 = \int_0^R dm_2 dr \quad M_3 = \int_0^R dm_3 dr \quad (\text{A.2})$$

Integration along the blade is operated symbolically, using the method of the trapezoids (Figure A.1). Let  $df$  be a generic aerodynamic load generated by a blade section, and  $n$  the number of intervals in which the blade has been divided; the length of each interval is designated as  $\Delta x$ . The overall aerodynamic load generated by the blade is then:

$$F = \int_0^R df \approx \frac{\Delta x}{2} (df(x_1) + 2df(x_2) + 2df(x_3) + \dots + 2df(x_n) + df(x_{n+1}))$$

### A.3 Gimballed rotor flapping dynamics

Flapping dynamics equation for a gimballed rotor:

$$\mathbf{M}\ddot{\boldsymbol{\beta}} + \mathbf{C}\dot{\boldsymbol{\beta}} + \mathbf{K}\boldsymbol{\beta} = \mathbf{F}_\beta \quad (\text{A.3})$$

Mass matrix:

$$\mathbf{M} = I_\beta \mathbf{I}$$

where  $\mathbf{I}$  is the identity matrix.

Damping matrix:

$$\mathbf{C} = \mathbf{C}_a + c_{\text{struct}}(\mathbf{I} - \mathbf{B}_\psi)$$

with:

$$\mathbf{B}_\psi = \frac{2}{N} \begin{bmatrix} 1 & \cos(\beta_2 - \beta_1) & \dots & \cos(\beta_N - \beta_1) \\ \cos(\beta_1 - \beta_2) & 1 & \dots & \cos(\beta_N - \beta_2) \\ \vdots & \vdots & \ddots & \vdots \\ \cos(\beta_1 - \beta_N) & \cos(\beta_2 - \beta_N) & \dots & 1 \end{bmatrix}$$

$$\mathbf{C}_a = \begin{bmatrix} C_{a_1} & 0 & \dots & 0 \\ 0 & C_{a_2} & \dots & 0 \\ \vdots & \vdots & \ddots & \vdots \\ 0 & 0 & \dots & C_{a_N} \end{bmatrix} \quad C_{a_j} = -M_{1_j}$$

Stiffness matrix:

$$\mathbf{K} = \mathbf{K}_a + k_\beta \mathbf{I} - (k_\beta - k_G) \mathbf{B}_\psi$$

with:

$$\mathbf{K}_a = \begin{bmatrix} K_{a_1} & 0 & \dots & 0 \\ 0 & K_{a_2} & \dots & 0 \\ \vdots & \vdots & \ddots & \vdots \\ 0 & 0 & \dots & K_{a_N} \end{bmatrix} \quad K_{a_j} = -M_{2_j} + m_b r_{cg} a_{z2_j}$$

Non-homogeneous term:

$$\mathbf{F}_\beta = \begin{Bmatrix} F_{\beta_1} \\ F_{\beta_2} \\ \vdots \\ F_{\beta_N} \end{Bmatrix} \quad F_{\beta_j} = M_{3_j} - m_b r_{cg} (a_{z3_j} + g_{z_j})$$

Where  $M_{1_j}$ ,  $M_{2_j}$ ,  $M_{3_j}$ ,  $a_{z2_j}$ ,  $M_{z3_j}$  are computed for the  $j$ -th blade using Equations A.2 and A.1, while  $g_{z_j}$  is the gravity acceleration along  $z_b$  for the  $j$ -th blade.

### A.4 Hub loads

By means of the procedure described in Section 3.1.5, the following forces and moments are obtained:

Forces:

$$X_h = \sum_{j=1}^N \left( \cos(\beta_j) \cos(\psi_j) m_b a_{cg,h,j}[1] + \sin(\psi_j) (-m_b a_{cg,h,j}[2] - Q_{a_j}) + \right. \\ \left. + \sin(\beta_j) \cos(\psi_j) (-m_b a_{cg,h,j}[3] + F_{a_j}) + m_b g_h[1] \right)$$

$$Y_h = \sum_{j=1}^N \left( -\cos(\beta_j) \sin(\psi_j) m_b a_{cg,h,j}[1] + \cos(\psi_j) (-m_b a_{cg,h,j}[2] - Q_{a_j}) + \right. \\ \left. - \sin(\beta_j) \sin(\psi_j) (-m_b a_{cg,h,j}[3] + F_{a_j}) + m_b g_h[2] \right)$$

$$Z_h = \sum_{j=1}^N \left( \sin(\beta_j) m_b a_{cg,h,j}[1] - \cos(\beta_j) (-m_b a_{cg,h,j}[3] + F_{a_j}) + m_b g_h[3] \right)$$

Moments:

$$L_h = \sum_{j=1}^N \left( \sin(\psi_j) eZ_{h_j} - \sin(\psi_j) K_\beta \beta_j + \sin(\beta_j) \cos(\psi_j) (-a_{cg,h,j}[2] m_b r_{cg} + \right. \\ \left. - N_{a_j} + r_{cg} m_b (\sin(\psi_j) g_h[1] + \cos(\psi_j) g_h[2])) \right)$$

$$M_h = \sum_{j=1}^N \left( \cos(\psi_j) eZ_{h_j} - \cos(\psi_j) K_\beta \beta_j - \sin(\beta_j) \sin(\psi_j) (-a_{cg,h,j}[2] m_b r_{cg} + \right. \\ \left. - N_{a_j} + r_{cg} m_b (\sin(\psi_j) g_h[1] + \cos(\psi_j) g_h[2])) \right)$$

$$N_h = \sum_{j=1}^N \left( -\cos(\psi_j) eY_{h_j} - \sin(\psi_j) eX_{h_j} - \cos(\beta_j) (-a_{cg,h,j}[2] m_b r_{cg} + \right. \\ \left. - N_{a_j} + r_{cg} m_b (\sin(\psi_j) g_h[1] + \cos(\psi_j) g_h[2])) \right)$$



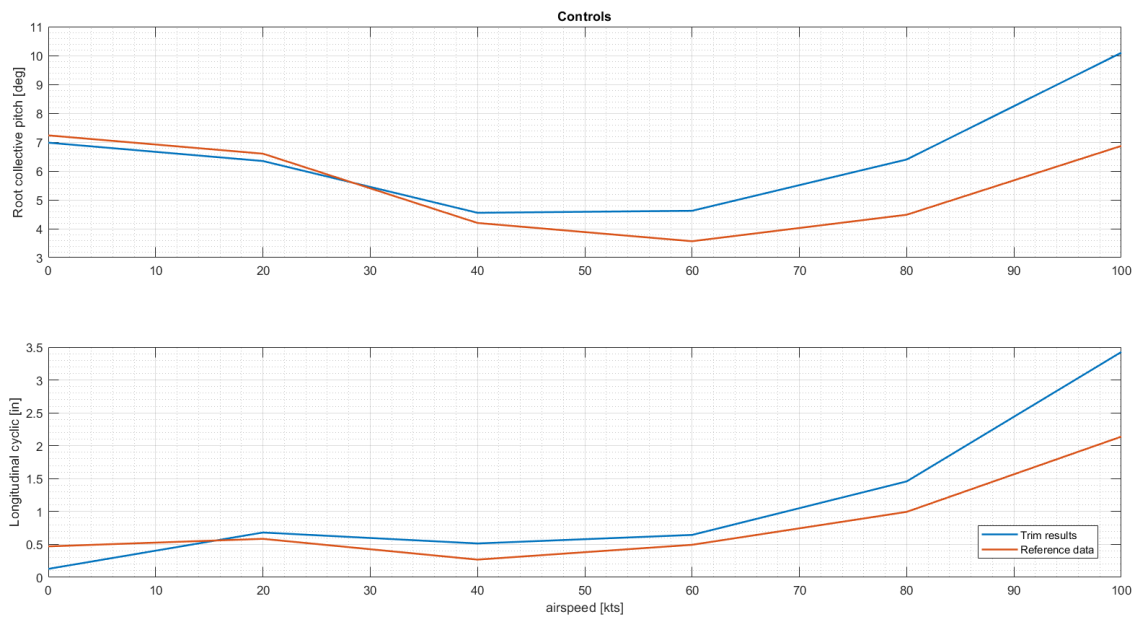
# Appendix B

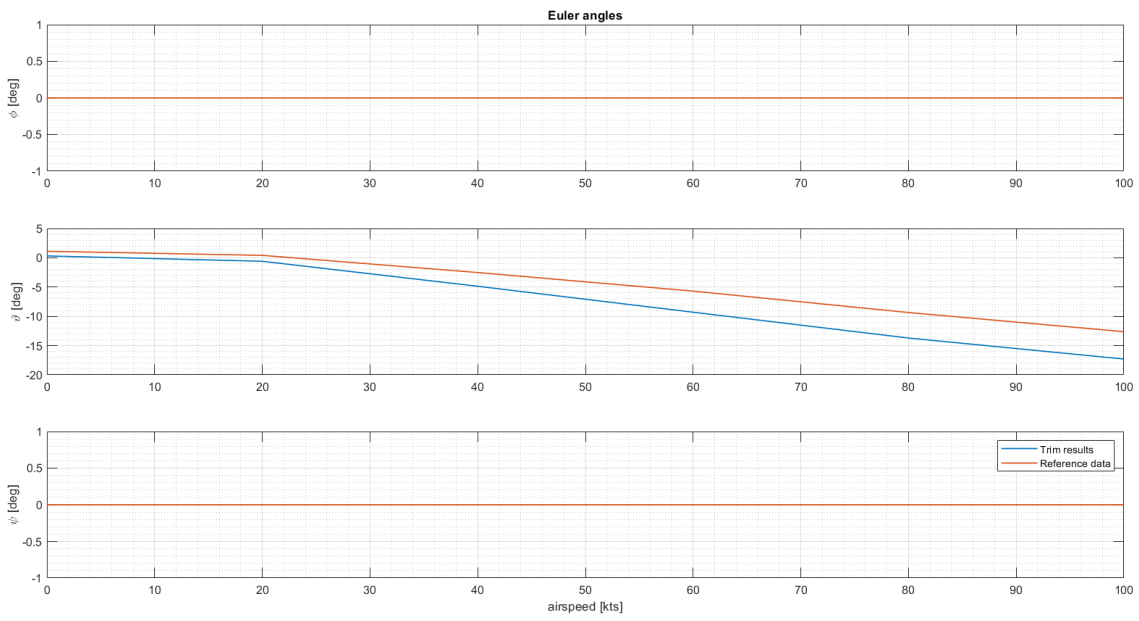
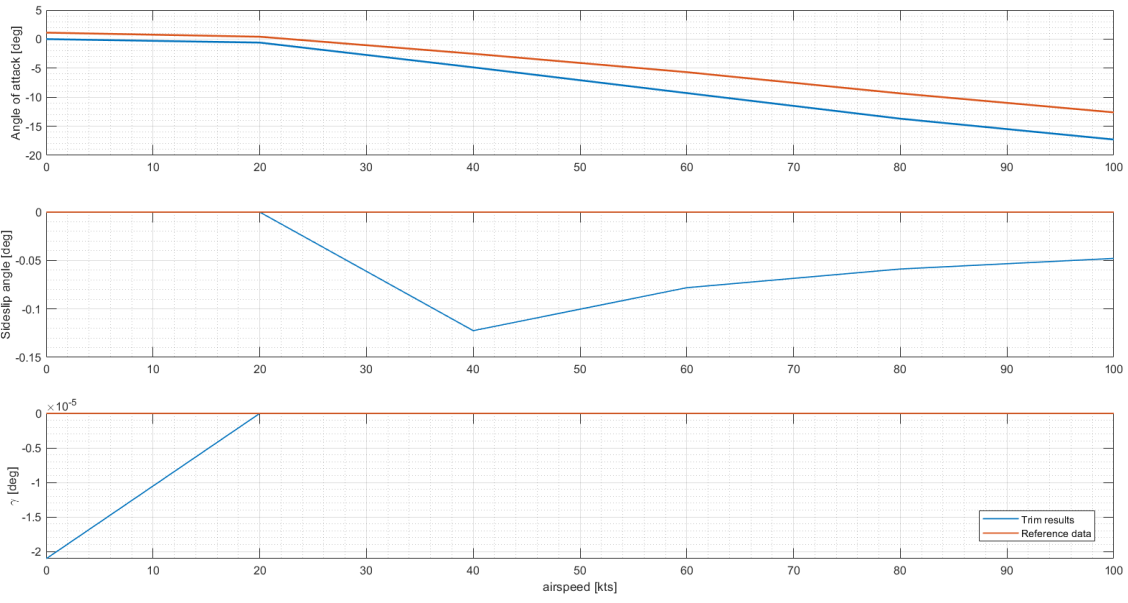
## Trim results

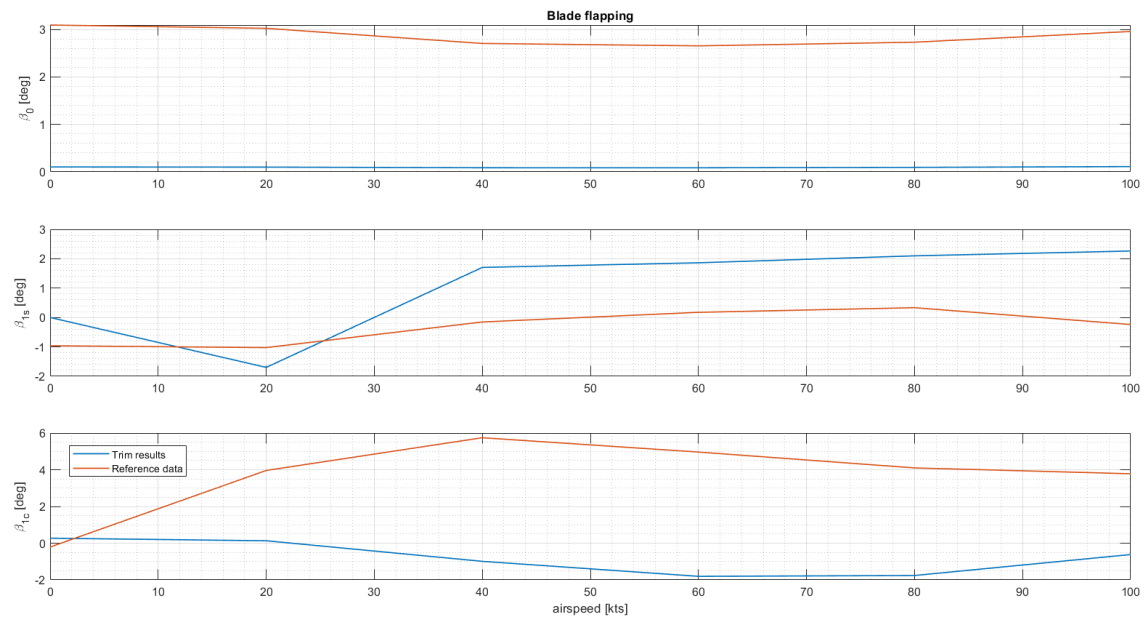
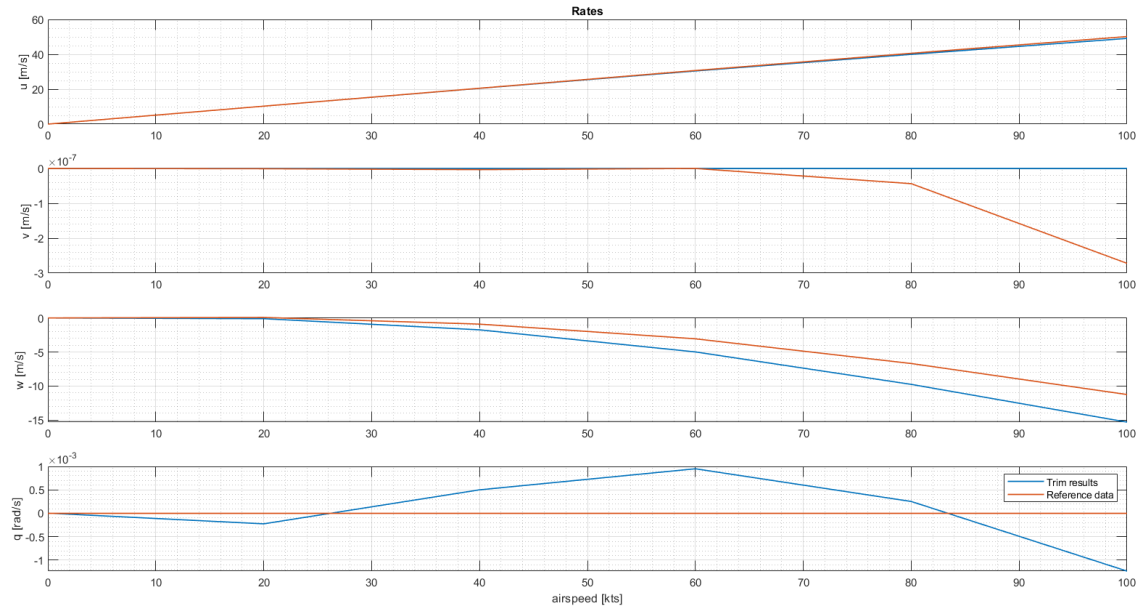
### B.1 Helicopter mode

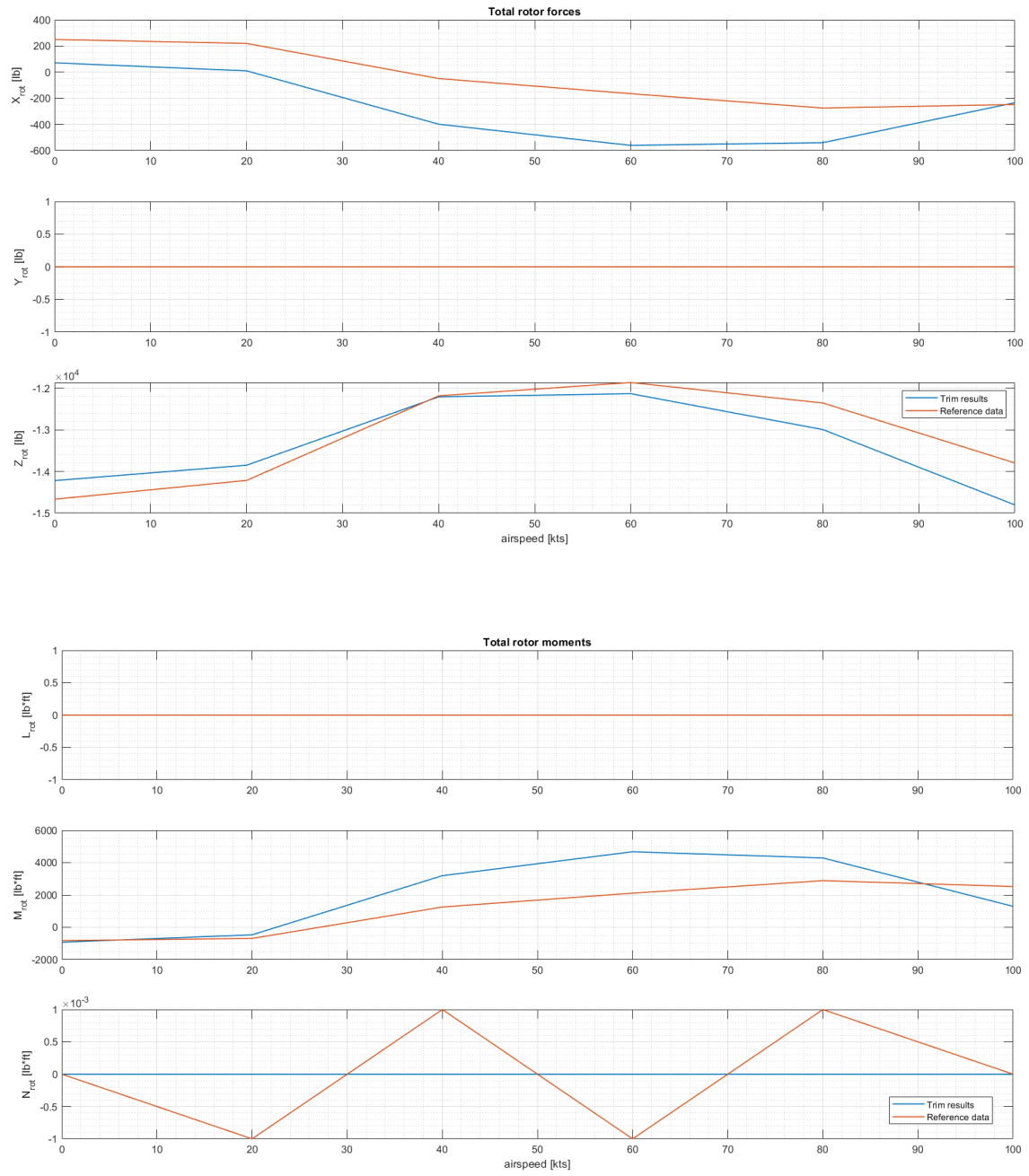
#### Flight conditions

- Nacelle incidence: 90 degrees
- Rotor speed: 589 rpm
- Flap/flaperon position: 40/25 degrees
- Altitude: Sea Level Standard
- Airspeed: 0.01, 20, 40, 60, 80, 100 knots





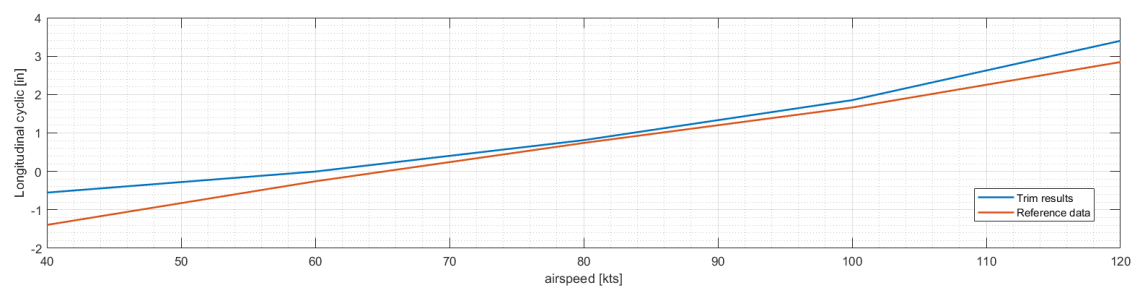
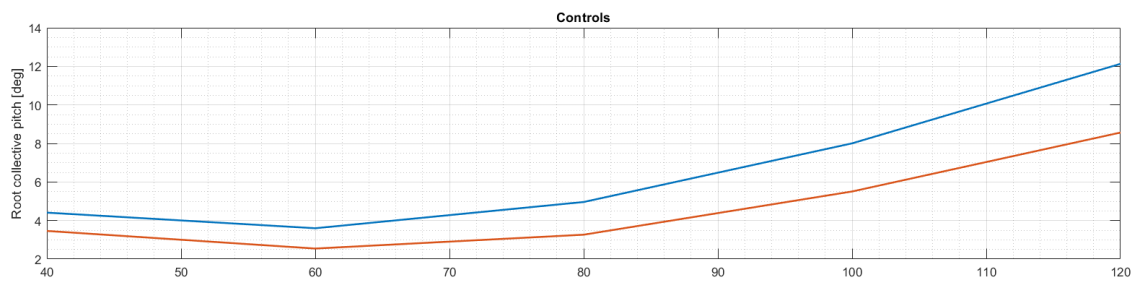


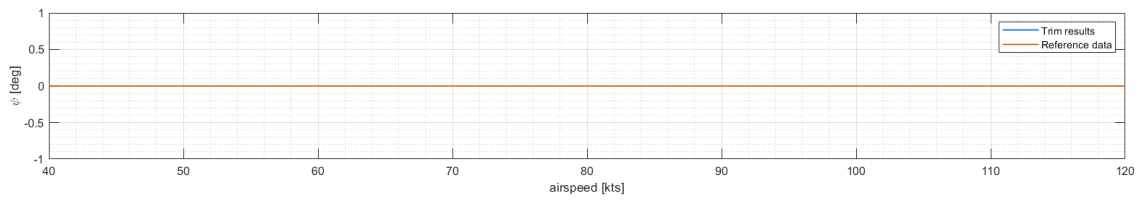
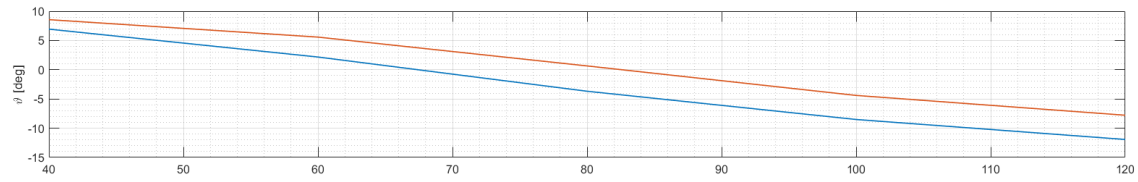
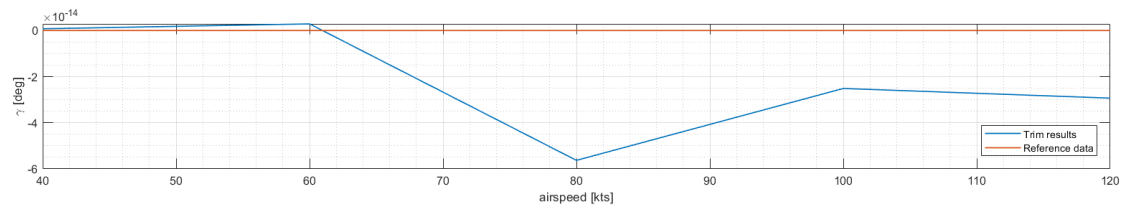
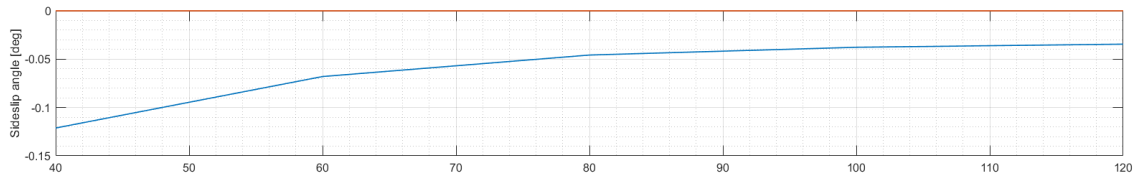
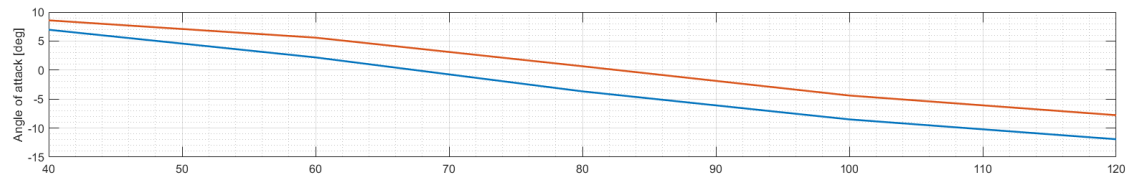


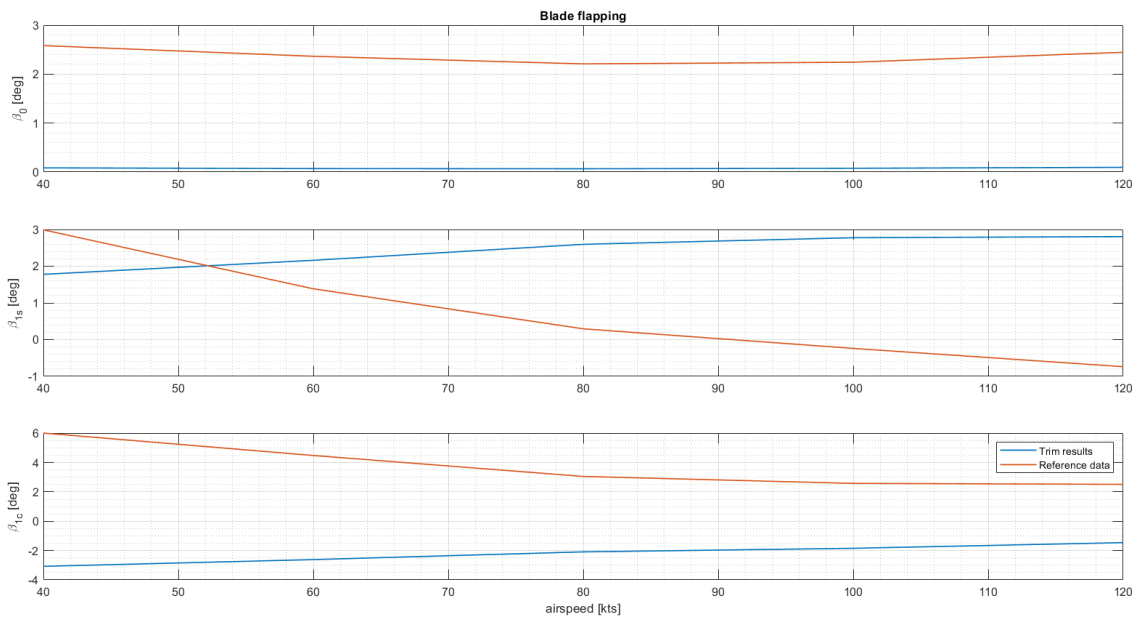
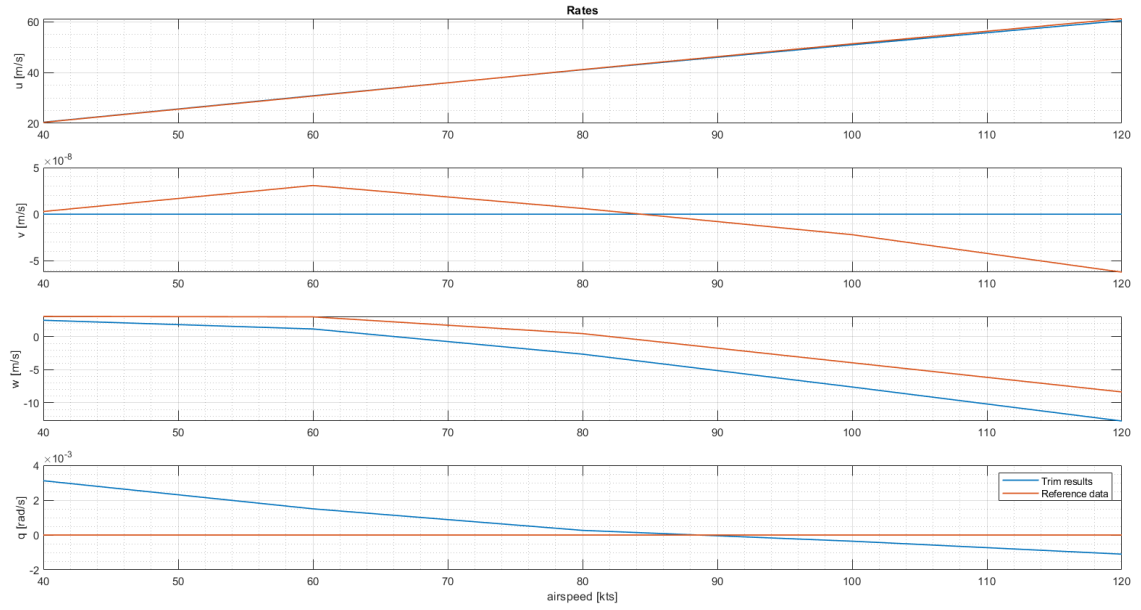
## B.2 Conversion

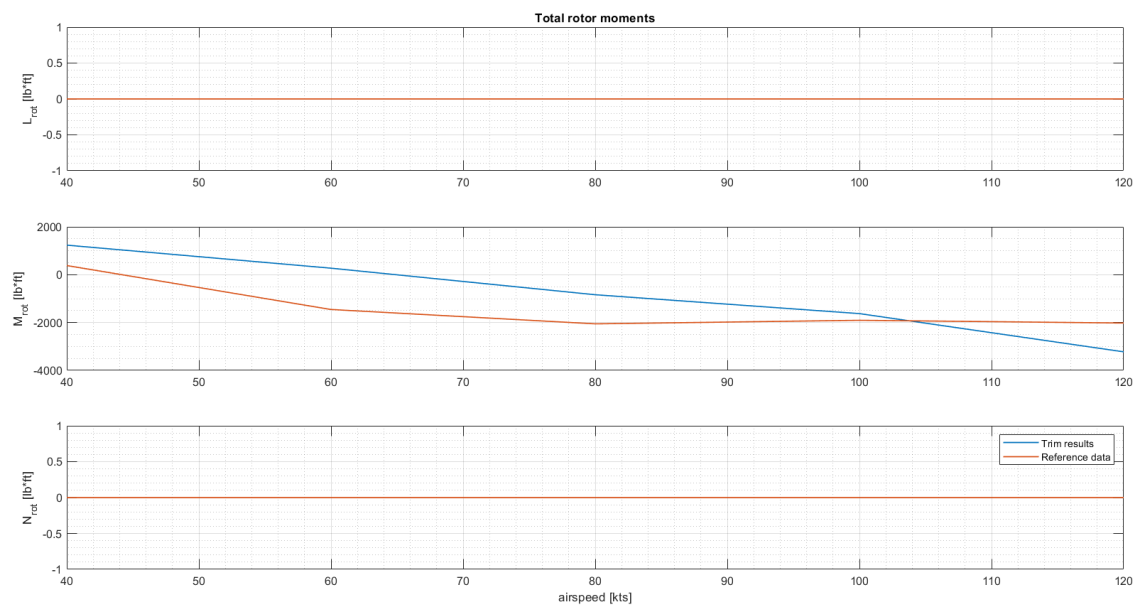
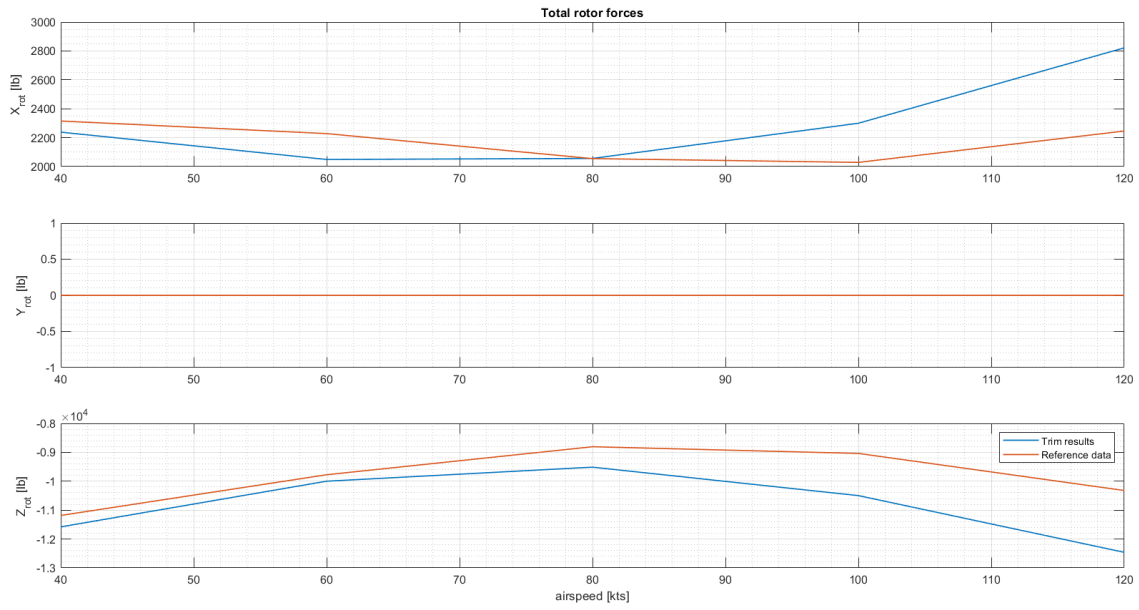
### Flight conditions

- Nacelle incidence: 75 degrees
- Rotor speed: 589 rpm
- Flap/flaperon position: 40/25 degrees
- Altitude: Sea Level Standard
- Airspeed: 40, 60, 80, 100, 120 knots



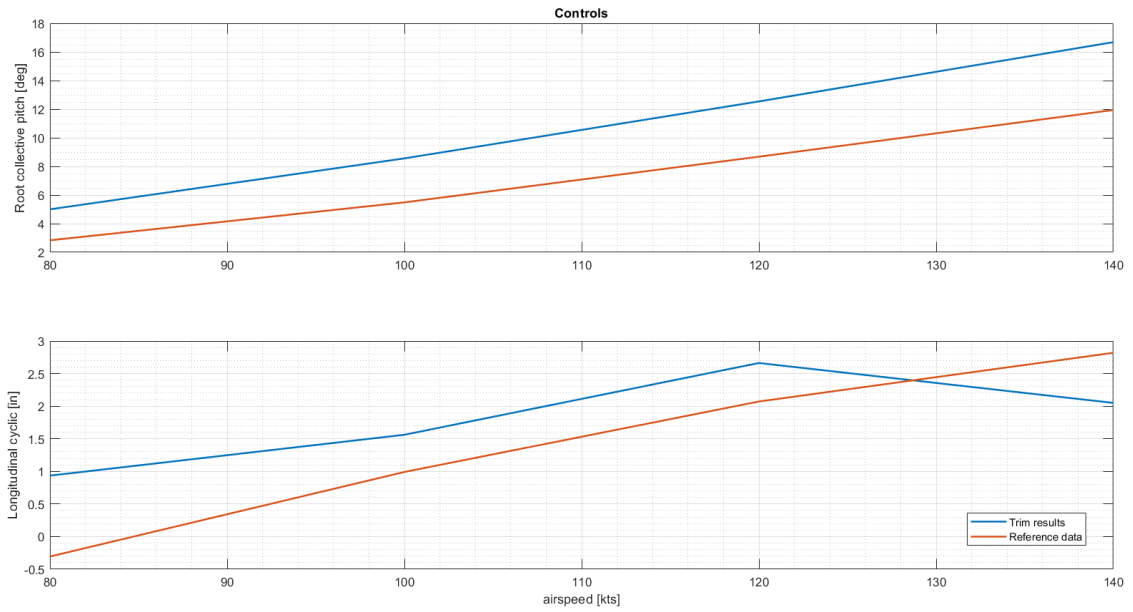


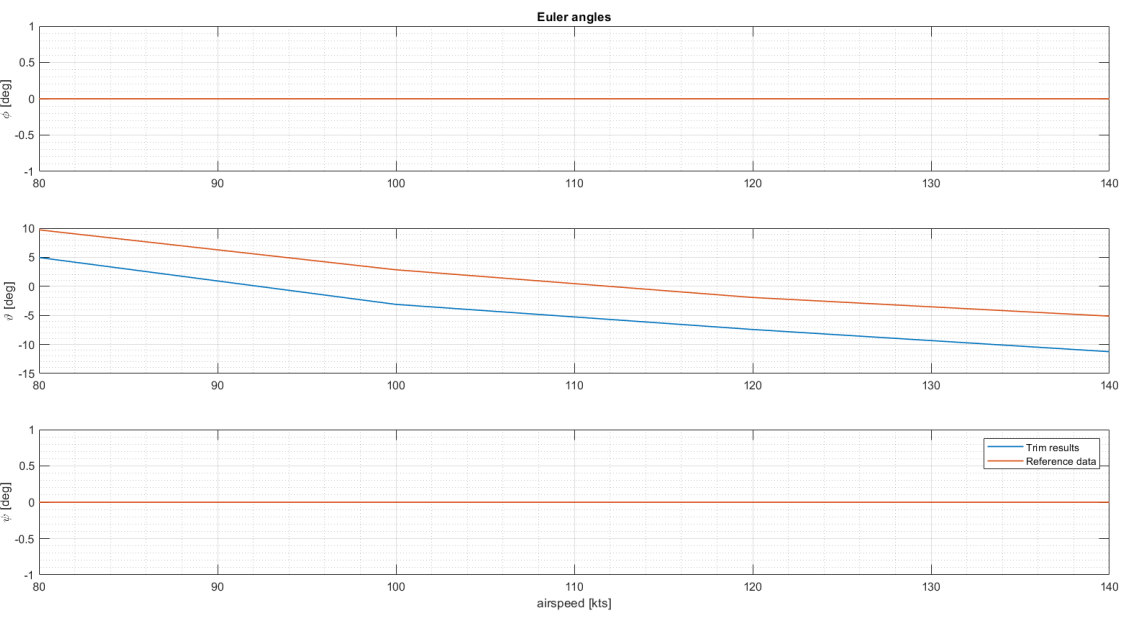
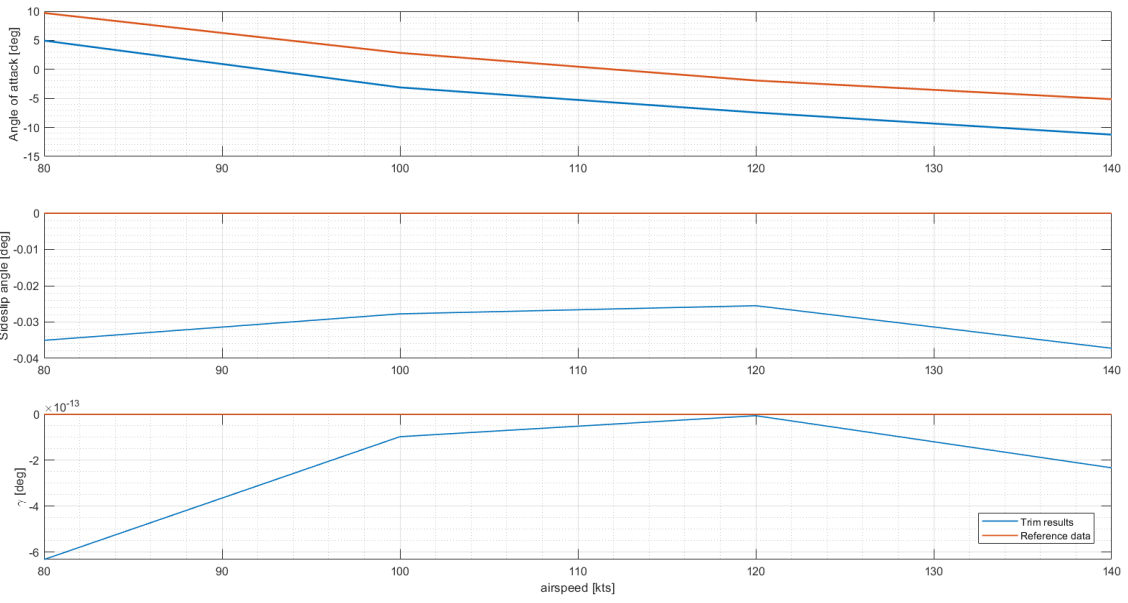


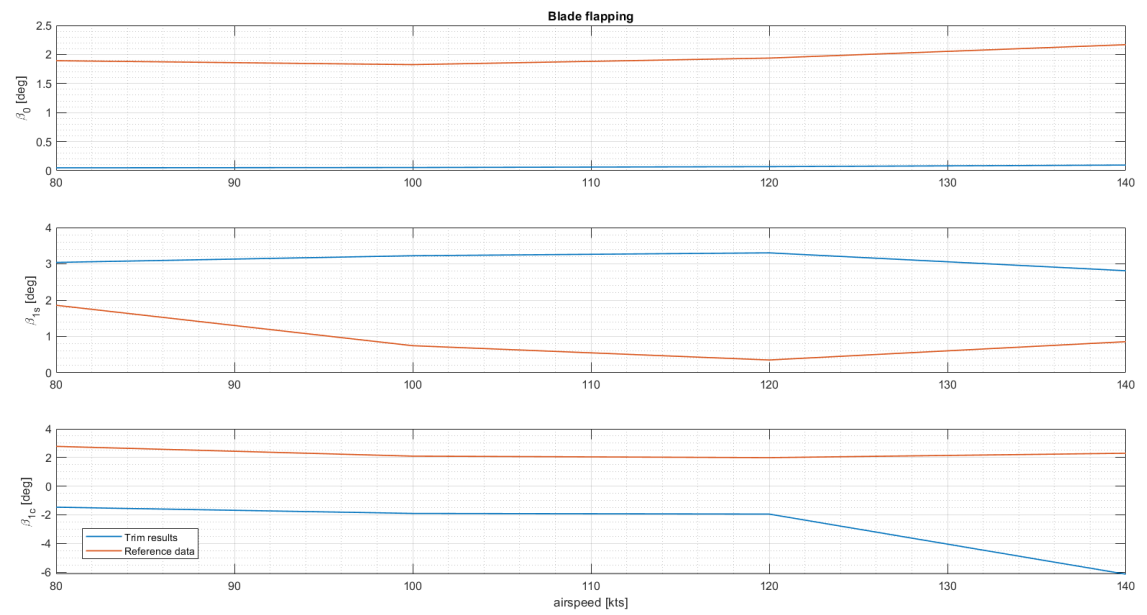
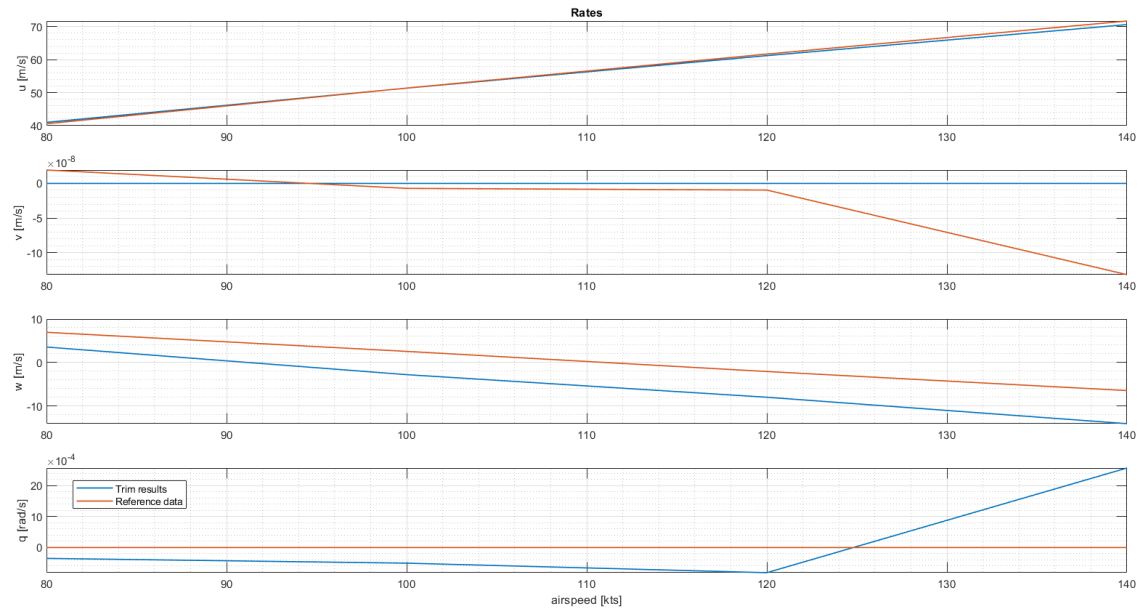


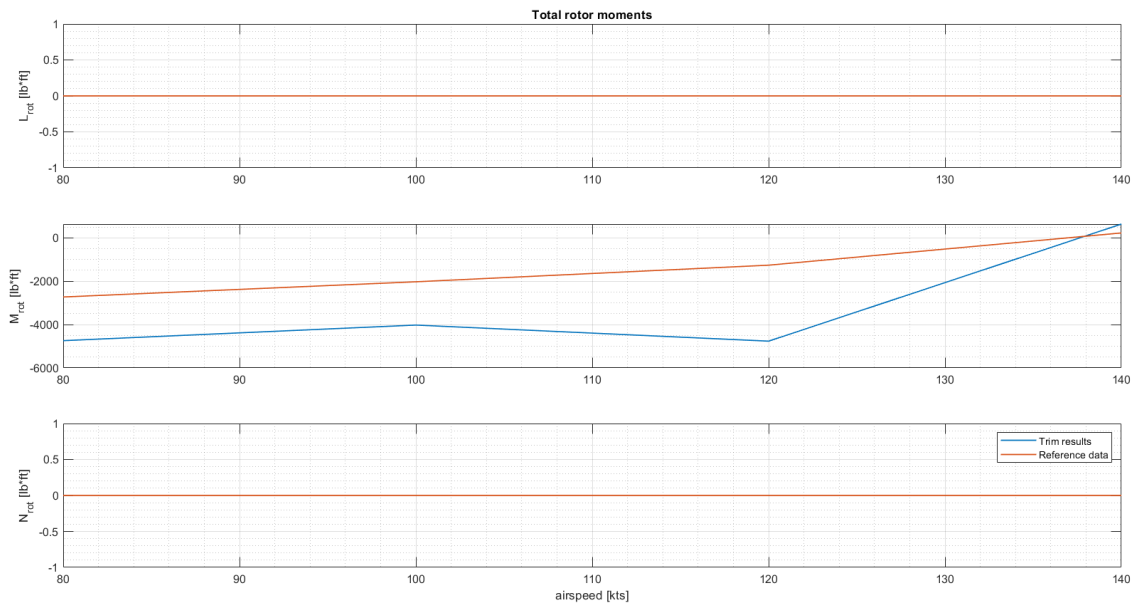
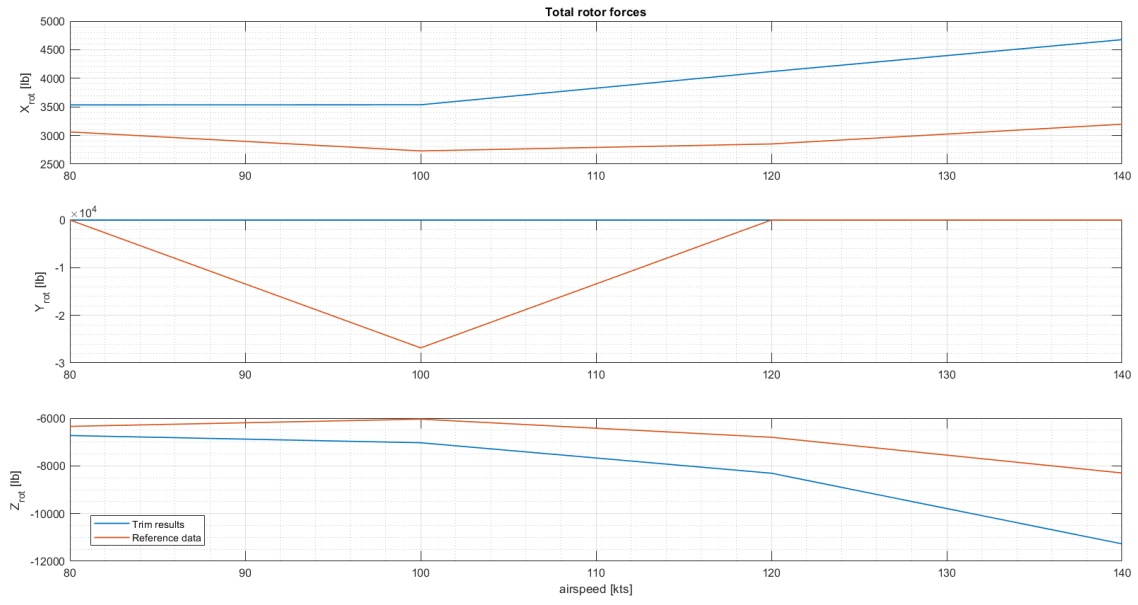
**Flight conditions**

- Nacelle incidence: 60 degrees
- Rotor speed: 589 rpm
- Flap/flaperon position: 20/12.5 degrees
- Altitude: Sea Level Standard
- Airspeed: 80, 100, 120, 140 knots



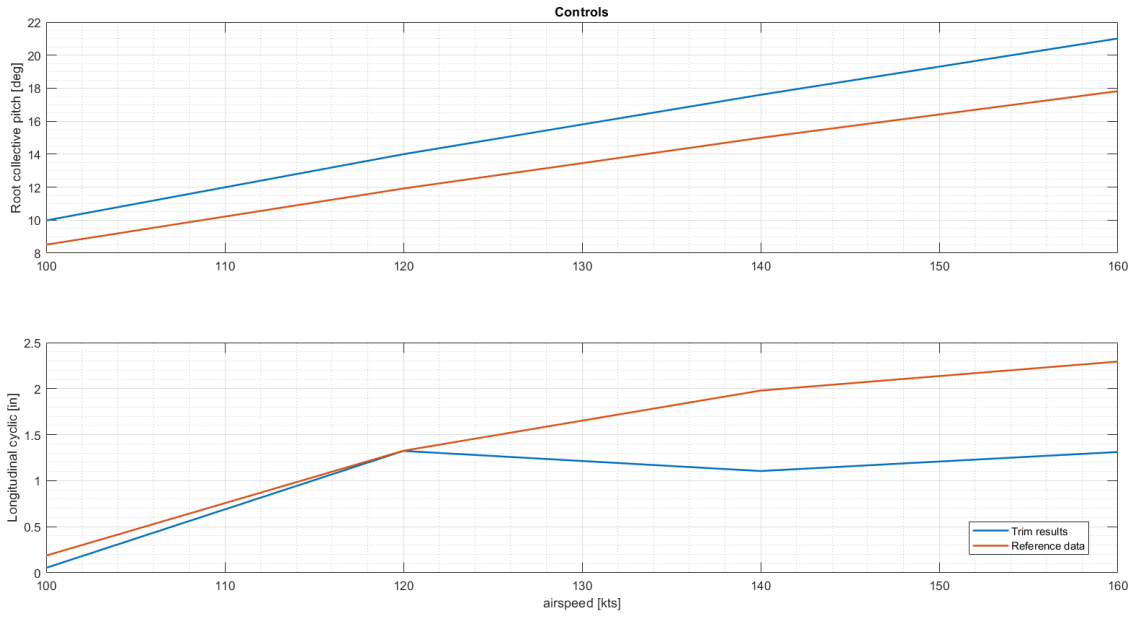


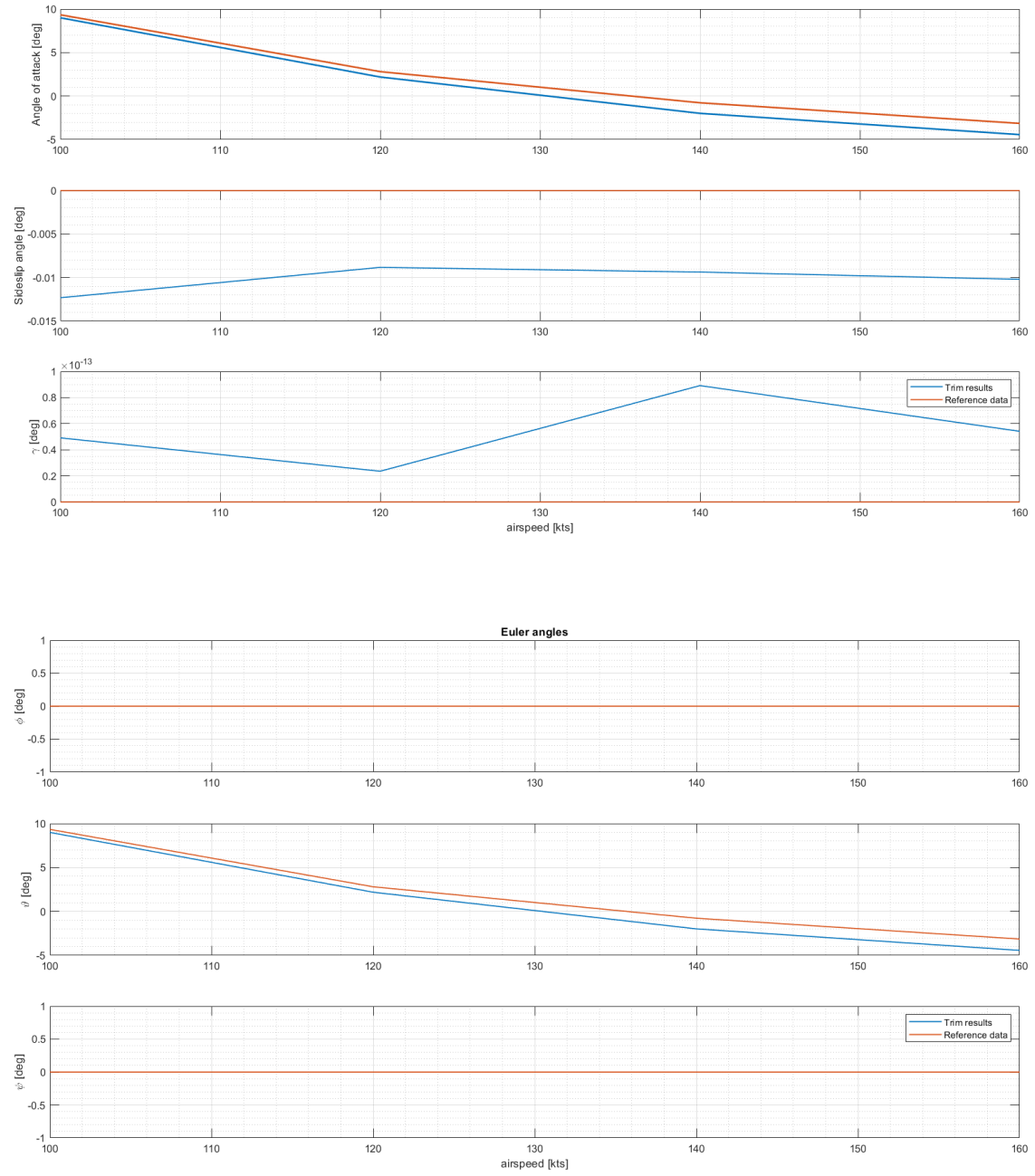


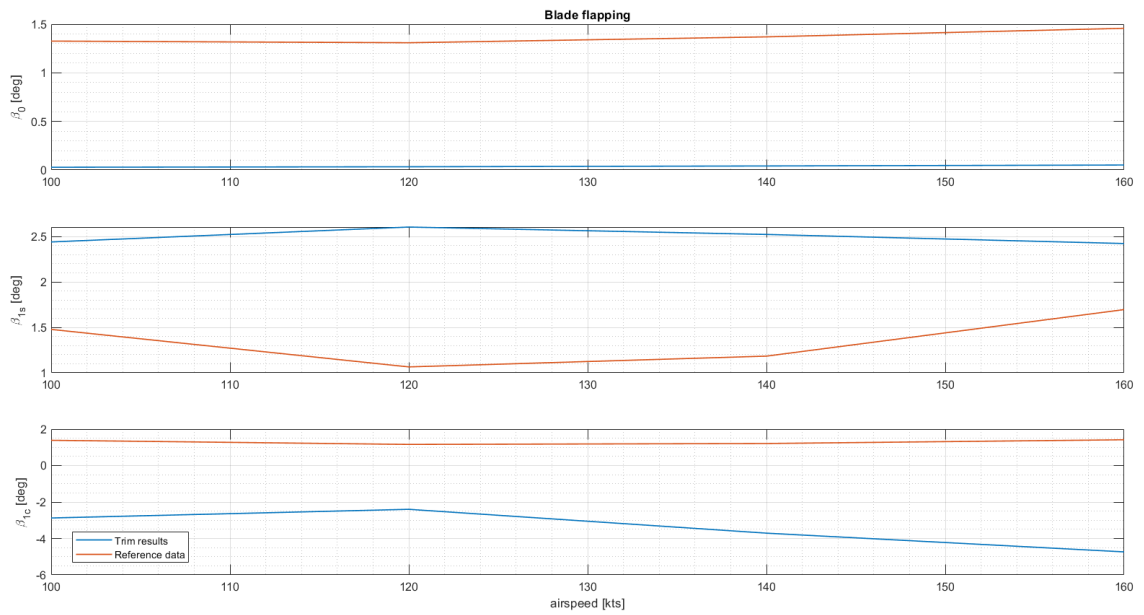
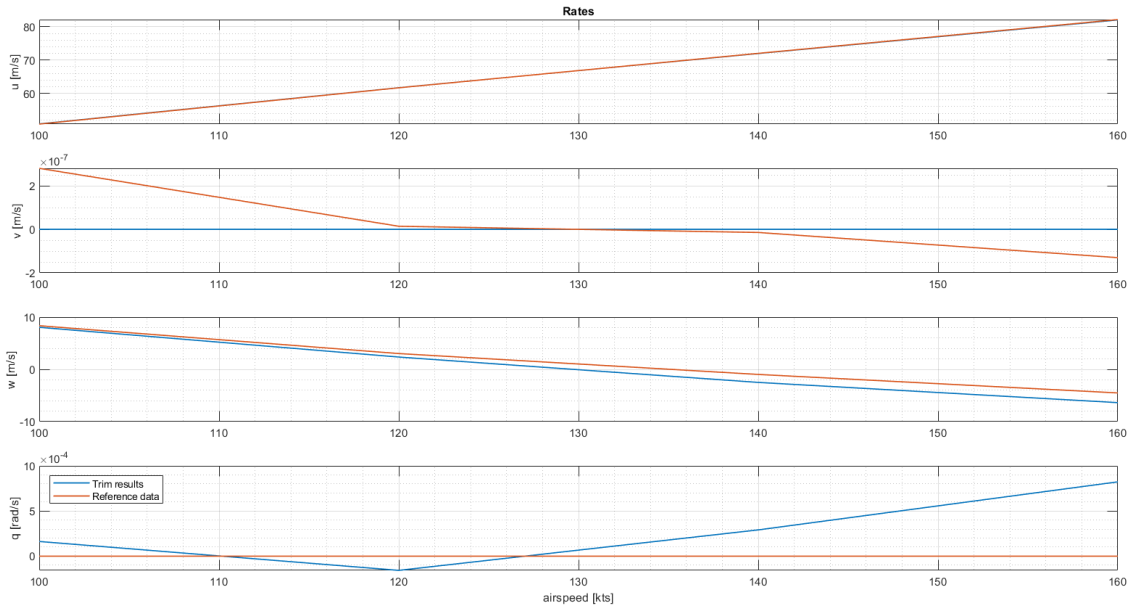


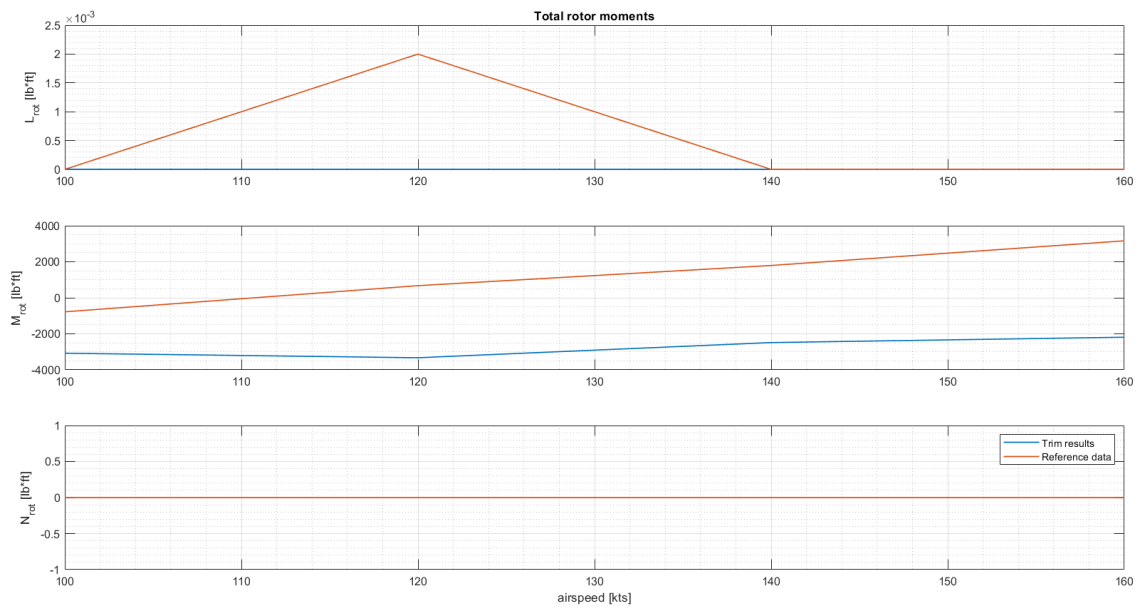
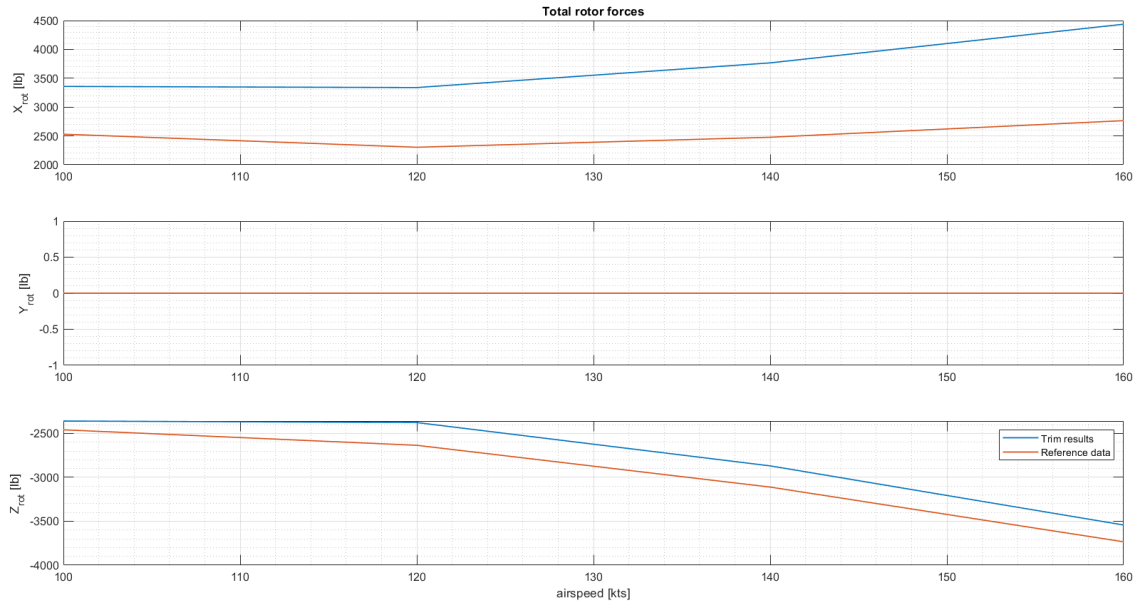
**Flight conditions**

- Nacelle incidence: 30 degrees
- Rotor speed: 589 rpm
- Flap/flaperon position: 20/12.5 degrees
- Altitude: Sea Level Standard
- Airspeed: 100, 120, 140, 160 knots





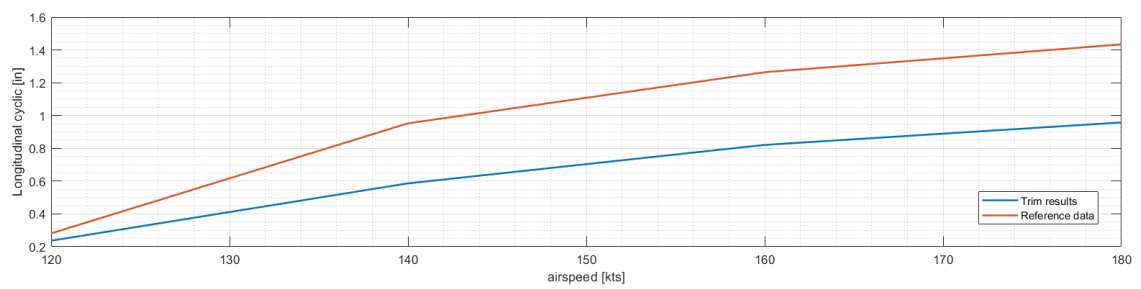
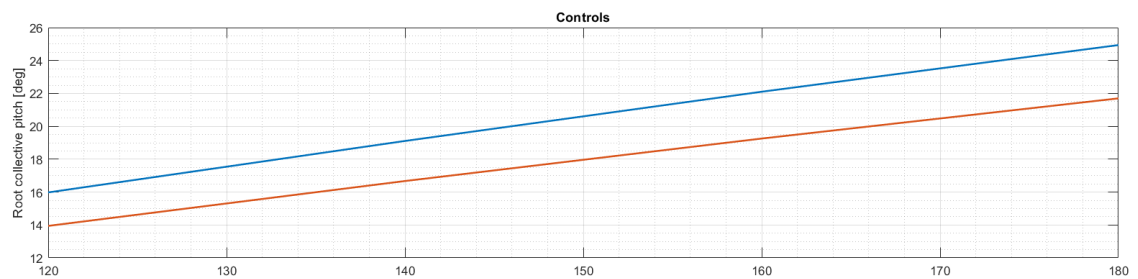


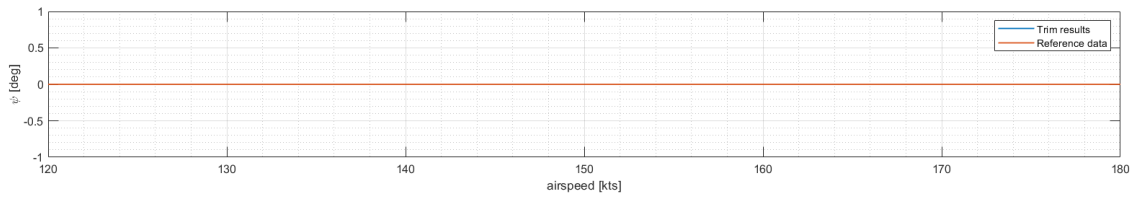
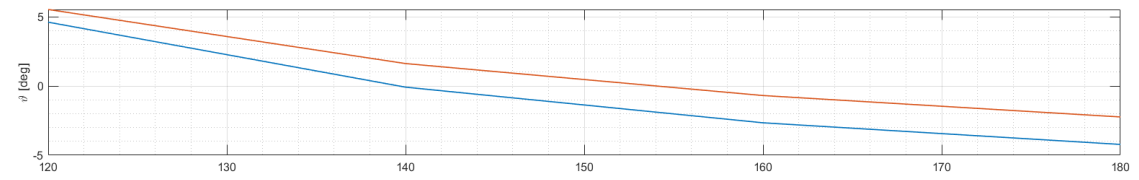
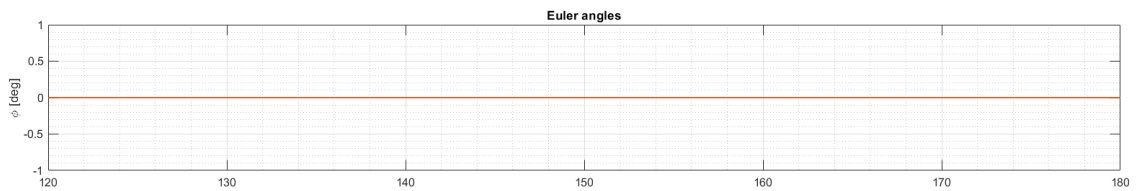
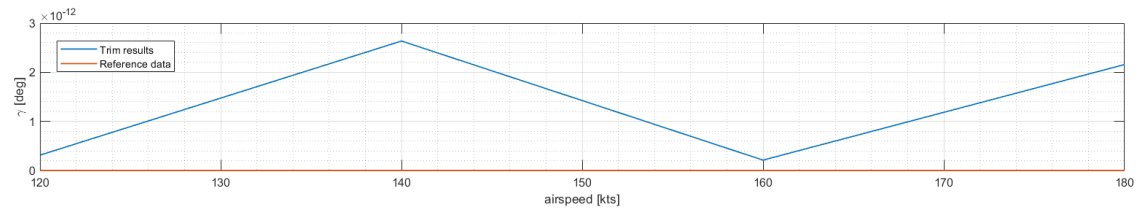
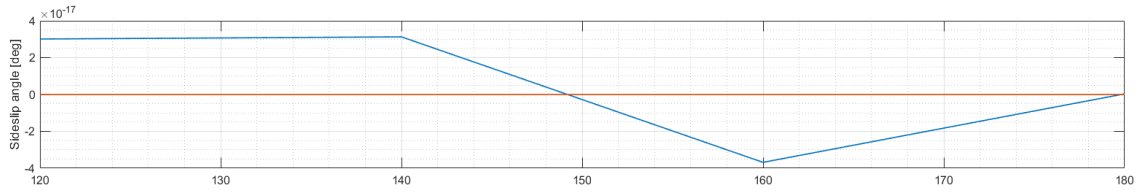
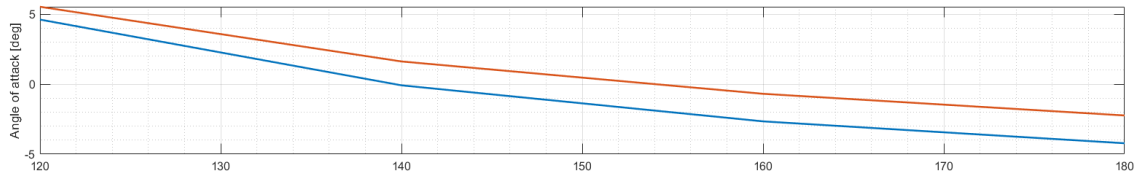


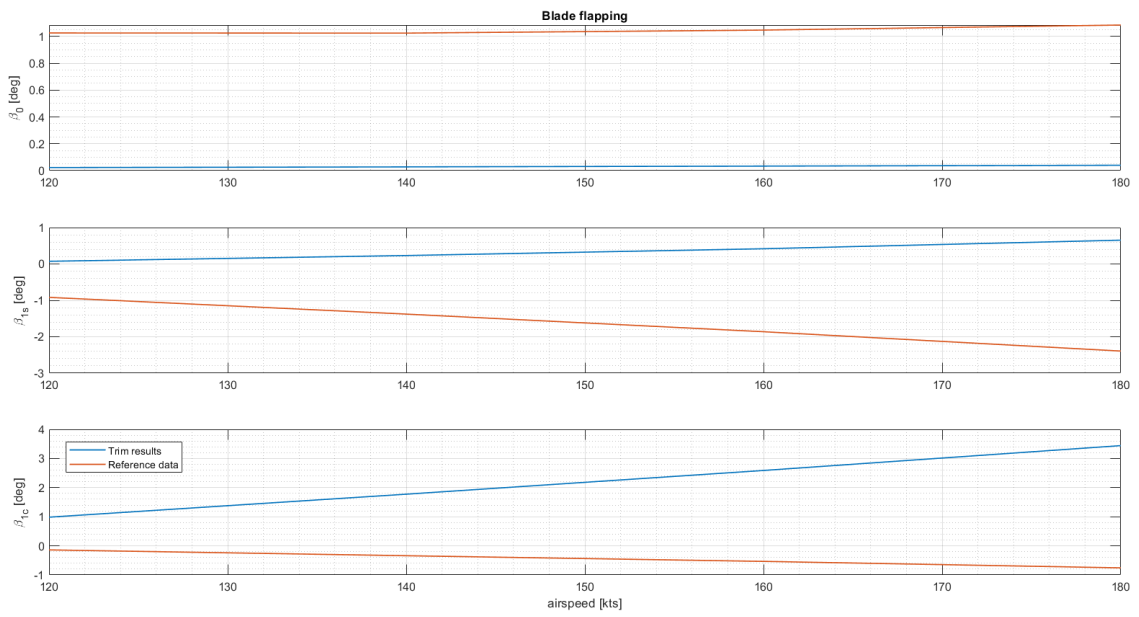
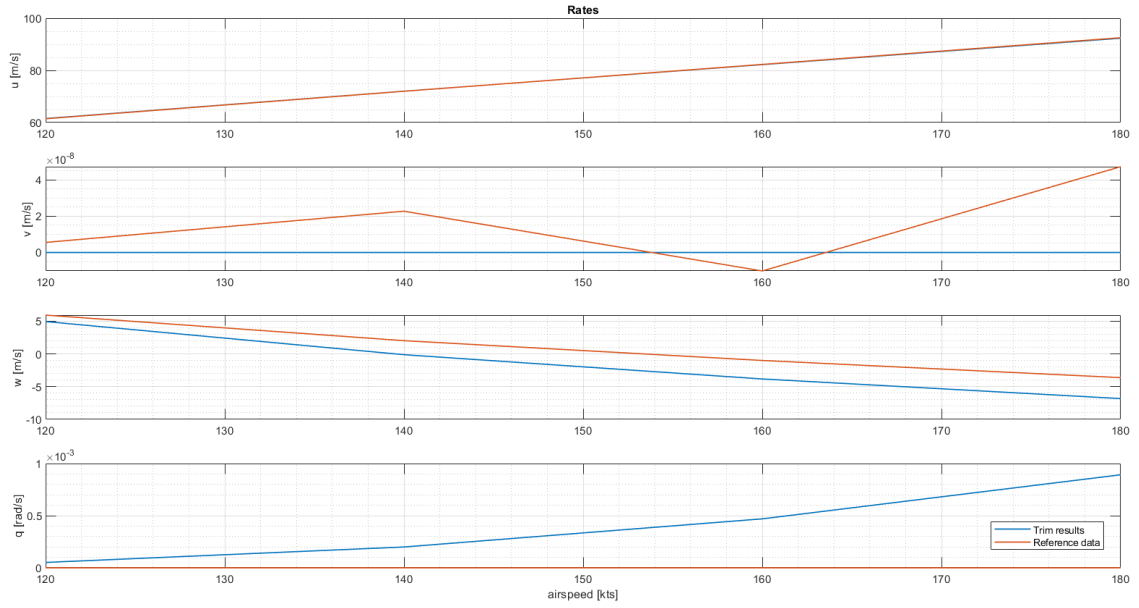
## B.3 Airplane mode

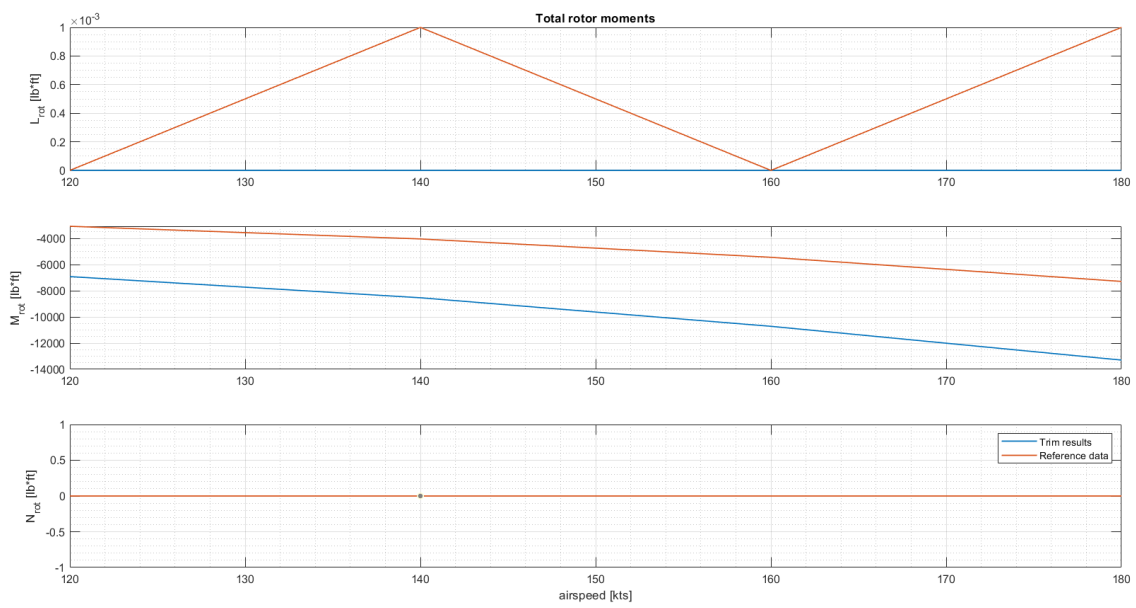
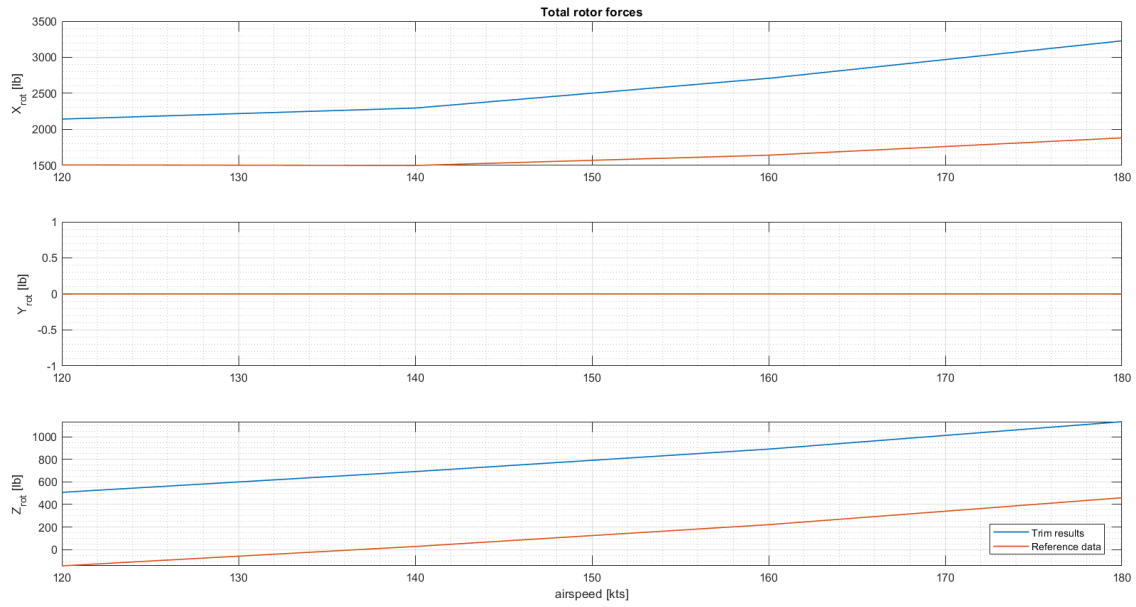
### Flight conditions

- Nacelle incidence: 0 degrees
- Rotor speed: 589 rpm
- Flap/flaperon position: 20/12.5 degrees
- Altitude: Sea Level Standard
- Airspeed: 120, 140, 160, 180 knots



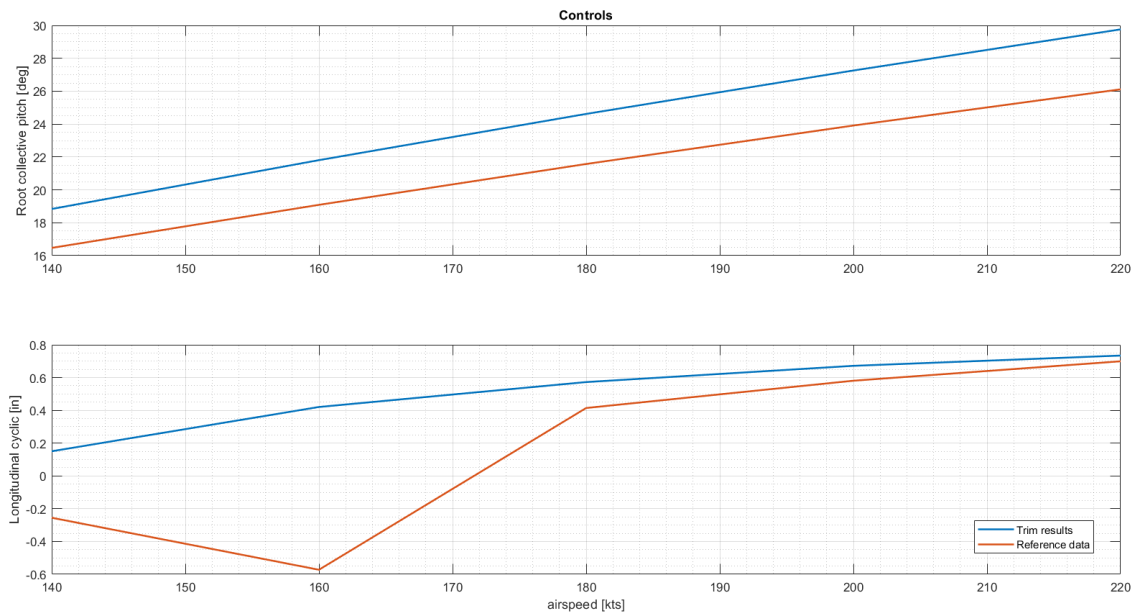


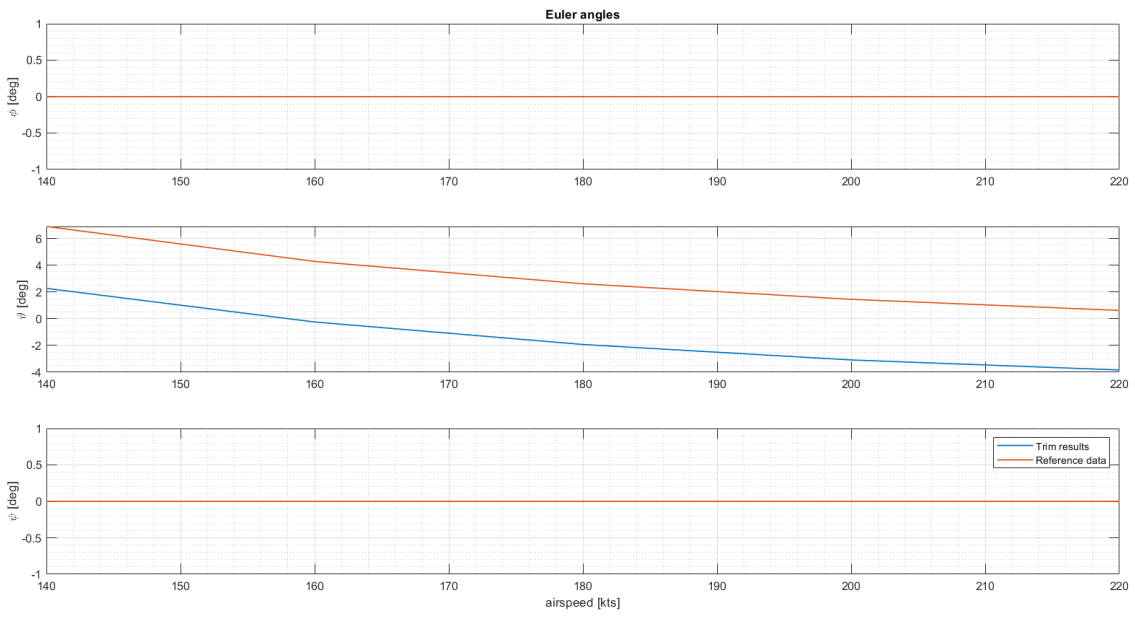
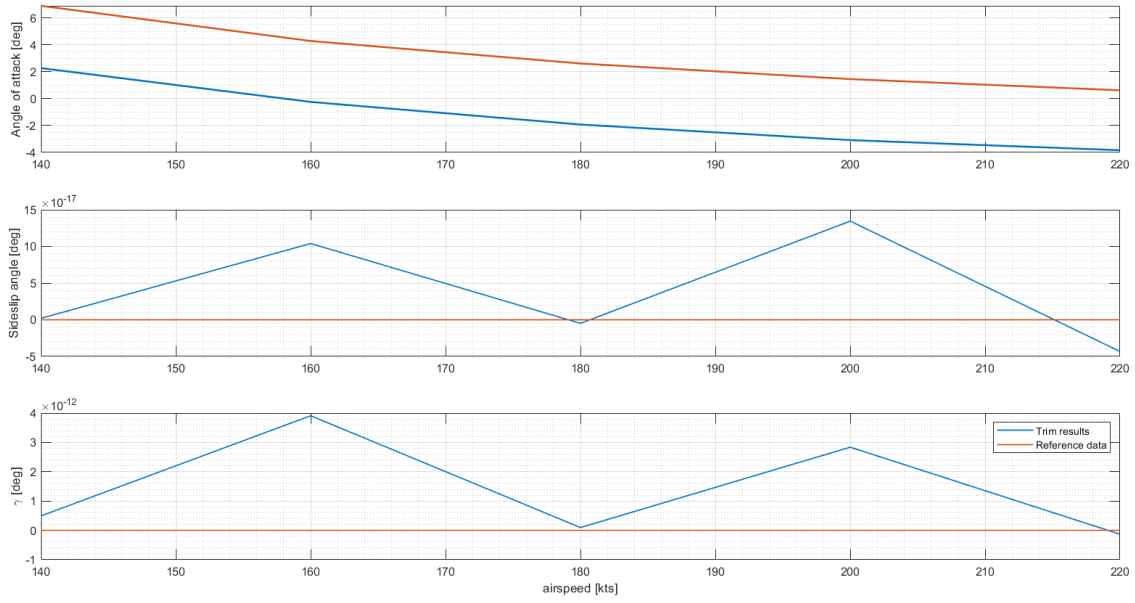


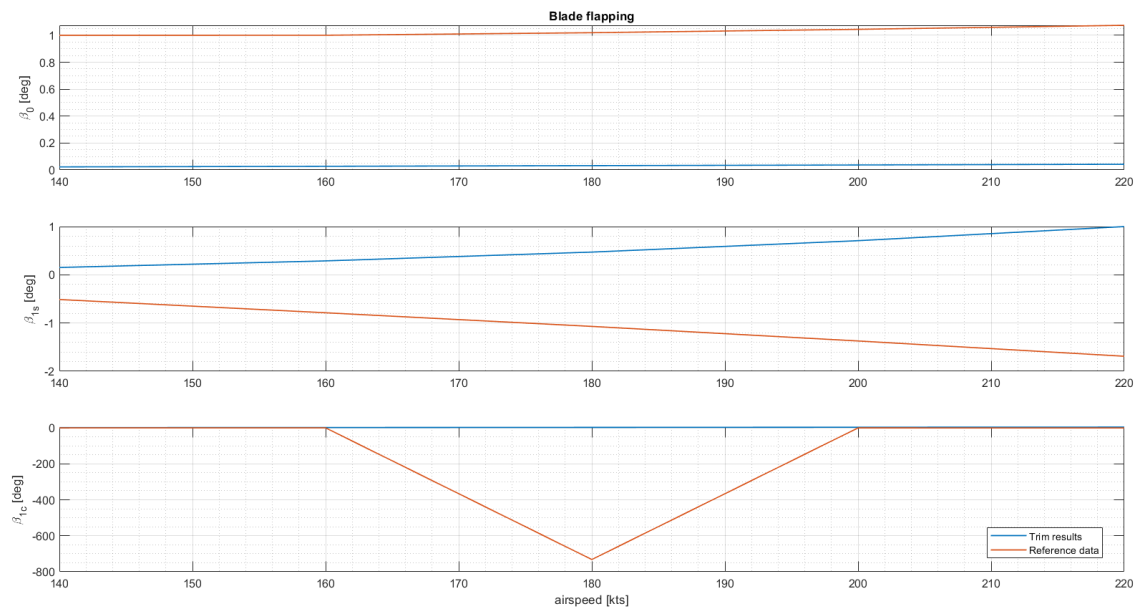
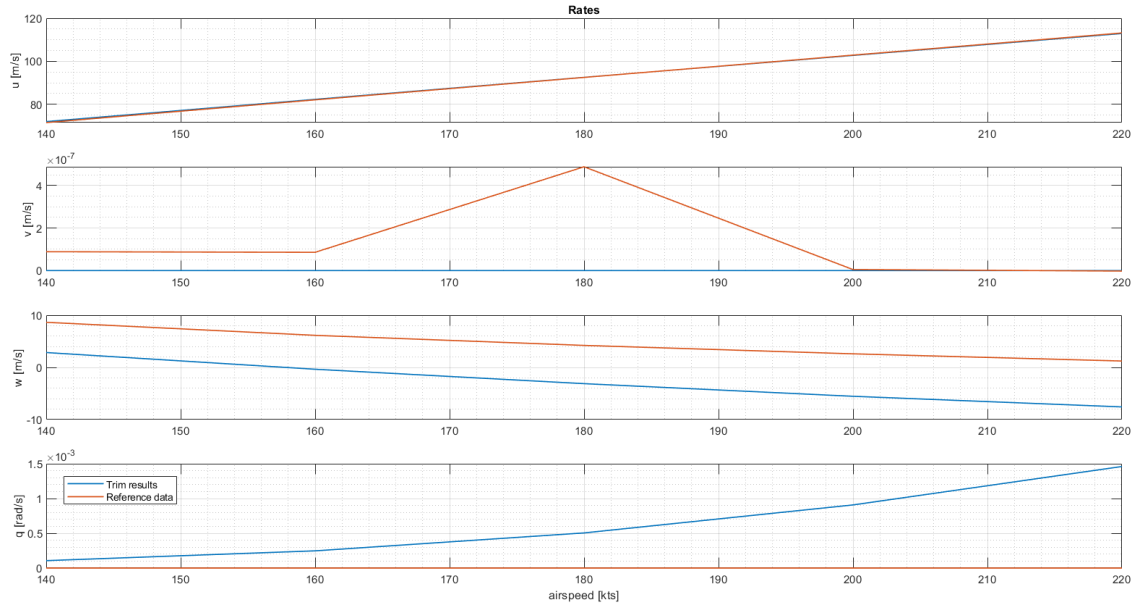


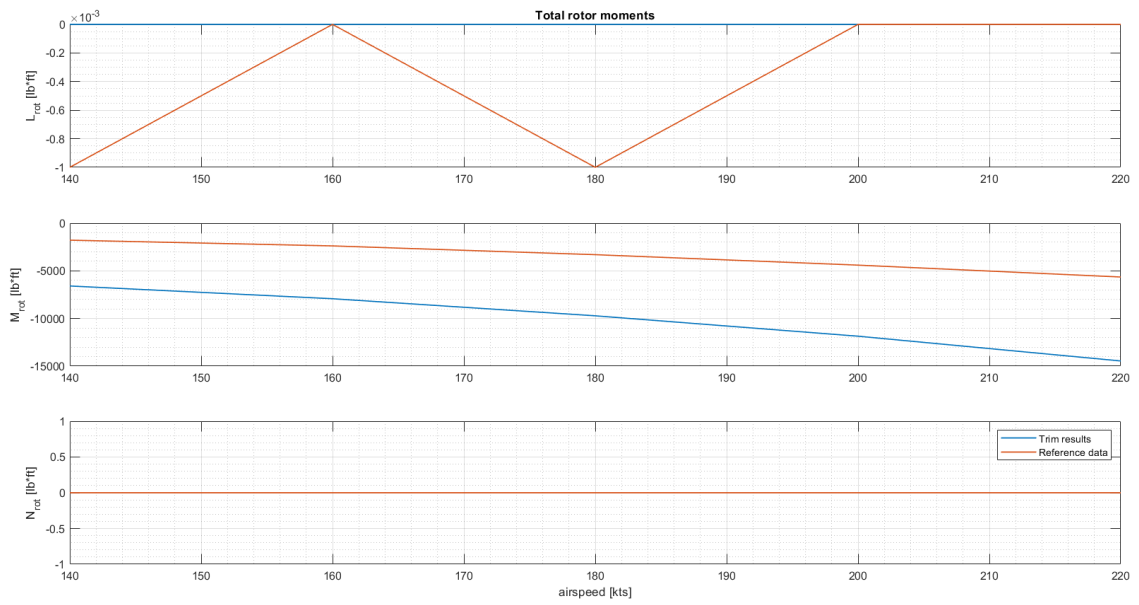
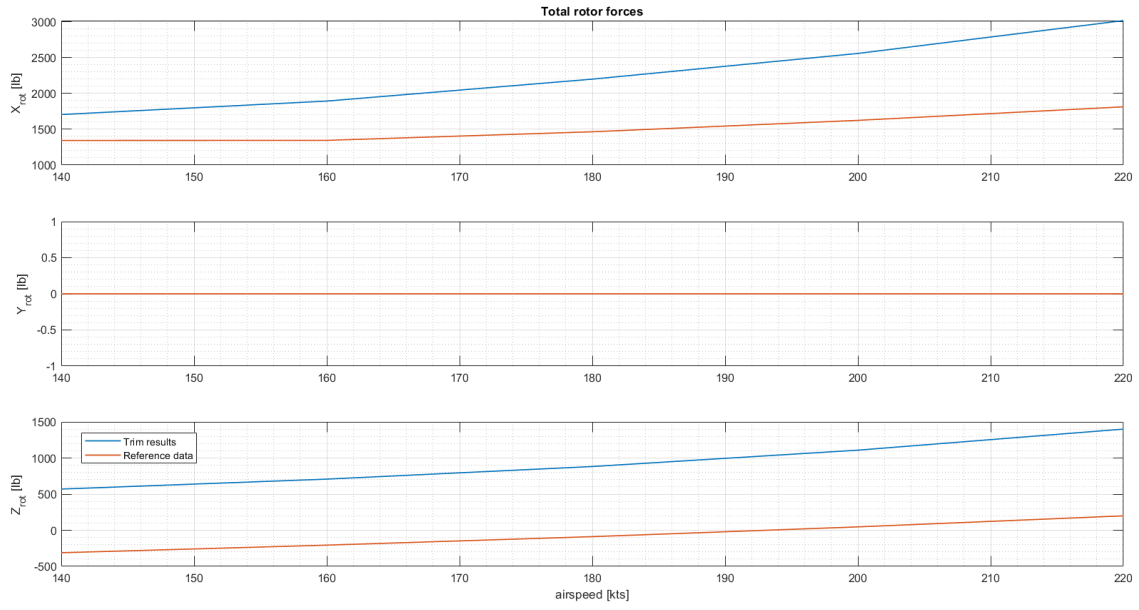
**Flight conditions**

- Nacelle incidence: 0 degrees
- Rotor speed: 589 rpm
- Flap/flaperon position: 0/0 degrees
- Altitude: Sea Level Standard
- Airspeed: 140, 160, 180, 200, 220 knots



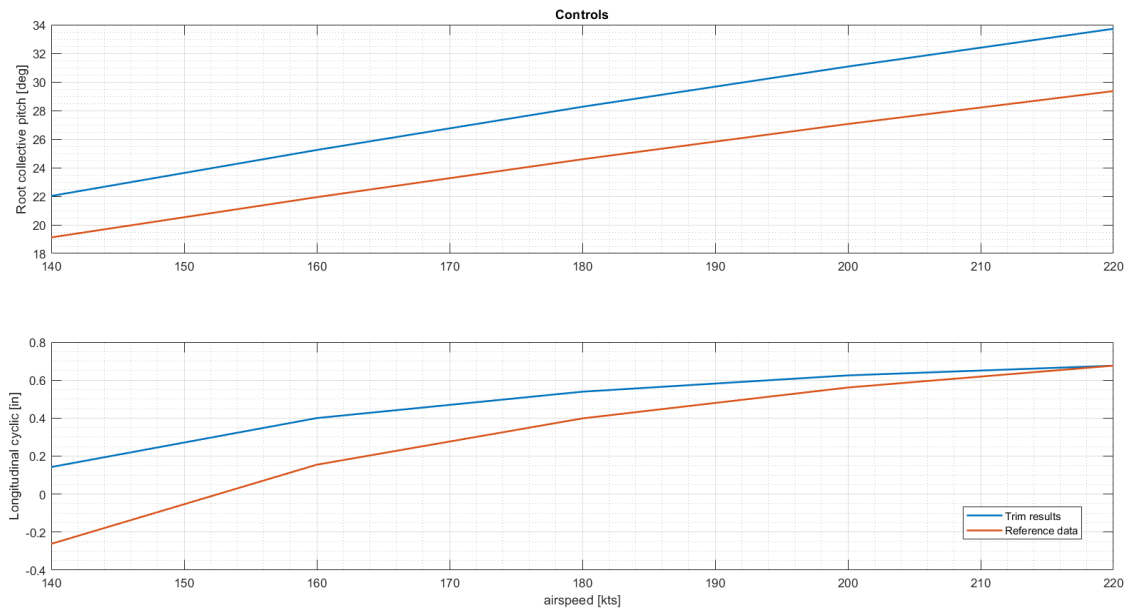


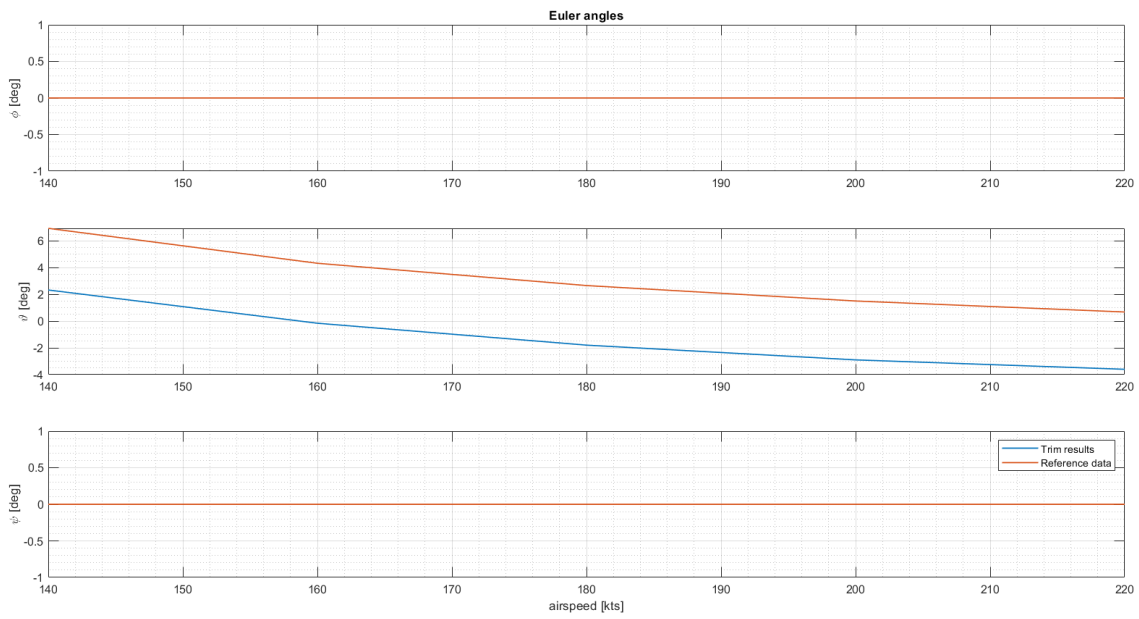
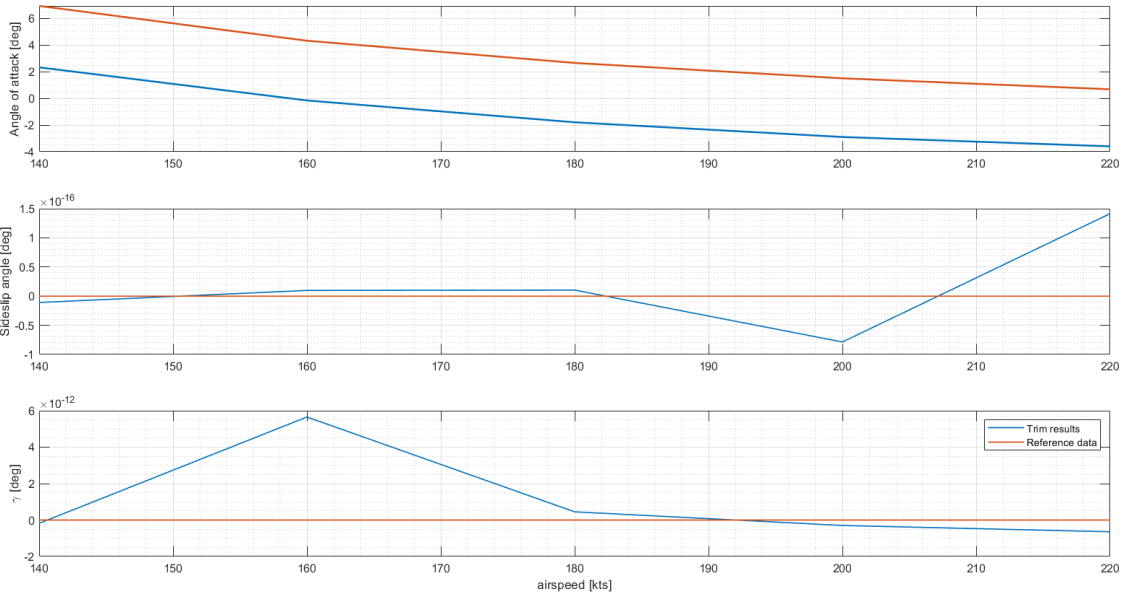


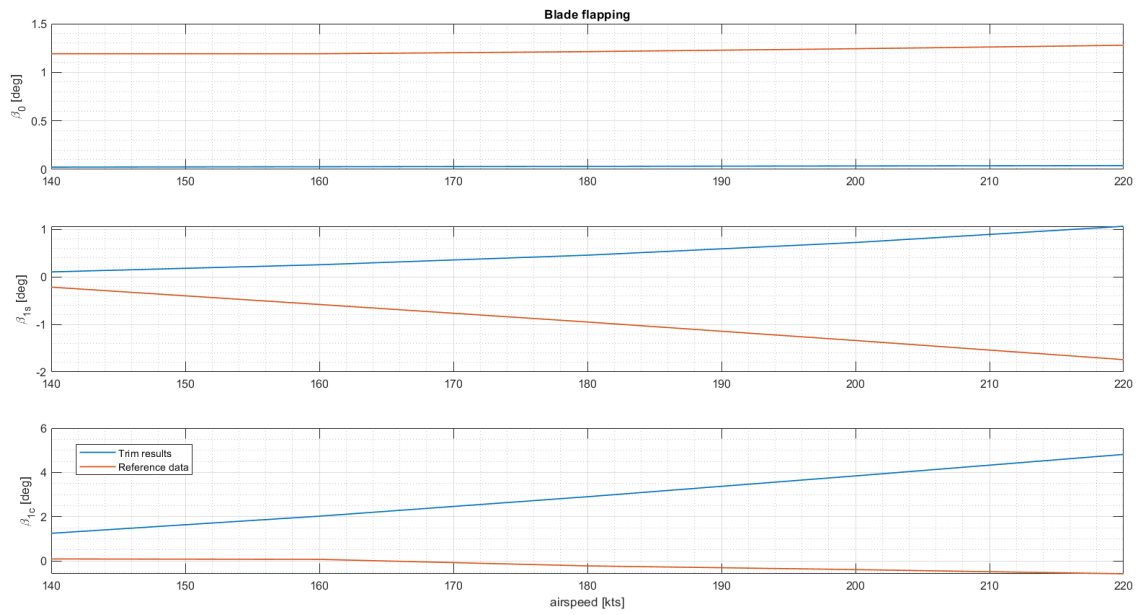
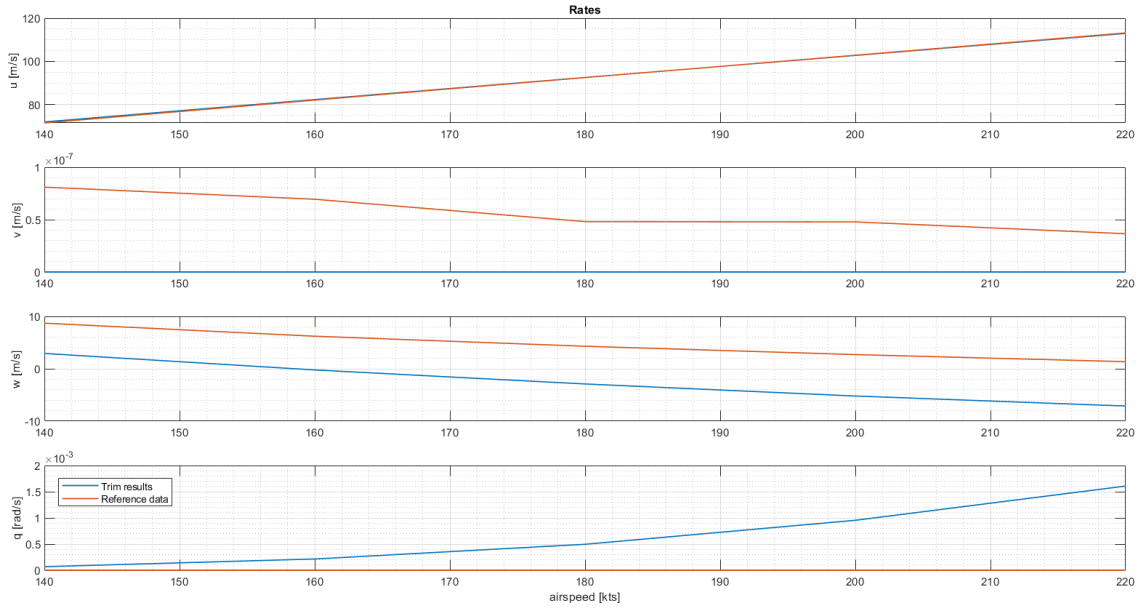


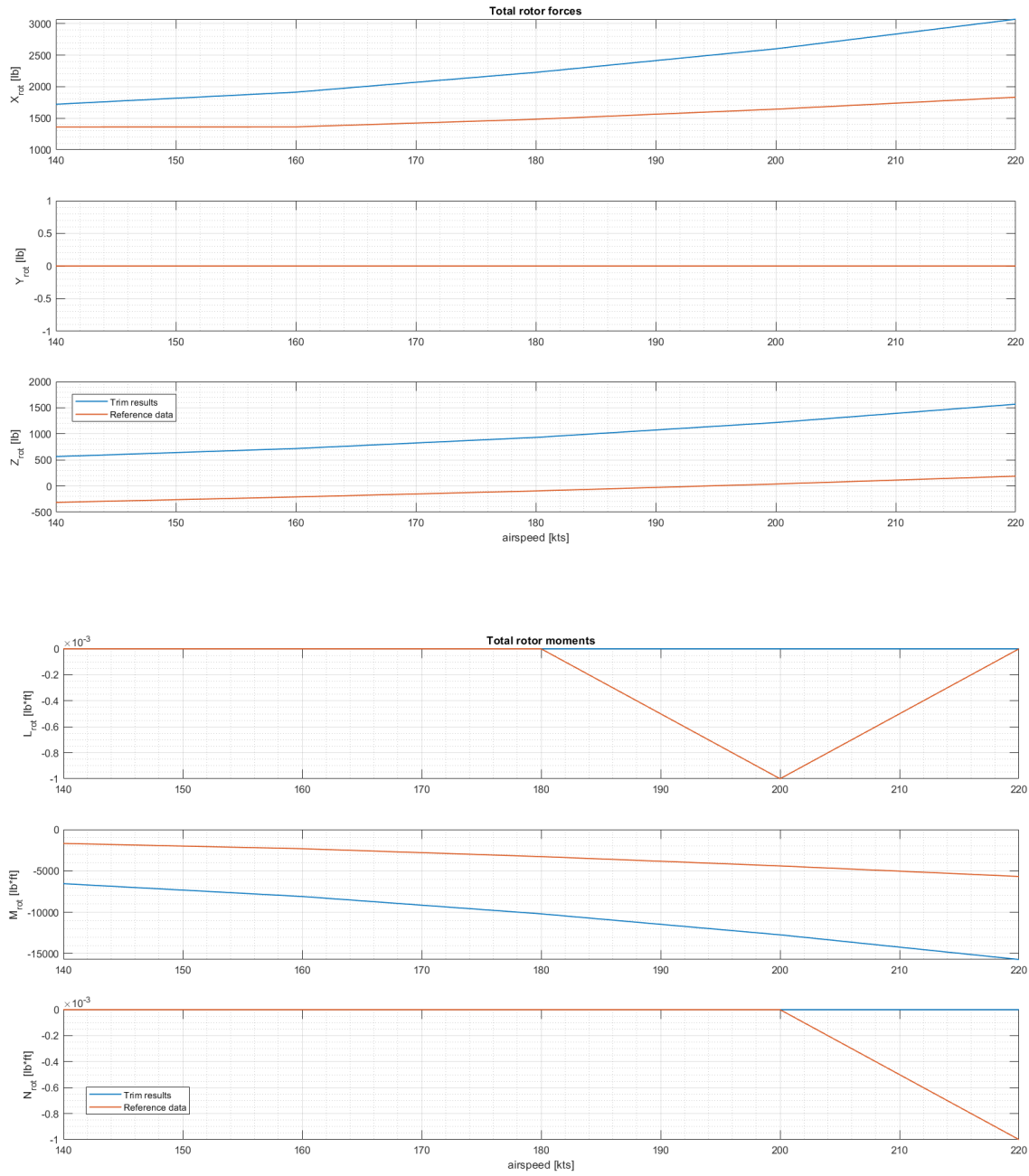
**Flight conditions**

- Nacelle incidence: 0 degrees
- Rotor speed: 517 rpm
- Flap/flaperon position: 0/0 degrees
- Altitude: Sea Level Standard
- Airspeed: 140, 160, 180, 200, 220 knots



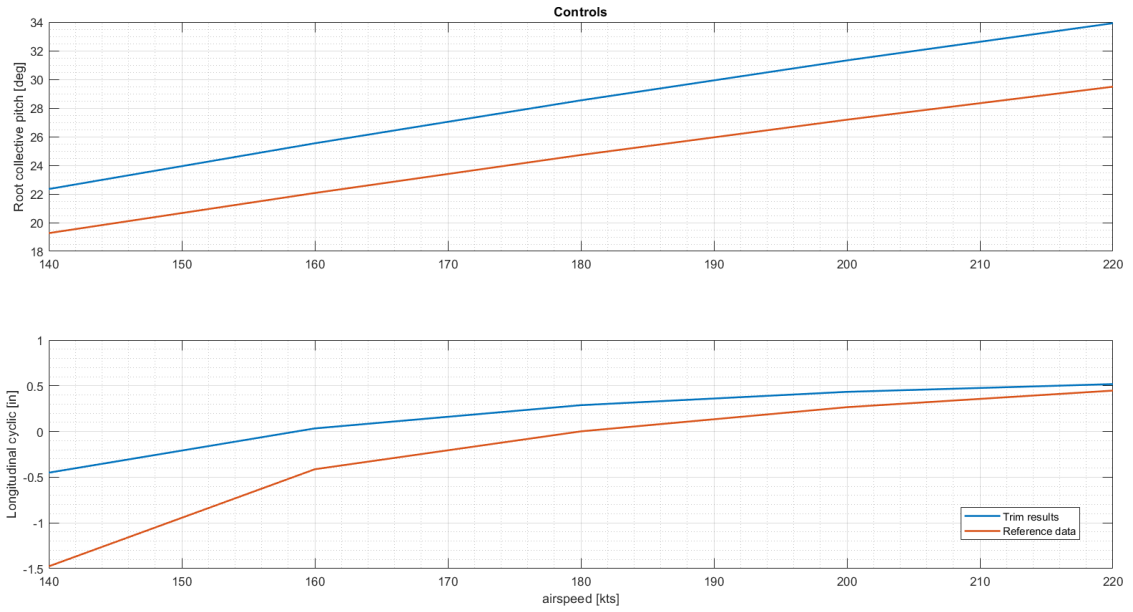


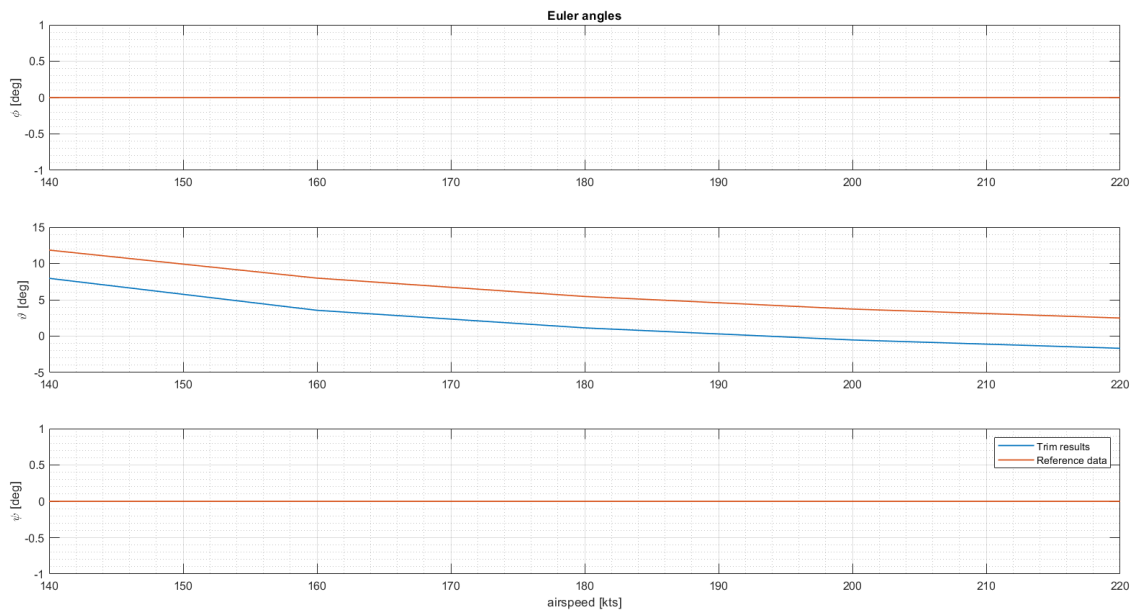
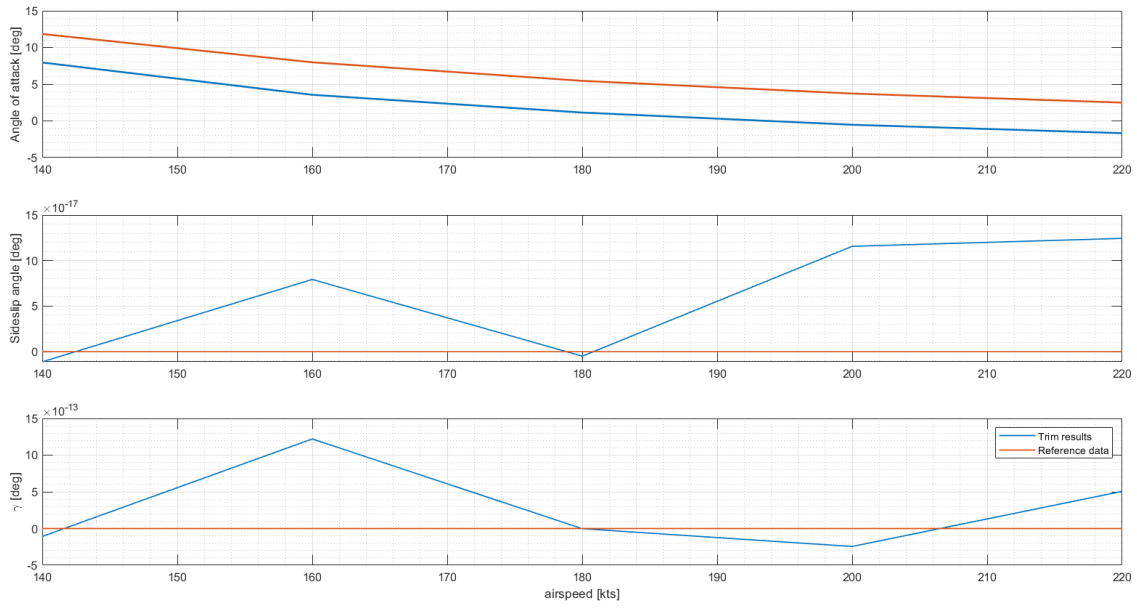


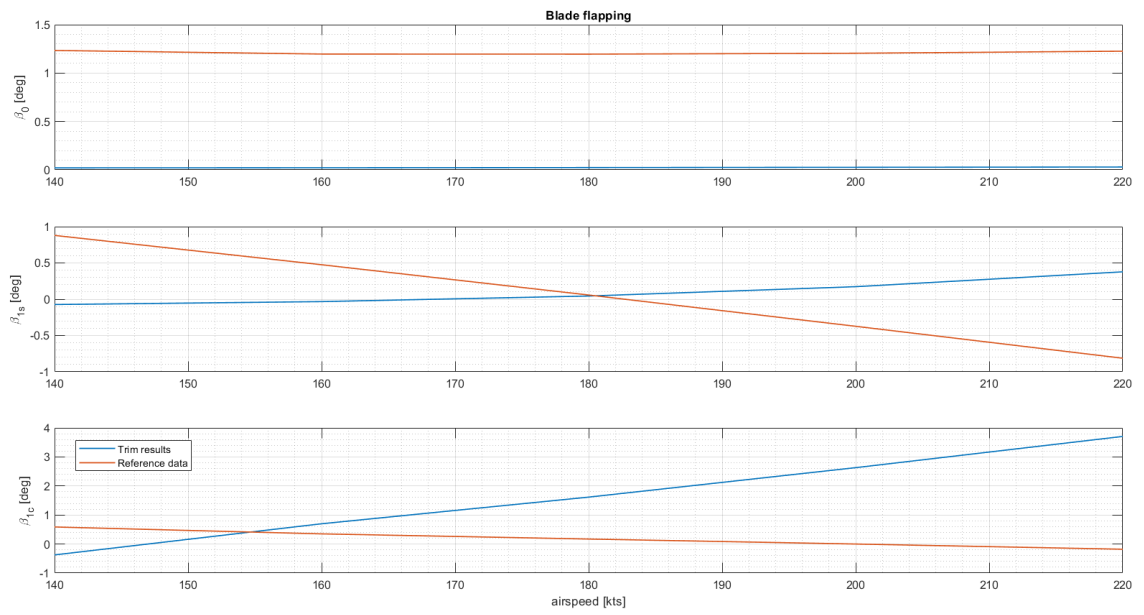
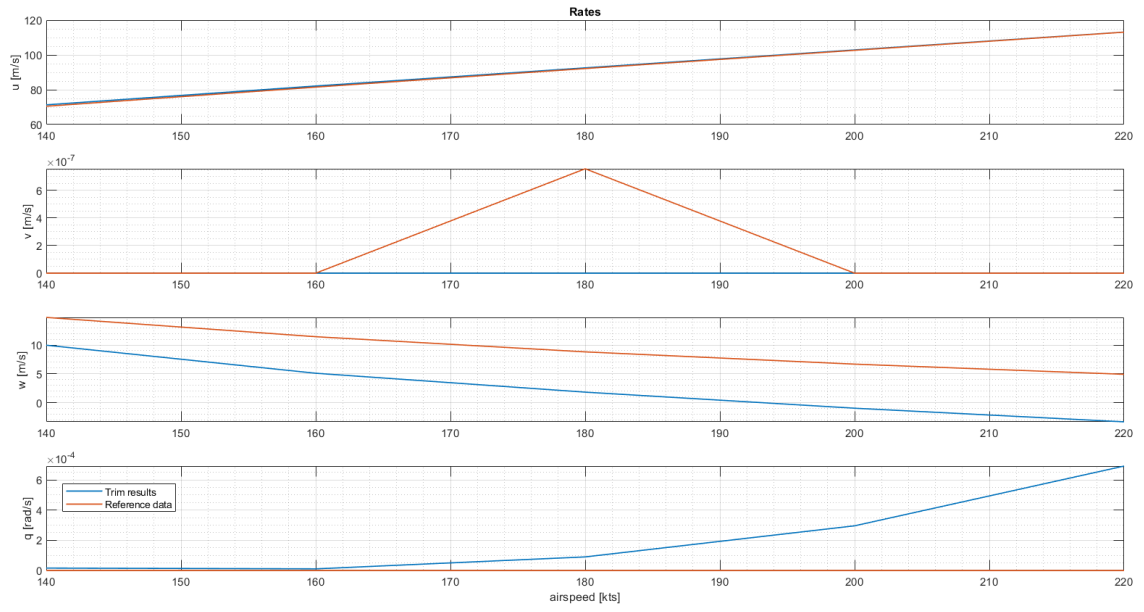


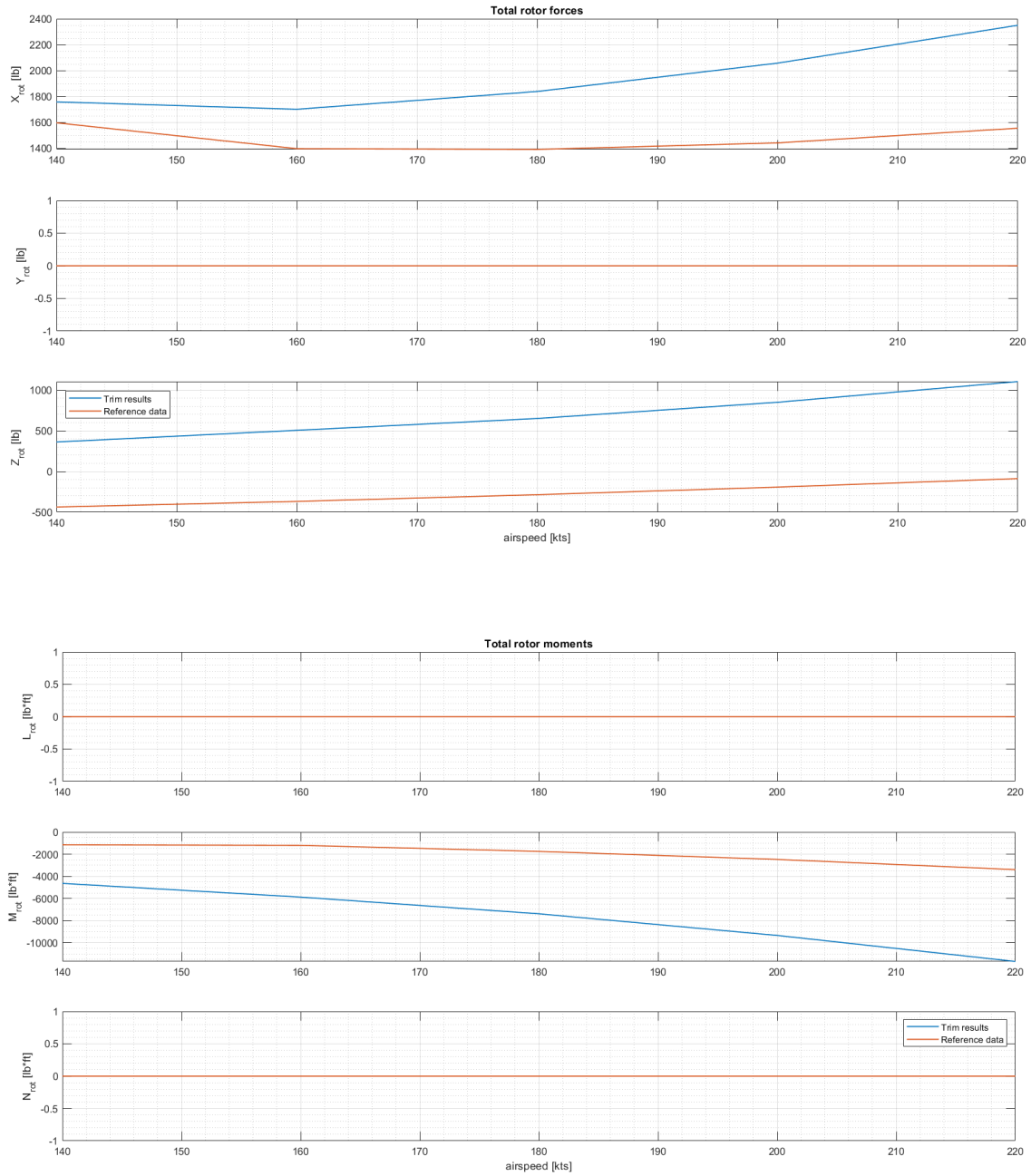
**Flight conditions**

- Nacelle incidence: 0 degrees
- Rotor speed: 517 rpm
- Flap/flaperon position: 0/0 degrees
- Altitude: 12000 ft Standard
- Airspeed: 140, 160, 180, 200, 220 knots









# Appendix C

## Examples of Flight Test Cards

### C.1 The Cooper-Harper Handling Qualities Rating Scale

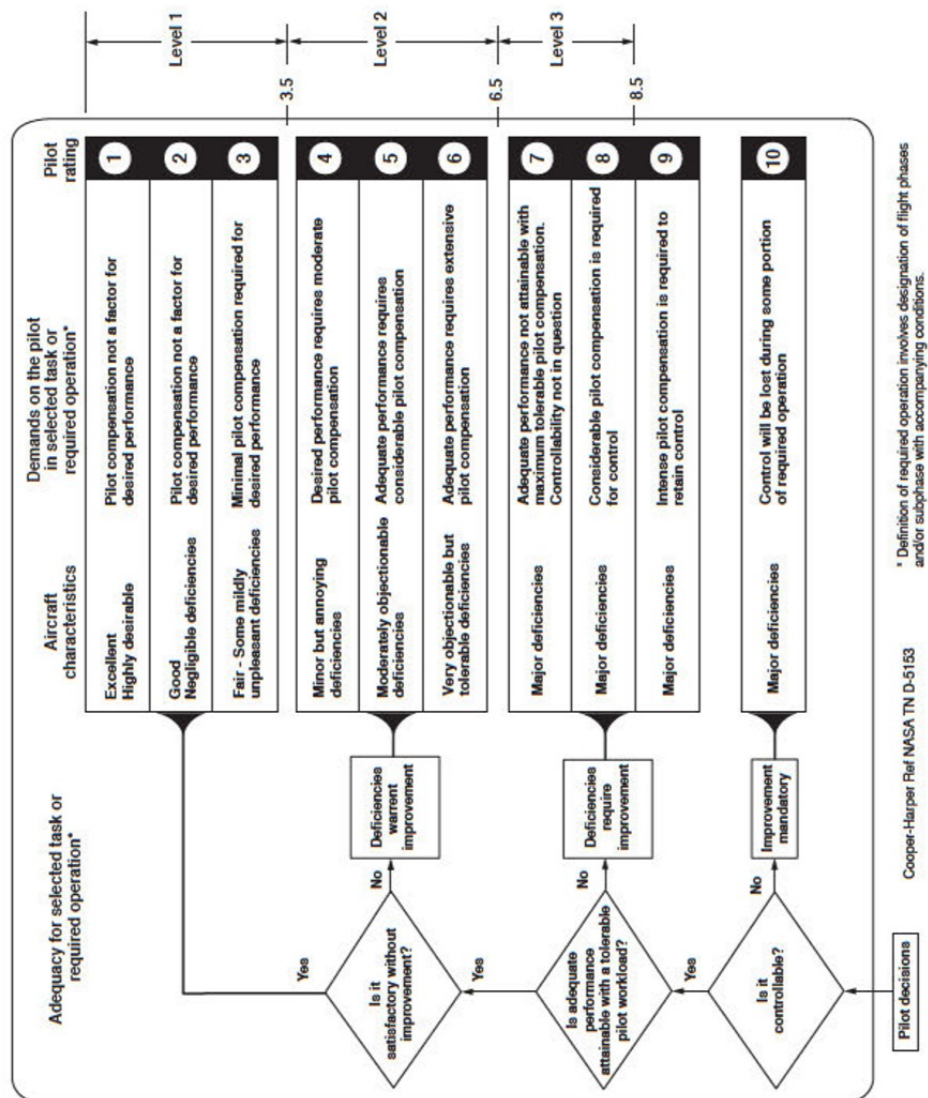


Figure C.1: The Cooper-Harper Handling Qualities Rating Scale (Reference [1])

## C.2 Helicopter mode

### C.2.1 Hover

Engineering Card	Project		Simulation number
	XV-15 Model Development		26.1
Prepared by	Test Pilot		Aircraft Model
Anna Abà	Raphael Monstein		XV-15
Headline	Date		In-flight Card Recording
	14-feb-20		Anna Abà
Aircraft Data			
Empty Weight	10083 lb	Flight Mode	Helicopter
Maximum take-off weight	13000 lb	Initial Condition	On ground
Take-off Weight	13000 lb	SCAS	On
Times			
Flight Duration	380 s	Task Duration	50 s
Mission task: Hover			
Performance achieved	Less than adequate	Cooper-Harper Rating	8
Notes			
Notes from the Pilot			
<ol style="list-style-type: none"> <li>1. Aircraft is still very lively, even with SCAS on: high impulse in any control results in very enhanced response (from which it is difficult to bring the machine back to stability).</li> <li>2. Even with very little speed (10 kts) airplane is very much more stable. When deceleration starts stability decreases.</li> <li>3. Deceleration in one smooth maneuver is very hard to obtain. Pilot suggested having a visual cue identifying the starting point for deceleration.</li> <li>4. Establishing a more or less stabilised hover takes a lot of time since start of deceleration.</li> <li>5. Altitude changes are very quick and hard to detect by only looking at the visual.</li> <li>6. Hovering for 30 seconds requires extensive pilot compensation, on all axes.</li> <li>7. Pilot noticed coupling between roll and yaw. Strong pedal input causes also roll response.</li> </ol>			
Additional notes			
<ol style="list-style-type: none"> <li>1. Once hover was reached, altitude and position variations satisfied acceptable performance standards.</li> </ol>			

<b>Engineering Card</b>	<b>Project</b>		<b>Simulation number</b>
	XV-15 Model Development		16.1
<b>Prepared by</b>	<b>Test Pilot</b>		<b>Aircraft Model</b>
Anna Abà	Davide Guscetti		XV-15
<b>Headline</b>	<b>Date</b>		<b>In-flight Card Recording</b>
	12-feb-20		Anna Abà
<b>Aircraft Data</b>			
Empty Weight	10083 lb	Flight Mode	Helicopter
Maximum take-off weight	13000 lb	Initial Condition	On ground
Take-off Weight	13000 lb	SCAS	Off
<b>Times</b>			
Flight Duration	399 s	Task Duration	36 s
<b>Mission task: Hover</b>			
Performance achieved	Less than adequate	Cooper-Harper Rating	9
<b>Notes</b>			
Notes from the Pilot			
<ol style="list-style-type: none"> <li>1. Visual cues on the right side cannot be seen; the ones at 45 degrees help holding position.</li> <li>2. Pitch oscillations are huge, so pilot concentrates in compensating them, which in turn leads oscillations on the other axes to grow.</li> <li>3. Low damping on roll is evident: unlike in other tasks, pilot has to be very delicate with his actions even on this axis.</li> <li>4. Yaw oscillations are also important; pilot has to compensate a lot with pedals (very high command amplitude is required).</li> <li>5. When pilot tries to correct more actively, oscillations start to grow and stability is lost.</li> <li>6. Pilot finds it difficult to estimate altitude based only on the visual.</li> </ol>			
Additional notes			
1. Task had to be aborted after 20 seconds, to avoid loss of control of the aircraft.			

## C.2.2 Pirouette

<b>Engineering Card</b>	<b>Project</b>		<b>Simulation number</b>
	XV-15 Model Development		1.3
<b>Prepared by</b>	<b>Test Pilot</b>		<b>Aircraft Model</b>
Anna Abà	Davide Guscetti		XV-15
<b>Headline</b>	<b>Date</b>		<b>In-flight Card Recording</b>
	10-feb-20		Anna Abà
<b>Aircraft Data</b>			
Empty Weight	10083 lb	Flight Mode	Helicopter
Maximum take-off weight	13000 lb	Initial Condition	On ground
Take-off Weight	13000 lb	SCAS	On
<b>Times</b>			
Flight Duration	901 s	Task Duration	44 s
<b>Mission task: Pirouette</b>			
Performance achieved	Adequate	Cooper-Harper Rating	5
<b>Notes</b>			
Notes from the Pilot			
<ol style="list-style-type: none"> <li>1. Once a certain lateral speed is achieved, the aircraft is more stable and the maneuver can be completed without excessive need for compensation.</li> <li>2. Yaw is not very stable; pilot needs to constantly compensate with the pedals.</li> <li>3. Detecting changes in pitch and altitude is difficult: simulator provides less ground reference and has no motion feedback. Image definition is also not very high.</li> <li>4. Altitude tends to increase when lateral speed increases. Pilot corrected a little too much with the collective, causing aircraft to lose altitude and gain speed, and resulting in higher trajectory radius towards the end of the maneuver.</li> </ol>			
Additional notes			
<ol style="list-style-type: none"> <li>1. Achieving a stabilised hover was not possible; therefore, the task has been performed without the initial and final 5-second hover.</li> <li>2. The SCAS currently implemented within the model has no damping around the yaw axis.</li> <li>3. Aircraft nose was not exactly pointed towards the reference point, as pilot had difficulties seeing the cones on his right. Next runs will be performed at lower altitude, to obtain better visibility.</li> <li>4. Cooper-Harper rating refers to the pirouette maneuver alone; hover is not considered.</li> </ol>			

<b>Engineering Card</b>	<b>Project</b>		<b>Simulation number</b>
	XV-15 Model Development		3.1
<b>Prepared by</b>	<b>Test Pilot</b>		<b>Aircraft Model</b>
Anna Abà	Davide Guscetti		XV-15
<b>Headline</b>	<b>Date</b>		<b>In-flight Card Recording</b>
	10-feb-20		Anna Abà
<b>Aircraft Data</b>			
Empty Weight	10083 lb	Flight Mode	Helicopter
Maximum take-off weight	13000 lb	Initial Condition	On ground
Take-off Weight	13000 lb	SCAS	Off
<b>Times</b>			
Flight Duration	224 s	Task Duration	42 s
<b>Mission task: Pirouette</b>			
Performance achieved	Adequate	Cooper-Harper Rating	6
<b>Notes</b>			
Notes from the Pilot			
<ol style="list-style-type: none"> <li>1. Pitch oscillations with SCAS off are very important and demand significant corrections from the pilot.</li> <li>2. Roll is not very different from the SCAS-On situation.</li> <li>3. Yaw oscillations are still present.</li> <li>4. Once sufficient lateral speed has been gained, no excessive compensation is required to complete the maneuver.</li> <li>5. Keeping a constant altitude is very difficult.</li> </ol>			
Additional notes			
<ol style="list-style-type: none"> <li>1. Achieving a stabilised hover was not possible; therefore, the task has been performed without the initial and final 5-second hover.</li> <li>2. Cooper-Harper rating refers to the pirouette maneuver alone; hover is not considered.</li> </ol>			

## C.2.3 Sidestep

<b>Engineering Card</b>	<b>Project</b>		<b>Simulation number</b>
	XV-15 Model Development		9.4
<b>Prepared by</b>	<b>Test Pilot</b>		<b>Aircraft Model</b>
Anna Abà	Davide Guscetti		XV-15
<b>Headline</b>	<b>Date</b>		<b>In-flight Card Recording</b>
	11-feb-20		Anna Abà
<b>Aircraft Data</b>			
Empty Weight	10083 lb	Flight Mode	Helicopter
Maximum take-off weight	13000 lb	Initial Condition	On ground
Take-off Weight	13000 lb	SCAS	On
<b>Times</b>			
Flight Duration	545 s	Task Duration	49 s
<b>Mission task: Sidestep</b>			
Performance achieved	Less than adequate	Cooper-Harper Rating	7
<b>Notes</b>			
Notes from the Pilot			
<ol style="list-style-type: none"> <li>1. Pilot has no visibility 90 degrees to his side. To better see the reference line, pilot has performed the maneuver keeping aircraft nose slightly tilted in the direction of motion; as a result, additional longitudinal compensation was needed.</li> <li>2. Aircraft tends to move forward after lateral acceleration (in both directions) is initiated.</li> <li>3. When pilot reduces speed to achieve hover, aircraft becomes less stable and it is easy to lose position.</li> <li>4. Instability arises also when pilot initiates acceleration from hover to go back to the starting point.</li> <li>5. Evaluating altitude and attitude changes from the visual is very hard.</li> </ol>			
Additional notes			
<ol style="list-style-type: none"> <li>1. Altitude and longitudinal position variations satisfy acceptable performance standards.</li> <li>2. Maneuver is not aggressive enough to meet lateral speed and bank angle requirements.</li> </ol>			

<b>Engineering Card</b>	<b>Project</b>		<b>Simulation number</b>
	XV-15 Model Development		23.2
<b>Prepared by</b>	<b>Test Pilot</b>		<b>Aircraft Model</b>
Anna Abà	Raphael Monstein		XV-15
<b>Headline</b>	<b>Date</b>		<b>In-flight Card Recording</b>
	13-feb-20		Anna Abà
<b>Aircraft Data</b>			
Empty Weight	10083 lb	Flight Mode	Helicopter
Maximum take-off weight	13000 lb	Initial Condition	On ground
Take-off Weight	13000 lb	SCAS	On
<b>Times</b>			
Flight Duration	228 s	Task Duration	44 s
<b>Mission task: Sidestep</b>			
Performance achieved	Less than adequate	Cooper-Harper Rating	7
<b>Notes</b>			
Notes from the Pilot			
<ol style="list-style-type: none"> <li>1. Simulator provides very limited lateral visibility. Pilot performed the task keeping the aircraft a few metres behind the reference line.</li> <li>2. Visual cues are not seen as they were meant to, so it is harder to keep the trajectory straight.</li> <li>3. When pilot initiates the lateral acceleration, altitude increases and the aircraft drifts forward.</li> <li>4. Establishing a more or less stable hover is difficult and takes a lot of time, as aircraft stability degrades at</li> <li>5. Visual system is not smooth and does not help to hold altitude constant.</li> </ol>			
Additional notes			
<ol style="list-style-type: none"> <li>1. Maneuver has been performed aggressively, as required by ADS-33. Acceptable values of bank angle and lateral speed have been attained.</li> <li>2. Trajectory does not meet requirements for an acceptable performance.</li> </ol>			

### C.3 Airplane mode

<b>Engineering Card</b>	<b>Project</b>		<b>Simulation number</b>
	XV-15 Model Development		18.4
<b>Prepared by</b>	<b>Test Pilot</b>		<b>Aircraft Model</b>
Anna Abà	Davide Guscetti		XV-15
<b>Headline</b>	<b>Date</b>		<b>In-flight Card Recording</b>
	12-feb-20		Anna Abà
<b>Aircraft Data</b>			
Empty Weight	10083 lb	Flight Mode	Airplane
Maximum take-off weight	13000 lb	Initial Condition	550 m, 120 kts
Take-off Weight	13000 lb	SCAS	Off
<b>Times</b>			
Flight Duration	399 s	Task Duration	36 s
<b>Mission task: Rudder kicks + free practice</b>			
Performance achieved	--	Cooper-Harper Rating	--
<b>Notes</b>			
Notes from the Pilot			
<ol style="list-style-type: none"> <li>1. Aircraft is in general very responsive: a minimum input from the pilot generates immediately evident effects.</li> <li>2. Following the doublet pedal input, oscillations are damped in very short time.</li> <li>3. An attempt at performing a turn at constant bank angle highlighted high-amplitude, low-damped roll oscillations, requiring significant pilot compensation.</li> <li>4. A problem with the visual occurred, due to which the aircraft appeared to be drifting to the left (although neither the cockpit instruments nor simulation data displayed any sideslip).</li> </ol>			
Additional notes			
<ol style="list-style-type: none"> <li>1. Power control is obtained using the collective lever.</li> <li>2. Aircraft is definitely overpowered, as the engine model has not been implemented yet.</li> </ol>			

# Bibliography

- [1] ADS-33E-PRF. *Performance Specification – Handling Qualities Requirements for Military Rotorcraft*. 2000.
- [2] Federico Barra. “Development of a tilt-rotor model for real-time flight simulation”. Politecnico di Torino, 2018.
- [3] Richard L. Bielawa. *Rotary Wing Structural Dynamics and Aeroelasticity*. 2nd ed. AIAA American Institute of Aeronautics and Astronautics, 2006.
- [4] A. R. S. Bramwell, David Balmford, and George Done. *Bramwell’s Helicopter Dynamics*. Butterworth-Heinemann, 2001.
- [5] Pierluigi Capone. “Trim Algorithm”. 2017.
- [6] R. T. N. Chen. *Effects of Primary Rotor Parameters on Flapping Dynamics*. TP-1431. 1980.
- [7] Samuel W. Ferguson. *A Mathematical Model for Real Time Flight Simulation of a Generic Tilt-Rotor Aircraft*. CR-166536. Ames Research Center, Moffet Field, California, 1983.
- [8] Samuel W. Ferguson. *Development and Validation of a Simulation for a Generic Tilt-Rotor aircraft*. CR-166537. Ames Research Center, Moffet Field, California, 1988.
- [9] Simone Godio. “Multi-purpose rotor model for a real-time flight simulator”. Politecnico di Torino, 2019.
- [10] Giorgio Guglieri, Andrea Quinci, and Massimiliano Porta. *Meccanica del volo dell’elicottero*. Esculapio Editore, 2018.
- [11] Franklin D. Harris. *Hover Performance of Isolated Proprotors and Propellers — Experimental Data*. CR-219486. 1988.
- [12] Franklin D. Harris. *Introduction to Autogyros, Helicopters, and Other V/STOL Aircraft*. SP-2015-215959. Ames Research Center, Moffet Field, California, 2015.
- [13] S. F. Hoerner. *Fluid Dynamic Lift*. S. F. Editions, 1975.
- [14] Wayne Johnson. *Helicopter Theory*. Dover Publications, Inc., 1980.
- [15] Martin D. Maisel, Demo J. Giulianetti, and Daniel D. Dugan. *The History of the XV-15 Tilt Rotor Research Aircraft*. SP-200-5417. Washington, D. C., 2000.
- [16] Gareth D. Padfield. *Helicopter Flight Dynamics*. 3rd ed. Wiley & Sons, 2018.
- [17] David A. Peters and Dinesh Barwey. *A General Theory of Rotorcraft Trim*. St. Louis, MO, 1996.
- [18] Dale M. Pitt and David A. Peters. “Theoretical prediction of dynamic-inflow derivatives”. In: *Sixth European rotorcraft and powered lift aircraft forum* (1980).
- [19] M. D. Takahashi. *A Flight-Dynamic Helicopter Mathematical Model with a Single Flap-Lag-Torsion Main Rotor*. TM-102267. 1990.

- [20] AA. VV. *Civil Tiltrotor Missions and Applications: A Research Study*. CR-177452. 1987.